学位論文

S-wave velocity structure of the lithosphere beneath

Mt. Fuji, Japan, by inversion of receiver functions

（ レシーバ関数のインバージョン解析による

富士山下のＳ波速度構造の研究 　）

東京大学大学院理学系研究科

地球惑星科学専攻

木下(宮林) 佐和子

Abstract

Mt. Fuji, the largest stratovolcano in central Japan, has ejected a huge amount of basaltic products during the last 100,000 years. Although the reason for this high eruptive rate has not been well understood yet, a complicated tectonic setting is likely to be responsible for this uniqueness. Because the Izu-Bonin-Mariana arc with a thickened crust is colliding and subducting below the Eurasian and Okhotsk plates around Mt. Fuji, a generic magma plumbing model for arc volcanoes is not readily applicable.

The purpose of this study is to understand the magma plumbing system of Mt. Fuji that ejects basaltic magma with a high long-term eruption rate. To address this, we conduct a receiver function (RF) analysis to investigate the seismic structure including the distributions of the subducting arc and the magma chamber around Mt. Fuji.

Cross sections of radial RF amplitudes reveal distinct positive velocity boundaries at depths of 40–60 km and 20–30 km around Mt. Fuji. We interpret the velocity boundary at 40–60 km depth as the lower boundary of the crust of subducting arc and that at 20–30 km depth as the lower boundary of the magma chamber of Mt. Fuji. Also, the velocity boundary representing the lower boundary of the arc crust does not continue immediately below Mt. Fuji at a depth of about 50 km, representing a locally weakened velocity contrast.

Next, we conducted an inversion analysis of receiver functions to investigate absolute S-wave velocities around Mt. Fuji, because the thick volcanic sediment layer and low velocity layers below Mt. Fuji change the amplitude of radial RFs. In RF inversions, there is a trade-off between the depth of the velocity boundary and the average velocity over the boundary, so we constrained results of the inversion by inverting receiver functions and dispersion curves of surface waves together.

Our results are characterized by the following three features: 1) The north-south cross section of absolute velocities reveals that the width of the Izu-Bonin-Mariana arc crust is developed down to a depth about 40 km. 2) Subducting oceanic crust, about 30–100 km to the southwest and 60–100 km to the northeast of Mt. Fuji, is represented by a low velocity body. 3) A distinct low velocity region exists below Mt. Fuji with a width of 40 km in horizontal direction and 20 km width in vertical direction, representing a crustal magma chamber of Mt. Fuji.

Our findings suggest that 1) Mt. Fuji has ejected mostly basaltic rocks because the crustal magma chamber is deep, and 2) an anomalously high eruption rate of Mt Fuji is because it hosts a large crustal magma chamber.

Abstract

富士山は、日本の代表的な活火山であり、2つの大きな特徴をもっている。まず、マグマの噴出量が1000年で約5立方キロメートルで、日本の他の火山と比較すると数倍から数十倍大きくなっている。さらに、最近10万年間は主に玄武岩質のマグマを噴出しつづけており、主に安山岩質のマグマを噴出する一般的な島弧火山とは異なる。富士山がこのような性質を持つ理由はわかっていないが、富士山が位置する場所が非常に複雑であることが起因している可能性がある。富士山の下には、南からフィリピン海プレートが沈み込み、その下約100kmの深さでは、東から太平洋プレートが沈み込んでいる。そして、富士山下で沈み込んでいるフィリピン海プレートは、それ自体が太平洋プレートの沈み込みによってできた伊豆-ボニン-マリアナ島弧 (IBM) で、地殻が発達している。富士山のマグマは太平洋プレートが沈み込むことで生成されて上昇し、その途中でIBM島弧を通り抜けており、マグマ供給系が他の火山と異なる可能性がある。本研究は、富士山のマグマ供給系を解明するために、レシーバ関数解析によって富士山下に沈み込むIBM島弧やマグマ溜まりの構造を含めた地下構造を明らかにすることを目標にした。

　レシーバ関数のラディアル成分の振幅を富士山を通る断面に投影すると、富士山下約40-60kmの深さに南北に沈み込む強い正の速度境界面があり、富士山直下でその境界面は不連続になっていることがわかった。また、富士山下で低周波地震が発生する領域の下、およそ25kmの深さに顕著な正の速度境界面があることもわかった。富士山周辺では、表層に地震波速度が遅い火山噴出物が堆積しており、さらに深さ20km付近には顕著な地震波速度低速度領域があると考えられるため、レシーバ関数の振幅断面からのみ、速度構造を議論することは難しい。そこで、インバージョン解析によって、地下のS波速度の絶対値を求めた。レシーバ関数の振幅は地下の速度コントラストに依存するため、先行研究による表面波分散曲線を一緒にインバージョンすることで、解を安定させた。インバージョンの結果、以下に挙げる3つの結果が得られた。

1) 先行研究による沈み込む前の IBM 島弧の速度構造と比較すると、伊豆半島では、IBM 弧の地殻の厚さは約 40km の厚さまで成長している。2) 通常の海洋プレートが沈み込む場所では、先行研究のトモグラフィの結果と整合的な場所に S 波低速度領域があり、これは沈み込む海洋性地殻を表している。3) 富士山の下には横方向に約 40km 深さ方向に約 20km の大きさの S 波低速度領域が存在する。

レシーバ関数のインバージョン解析によって、先行研究の地震波トモグラフィよりも解像度良く、富士山下の低速度領域の場所がわかった、と考えられる。本研究の結果より、富士山のマグマ噴出率が高いのは、地下のマグマ溜まりが大きいからであり、また、富士山のマグマが玄武岩質なのは、マグマ溜まりの場所が深いからである、と解釈することができる。

Contents

List of Figures

List of Tables

1 Introduction

Mt. Fuji, the largest volcano in Japan with its volume of about 400 km^3 (*Tsukui et al.*, 1986) lies in the center of Honshu Islands, and is composed of four volcanic bodies (Figure 1.1 and Figure 1.2): Shin-Fuji, Ko-Fuji, Komitake, and Pre-Komitake (*Yoshimoto et al.*, 2010). The oldest body, Pre-Komitake, started eruption at about 0.27 Ma (*Yoshimoto et al.*, 2010). Historically, Mt. Fuji has erupted repeatedly every decade or hundreds of years. Currently Mt. Fuji has not erupted since the last one, the Hoei eruption, in 1707 for more than 300 years. Mt. Fuji has ejected mostly the basaltic lava flow with some exceptions like the Hoei eruption in 1707 that was a very explosive eruption with both andesitic and basaltic products (e.g., *Fujii*, 2007; *Kaneko et al.*, 2010). In spite of its dormancy, Mt. Fuji hosts low frequency earthquakes (LFEs) related to the magmatic activity a few times a month at depths between 10 and 15 km, a few kilometers to the northeast from the summit of Mt. Fuji. Number of LFEs increased just after a dike intrusion between the Miyake-jima and Kozu-shima area, 140 km to the southeast from Mt. Fuji (Figure 1.1), in 2000 and 2001 (*Ukawa*, 2005). A large tectonic earthquake with Mw 5.9 (East-Shizuoka earthquake) occurred 6.5 km to the southwest of Mt. Fuji (Figure 1.3) on 15 March 2011, 4 days after the 2011 Tohoku-oki earthquake. This earthquake generated numerous aftershocks around the hypocenter of the main shock (e.g., *Fujita et al.*, 2013).

Fujita et al. (2013) estimated that the Tohoku-oki earthquake and the East-Shizuoka earthquake pressurized the magma chamber of Mt. Fuji, which is assumed to exist on the LFE's area at a depth of 15 km with a radius of 3 km, by 0.001–0.01 MPa and 0.1–1.0 MPa, respectively. Despite the pressure changes at the magma reservoir (*Fujita et al.*, 2013), no signs of volcanic unrest, changes in seismic anisotropy, and an increase in LFEs have been observed right after these earthquakes (*Araragi et al.*, 2015). The magma plumbing system, especially of the size and location of the deep magma chamber below Mt. Fuji, is not well understood so far. This poor understanding prevents us from evaluating the effect of large earthquakes, such as the East-Shizuoka earthquake, on the

volcanic activity of Mt. Fuji.

1.1   Unique characteristics of Mt. Fuji

Mt. Fuji possesses two anomalous features for an arc volcano in that 1) the long-term eruption rate is much larger than other surrounding arc volcanoes in Japan (*Tsukui et al.*, 1986), and 2) basaltic rocks dominates while arc volcanoes are generally more silicic (*Fujii*, 2007). *Tsukui et al.* (1986) estimated long-term eruption rates on many volcanoes in Japan by dividing the volume of discharged material by the corresponding period of time. They estimated the volume of Mt. Fuji to be about 400 km^3 mostly built in the last 80 Ka. This leads them to estimate the long-term eruption rate of Mt. Fuji to be about 5 km^3/Ka, much larger than other arc volcanoes in Japan, about 0.01-0.1 km^3/Ka (*Tsukui et al.*, 1986; *Yoshimoto et al.*, 2010). Also, most of the erupted products of Mt. Fuji are basaltic with small variety in silica content, while volcanic rocks in Izu-Bonin-Mariana arc (IBM, Figure 1.1) have large variety in silica content.

A complicated tectonic background possibly causes these two characteristics of Mt. Fuji, where the Philippine Sea (PHS) plate subducts beneath the Eurasian and the Okhotsk plate to northwest and northeast along the Suruga and Sagami trough, respectively (Figure 1.1 and 1.3). Also, the Pacific (PAC) plate subducting beneath the PHS plate forms the Izu-Bonin-Mariana arc (IBM) with a length of 2800 km. IBM collides with Honshu Island at the Izu collision zone to the southeast of Mt. Fuji and subducts beneath the Eurasian and the Okhotsk plate in north direction. Primary magma of Mt. Fuji is made above subducting PAC slab at depths about 100–150 km. The magma then goes through such a complex region during upwelling. Considering tectonic setting around Mt. Fuji, the magma plumbing system of Mt. Fuji cannot be explained only by a generic model for arc volcanoes as with those in northern part of Japan.

1.2   Geological and Geochemical background of Mt. Fuji

As described above, the magma composition of Mt. Fuji is quite different from that of other volcanoes in IBM. *Fujii* (2007) compiled the previous petrological studies on Mt. Fuji to summarize that the basaltic magma of Mt. Fuji has three characteristics as described next.

First, the amount of silica in the magma is low while the amount of incompatible elements has large variety. Second, the ratio of minor element, Zr/Y, increases from Ko-Fuji to Shin-Fuji, and remain high in newer volcanoes. Third, the FeO*/MgO ratio of the magma ejected from Mt. Fuji is higher that 1.6, representing the highly differentiation of magma (*Fujii*, 2007). He concluded that the pyroxene makes a larger contribution to the fractional crystallization in the magma of Mt. Fuji than other volcanoes in IBM to propose that the magma chamber of Mt. Fuji is located at around 20 km, deeper than that of other volcanoes in IBM.

Kaneko et al. (2010) proposed a magma plumbing system of Mt. Fuji to explain the large variety of both FeO*/MgO and the content of incompatible elements and the small variety of SiO_2 content in basaltic magma of Mt. Fuji from chemical analyses on the whole rocks, phenocryst, and melt inclusion in air-fall scoria on eastern slope of Mt. Fuji. They found that the SiO_2 content in olivine melt-inclusions is largely variable, while those of whole rock are not variable, and proposed that Mt. Fuji ' s magmatic plumbing system consists of at least two magma chambers, a deep basaltic one at 20 km and a shallow one with more SiO_2-rich end members resulting from a differentiation of old magma at 10 km.

Nakamura et al. (2008) obtained the amount and origin of slab fluids in 28 Quaternary volcanoes in central Japan by examining trace elements. They showed that the amount of slab fluids in Mt. Fuji's volcanic rocks is much smaller than other volcanoes. They also showed that the slab fluid in Mt. Fuji's rock is originated predominantly from the PAC slab, rather than the PHS slab. This result implies that the PHS plate overriding the PAC plate does not contaminate the fluid component of magma originating from PAC.

1.3   Tectonic background of Izu-collision zone

IBM is the intraoceanic convergent system of the PAC and PHS plate with a length of about 2800 km between Sagami Bay and Guam as shown in Figure 1.1 (*Stern et al.*, 2003). PAC began to subduct below PHS at 43 Ma when PAC changed the subducting direction from north to west (*Richards and Lithgow-Bertelloni*, 1996). The backarc of IBM opened between 29 Ma and 15 Ma forming Parece Vela Basin (Figure 1.1) at the south of IBM (*Okino et al.*, 1998) and between 30 Ma and 15 Ma forming Shikoku Basin (Figure 1.1) at the north of IBM (*Okino et al.*, 1994). These backarc openings stopped at 15 Ma (*Okino et al.*, 1994, 1998) and at almost the same time, IBM started to collide with the Honshu Island (e.g., *Aoike*, 1999). IBM is colliding around Izu collision zone. Figure 1.4 shows the simplified geological background around Mt. Fuji after *Amano et al.* (2007). The Koma, Misaka, Tanzawa, and Izu block represent the accreted segments of collided IBM. Kofu Granitic complex and the Tanzawa Plutonic Complex are the lower crust of the IBM which were outcropped by the collision (Figure 1.4).   The last block, Izu peninsula, started to collide with Honshu Island at about 1 Ma (*Aoike*, 1999), and Pre-Komitake, the oldest body of Mt. Fuji started eruption at about 0.27 Ma (*Yoshimoto et al.*, 2010).

Kodaira et al. (2007) and *Takahashi et al.* (2009) obtained the P-wave velocity structure with an active source wide-angle seismic study along and across the pre-subducted IBM, respectively. These studies found a thickened middle crust of IBM consisting of tonalite with high SiO_2 content in the upper part of the middle crust and plutonic rocks with intermediate composition in the lower part the middle crust. *Kodaira et al.* (2007) showed that the thickness of the middle crust varies along arc from 3 to 13 km with a wavelength of 80–100 km with thicker middle crust below large basaltic volcanoes (e.g., Miyake-jima, Hachijo-jima) and thinner below submarine calderas (e.g., Kurose hole, Minami Hachijo). A crust-mantle transition layer, CMTL by *Takahashi et al.* (2009), with P wave velocity of about 7.2–7.6 km/s exists between the lower crust and the uppermost mantle slower than normal upper mantle. *Kodaira et al.* (2007) interpreted that CMTL consists of

mafic to ultramafic cumulates that is formed during the crustal evolution in IBM. Also, they found that the crust grows up to the width of about 25-30 km below basaltic volcanoes whose middle crust is thickened.

Tamura et al. (2010) and *Tamura* (2011) discussed the age of the plutonic rocks outcropped in the Izu collision zone, pre-collisional volcanic rocks of IBM, and volcaniclastic deposits of IBM drilled in the Ocean Drilling Program using major elements, rare earth element ratios, and isotropic data. They suggested that the middle crust of the IBM is delaminated from the lower crust during collision with the Houshu Island and remobilized, resulting in the accretion to the bottom of the crust of Honshu Island. In other words, they suggested that the upper and the middle crust of IBM is obducted or accreted to the overlying Honshu arc and only the portion below the lower crust of IBM subducts below the Honshu Island around Izu collision zone.

An active source wide angle reflection data lead *Arai* (2011) and *Arai et al.* (2014) to reveal that the top of the subducted IBM is the lower crust of IBM, supporting the idea of *Tamura et al.* (2010) and *Tamura* (2011). *Sato et al.* (2012) show from a compilation of seismic reflection and refraction studies that the upper boundary of the subducting PHS slab whose upper and middle crusts have been delaminated from the lower crust is about at depths of 20 km, 20 km to the northeast of Mt. Fuji.

1.4   Structural studies around Mt. Fuji

Lees and Ukawa (1992) found a broad low velocity region at depths between 15–32 km using the travel time tomography. Althouth they proposed that this deep low velocity region represents the subduction of the volcanic IBM, or a hot rising magma, the resolution is not good to discuss the detailed shape of the low velocity region.

Chung et al. (2009) calculated the attenuation structure around Mt. Fuji and showed that the intrinsic attenuation Q^{-1} near Mt. Fuji with radius of 5 km is lower than that of other volcanoes. Their results represent that magmatic activity of Mt. Fuji is not active.

From September to December in 2000 and from April to May in 2001, many deep-low-frequency seismic events occurred at depths of 11-16 km beneath Mt. Fuji (*Nakamichi et al.*, 2004; *Ukawa*, 2005). In response to the increase of LFEs in Mt. Fuji in 2000 and 2001, various observational campaigns had been conducted between 2001 and 2004 to understand the internal structure and magma plumbing system of Mt. Fuji.

Aizawa et al. (2004) found two distinct resistive bodies, representing the subducting PHS slab, which do not continue at a depth of about 20 km below the northeast of Mt. Fuji (Figure 1.5). Furthermore, they also found a large conductor below the epicenters of LFEs. Although they interpreted that the magma of Mt. Fuji ascends through a local gap of the PHS slab, the spatial resolution of their result in the depth direction is not good enough to confirm their interpretation.

Nakamichi et al. (2007) found from local seismic tomography that a region where both P and S wave velocities are low at a depth of about 7–17 km below Mt. Fuji. Because the Vp/Vs ratio in this region is not significantly larger than the surrounding areas, they interpreted the abundant volatile fluid is responsible for the reduction of seismic velocities in this region. Also, they pointed out the region with small Vp/Vs ratio where both P wave velocity and S wave velocity is low at a depth of about 15–25 km below Mt. Fuji (Figure 1.5). Although, they considered this region as a magma chamber, the resolution at depths more than 20 km is limited because of the sparse distribution of deep earthquakes used in this analysis.

Nakajima et al. (2009) estimated depths of the upper surface of the PAC and PHS around the Tokyo metropolitan area, Japan, using relocated interplate earthquakes and the travel-time tomography at depths down to 200 km. Their results show that the high velocity anomalies representing the PHS plate extend to depths between 60 and 130–140 km without a gap even in the north of the Izu-collision zone. They assumed that the PHS plate shows the low velocity anomaly above the depth less than 60 km because of the transformation of hydrous minerals in oceanic crust into eclogite. Around Mt. Fuji, the low velocity anomaly becomes very large and distributes from between 30 km and 100 km depth, so that the upper and lower boundary of the subducting PHS

slab just below Mt. Fuji is difficult to identify by their results.

1.5   The goal of this study

It is important to understand the magma plumbing system below Mt. Fuji to address why 1) the long-term eruption rate is much larger than other arc volcanoes in Japan, and 2) most of the ejected material from Mt. Fuji in last 10 Ka is basaltic as describe above.

Takahashi (2000) supposed that the magma plumbing model below Mt. Fuji is similar to that in the oceanic ridge. He proposed the subducting PHS plate is splitting below Mt. Fuji because the PHS plate subducts to the northwest along the Suruga trough, whereas subducts to the northeast along the Sagami trough (Figure 1.2). This model can explain the amount and the component of magma erupted from Mt. Fuji, because the huge amount of basaltic magma that is derived from the upper mantle through the splitting area in the PHS plate. However, the seismic tomography found the subducting PHS slab to a depth of about 140 km without gap (e.g., *Matsubara et al.*, 2005; *Nakajima et al.*, 2009) and does not support Takahashi's prospection. Other magma plumbing model of Mt. Fuji is that the magma chamber is deeper than 20 km as described above (*Fujii*, 2007). This model can explain the component of magma erupted from Mt. Fuji, but does not explain the significantly large eruption rate.

To clarify the magma plumbing system below Mt. Fuji, the seismic structure to a depth of about 60 km is very effective because previous studies did not successfully image the magma chamber of Mt. Fuji nor the structure of the subducting IBM with high resolution. Although seismic structure from travel-time tomography can, in theory, image whatever you want in an ideal condition, the travel-time tomography around Mt. Fuji does not achieve spatial resolution good enough to clarify the magma system deeper than 20 km because the seismicity below Mt. Fuji is low below 20 km (Figure 1.3).

In this study, we investigate the seismic structure below Mt. Fuji using a receiver function (RF) analysis. The RF method is an effective tool in the seismic investigation of velocity interfaces

such as the Moho boundary and has a higher resolution in detecting velocity boundaries than the travel-time tomography. Because this technique uses the body wave of teleseismic earthquakes, the velocity structure below seismograph stations in target area can be constrained without relying on the local seismicity. By executing the RF analysis around Mt. Fuji using a number of seismograph stations, we can get an entire image of the magma chamber and the IBM structure that were not detected by a travel time tomography in previous studies.

The purpose of this study is to gain more insight into the magma plumbing system below Mt. Fuji using the seismic structure of the magma chamber and the subducting IBM revealed by the RF analysis. In Chapter 2, the theory of the RF analysis used in this study is reviewed. We explain the details of seismograph stations and the teleseismic earthquakes used in this study in Chapter 3. In Chapter 4, distinct velocity boundaries around Mt. Fuji are revealed by projections of radial RF amplitudes onto cross sections around Mt. Fuji. In Chapter 5, S-wave velocity models are inverted using radial RFs by the Monte Carlo Method. Comparisons of results in our studies with those in previous studies and the magma plumbing system of Mt. Fuji are discussed in Chapter 6.
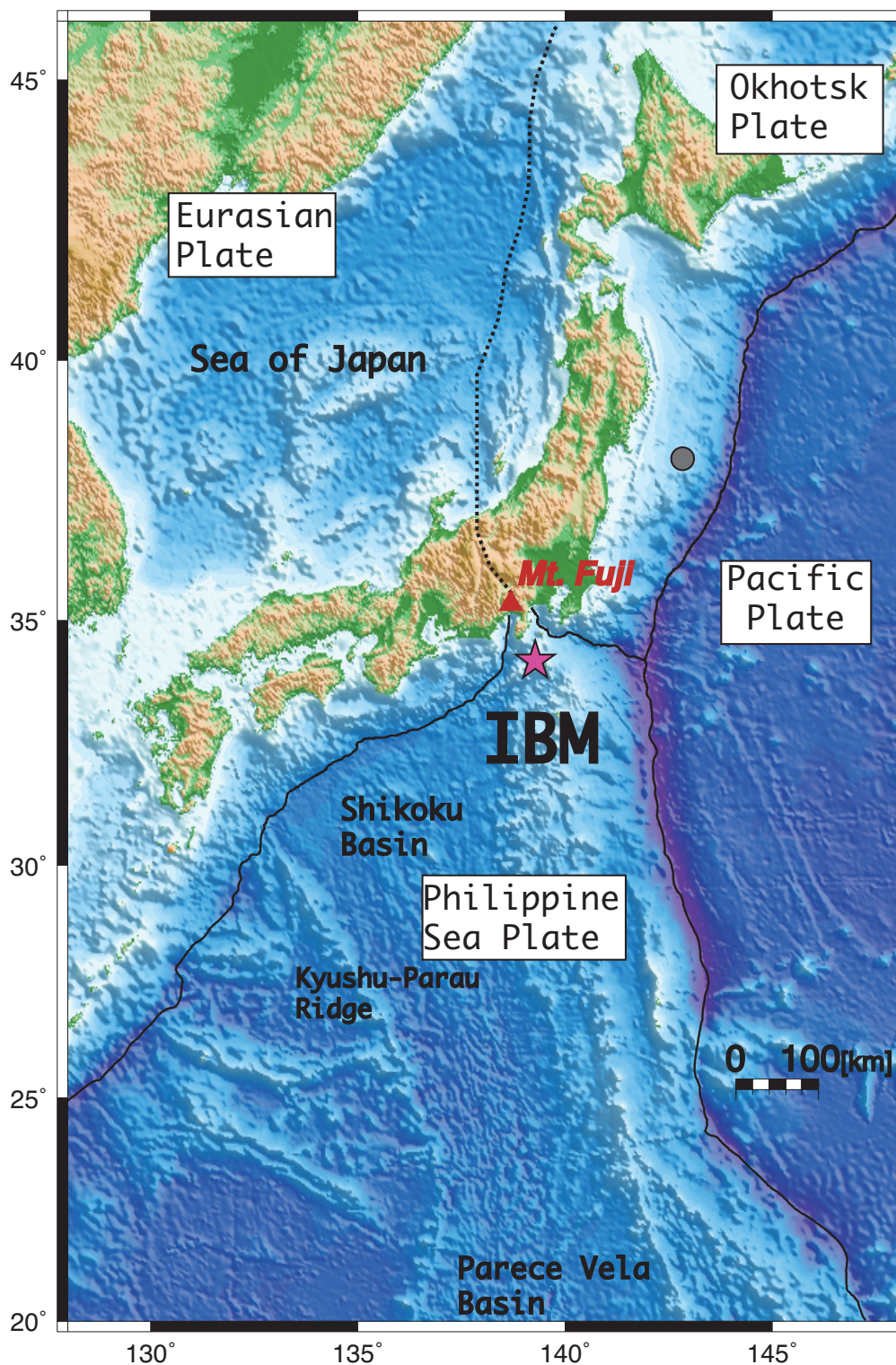
Figure 1.1: The tectonic background around Mt. Fuji.
Active plate boundaries around the Japanese island. Black dot line represents the plate boundary between the Eurasian plate and the Okhotsk plate from *Seno et al.* (1996). The red triangle, the pink star, and the gray circle show locations of Mt. Fuji, the dike intrusion between Miyake-jima and Kozu-shima in 2000 (*Sakai et al.*, 2001), and the hypocenter of the 2011 Tohoku-Oki earthquake.
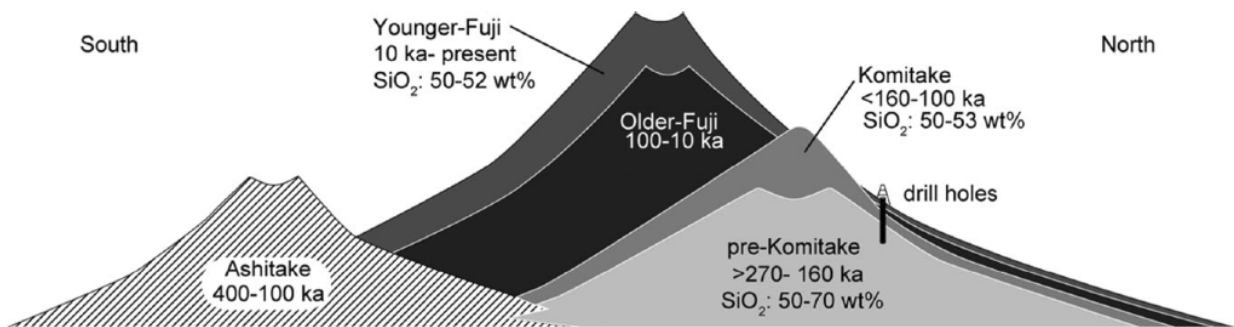
Figure 1.2: Schematic cross section of Mt. Fuji.
Eruption times and amounts of SiO2 of each volcanic pile are listed. After *Yoshimoto et al.* (2010)
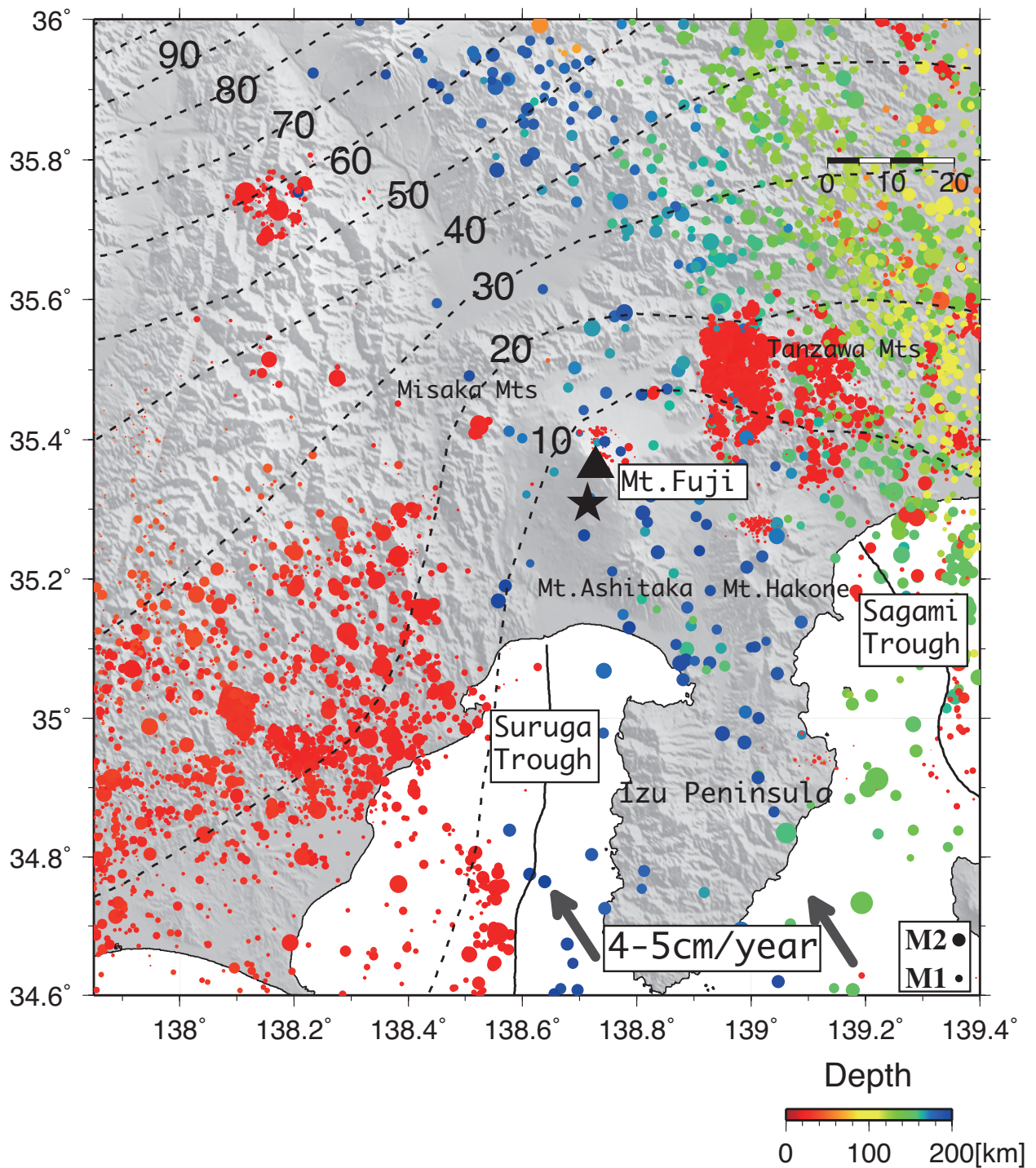
Figure 1.3: Tectonic setting around Mt. Fuji.
Depth contours indicate the upper surface of the subducting Philippine Sea (PHS) plate estimated by *Nakajima et al.* (2009). Color circles show hypocenters with a magnitude 0.1 or larger at depths between 20 and 200 km, occurred from 2001 to 2005 located by JMA. The colors and sizes of circles represent depths and magnitudes of events. Gray arrows show the relative plate motion between the PHS plate and the Eurasian plate (*Seno et al.*, 1993). The black triangle, black star, and black solid lines represents Mt. Fuji, the hypocenter of East-Shizuoka earthquake, and Suruga and Sagami troughs.
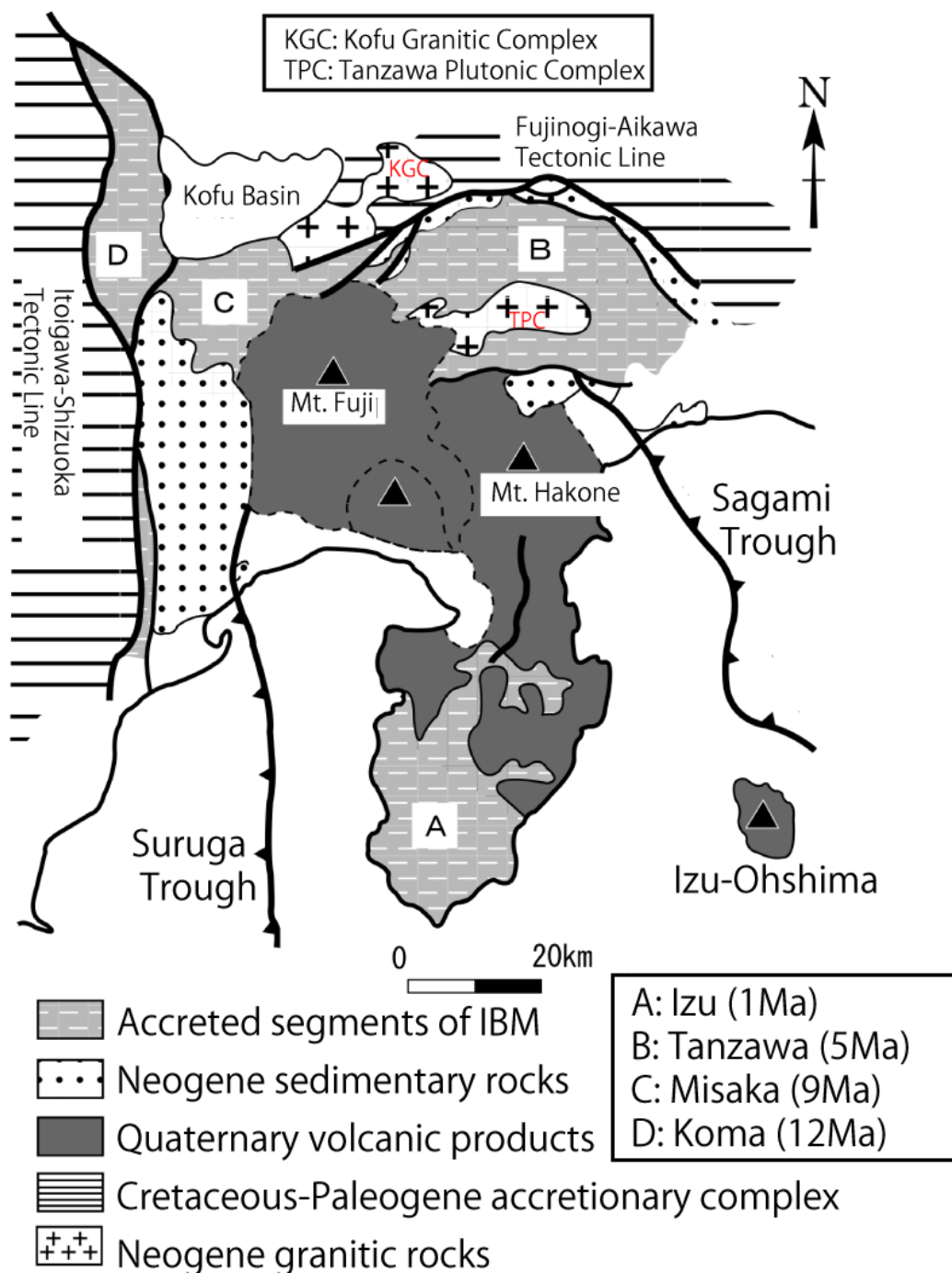
Figure 1.4: Geological background around Izu collision zone after *Amano et al.* (2007).

(a) Resistivity (Aizawa et al. 2004)   (b) Vp/Vs (Nakamichi et al. 2007)
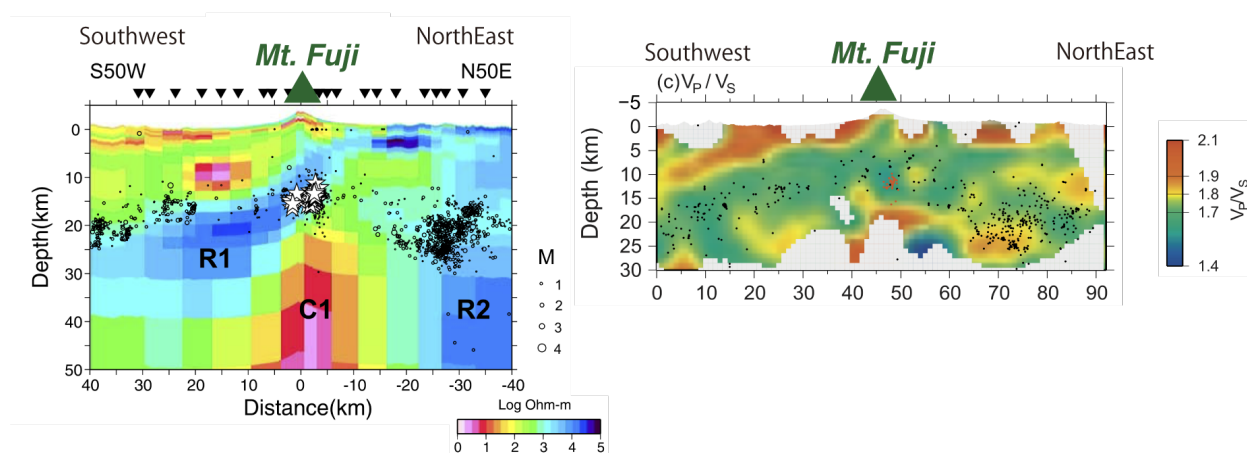
Figure 1.5: Previous studies of Mt. Fuji.
(a) Resistivity structure below Mt. Fuji after *Aizawa et al.* (2004). (b) Vp/Vs ratio below Mt. Fuji after *Nakamichi et al.* (2007).

2 Receiver Function Analysis

2.1 The definition of Receiver Function

The Receiver function (RF) analysis is a popular method to estimate the depth and the velocity contrast of distinct boundaries below seismic stations. A teleseismic P wave is followed by many Ps converted waves (e.g., Ps, PpPs, PpSs, PsPs) which are generated at velocity boundaries beneath receivers. RFs are calculated by deconvolving horizontal components of the teleseismic wave from vertical components (*Langston*, 1979). Displacements of the teleseismic wave are represented as follows;

$$Z(t) = S(t) * I(t) * E_z(t) \tag{2.1}$$

$$R(t) = S(t) * I(t) * E_r(t) \tag{2.2}$$

$$T(t) = S(t) * I(t) * E_t(t) \tag{2.3}$$

where $Z(t)$, $R(t)$, $T(t)$ are the vertical, radial, and transverse components of displacement in time domain, respectively. $S(t)$, $I(t)$, and $E_{z,r,t}(t)$ represent a source time function, an impulse response of the instruments and impulse responses of the structure at each component, respectively, where $*$ represents the convolution. The radial and transverse RFs in frequency domain $H_R(\omega)$, $H_T(\omega)$ are defined as follows (*Langston*, 1979);

$$H_R(\omega) = \frac{R(\omega)}{Z(\omega)} = \frac{E_r(\omega)}{E_z(\omega)} \tag{2.4}$$

$$H_T(\omega) = \frac{T(\omega)}{Z(\omega)} = \frac{E_t(\omega)}{E_z(\omega)} \tag{2.5}$$

where $Z(\omega)$, $R(\omega)$, $T(\omega)$ and $E_{z,r,t}(\omega)$ are the vertical, radial, transverse components of displacement and impulse responses of the structure at each component in frequency domain, respectively. This deconvolution removes P-multiples wave (e.g., PpPp) and isolates mode-converted waves (e.g., Ps, PpPs, PsPs and so on), because the incidence angle of teleseismic waves is near vertical

so that the vertical component of a teleseismic wave is composed of almost only P wave (*Ammon*, 1991). Time domain RFs can be estimated by computing the inverse Fourier transform of the frequency domain RFs expressed in equation (2.4) and (2.5).

2.2   The time separation between direct P and Ps converted waves

The time of RFs represents the lag time of converted waves from the arrival of the direct P wave. The arrival times of Ps, PpPs, PpSs and PsPs in RFs converted at a velocity boundary at a depth of H are represented in following equations (*Zhu and Kanamori*, 2000):

$$T_{Ps} = H\left[\sqrt{\frac{1}{Vs^2} - p^2} - \sqrt{\frac{1}{Vp^2} - p^2}\right] \tag{2.6}$$

$$T_{PpPs} = H\left[\sqrt{\frac{1}{Vs^2} - p^2} + \sqrt{\frac{1}{Vp^2} - p^2}\right] \tag{2.7}$$

$$T_{PpSs,PsPs} = 2H\sqrt{\frac{1}{Vs^2} - p^2} \tag{2.8}$$

where p, Vp and Vs represent the ray parameter, and the P and S wave velocity over the velocity boundary, respectively. These equations convert RFs in time domain to those in depth domain using a horizontally-layered seismic structures below the stations.

2.3   The amplitude of converted phase in RFs

Julia (2007) formulated the amplitude of Ps, PpPs and PpSs phase in RFs normalized by that of the direct P phase using approximations of reflection/transmission coefficients at velocity and density contrasts (*Aki and Richard*, 2002). Normalized amplitudes of converted phases, $\overline{A}$, in RFs over a simple 2-layered structure are as follows:

$$\overline{A_{Ps}} = \frac{\overline{Vp}}{4Vs_0}\left[\frac{4\overline{Vs}}{\overline{Vp}}\frac{\Delta Vs}{Vs} - \left(1 - \frac{2\overline{Vs}}{\overline{Vp}}\right)\frac{\Delta\rho}{\overline{\rho}}\right] \tag{2.9}$$

$$\overline{A_{PpPs}} \;=\; \frac{\overline{Vp}}{4Vs_0}\left[\frac{4\overline{Vs}}{\overline{Vp}}\frac{\Delta Vs}{\overline{Vs}} + \left(1 + \frac{2\overline{Vs}}{\overline{Vp}}\right)\frac{\Delta\rho}{\overline{\rho}}\right] \tag{2.10}$$

$$\overline{A_{PpSs}} \;=\; -\left[\frac{\Delta Vs}{\overline{Vs}} + \frac{\Delta\rho}{\overline{\rho}}\right] \tag{2.11}$$

where

$$\overline{Vp} \;=\; \frac{Vp_1 + Vp_2}{2} \tag{2.12}$$

$$\overline{Vs} \;=\; \frac{Vs_1 + Vs_2}{2} \tag{2.13}$$

$$\overline{\rho} \;=\; \frac{\rho_1 + \rho_2}{2} \tag{2.14}$$

$$\Delta Vp \;=\; Vp_2 - Vp_1 \tag{2.15}$$

$$\Delta Vs \;=\; Vs_2 - Vs_1 \tag{2.16}$$

$$\Delta\rho \;=\; \rho_2 - \rho_1 \tag{2.17}$$

Here, Vp_1, Vs_1, ρ_1, Vp_2, Vs_2 and ρ_2 represent P and S wave velocities and densities above and below the boundary, and Vp_0 and Vs_0 represent P and S wave velocities at near surface, respectively. These expressions indicate that amplitudes of Ps, PpPs and PpSs converted phases in RFs have almost no sensitivity to the perturbation of P wave velocity. In equation (2.9), $(1 - 2\overline{Vs}/\overline{Vp})$ is much less than $4\overline{Vs}/\overline{Vp}$ in a realistic velocity structure so that the normalized amplitude of the Ps converted phase in RFs is proportional to the contrast of the S wave velocity at the velocity boundary, $\Delta Vs/\overline{Vs}$. On the other hand, the amplitudes of the PpPs and PpSs phases are sensitive to both the contrasts of S wave velocity and density at the boundary, $\Delta Vs/\overline{Vs}$ and $\Delta\rho/\overline{\rho}$.

Also, Numerical experiments by *Julia* (2007) indicate that if the velocity changes gradually within a range of width, RFs can separate converted phases from each velocity variation in high frequencies. On the other hand, RFs consider the gradual variation of velocities as one velocity boundary in low frequencies.

2.4   Multiple-taper correlation method

Although the definition of RFs in equations (2.4) and (2.5) is very simple, it is difficult to compute RFs in a reliable manner because a division by a raw spectral is unstable at spectral holes. Various numerical methods to calculate RFs have been suggested to enable a reliable estimation of spectral divisions by reducing the influence of spectral holes (e.g., *Shibutani et al.*, 2009) including water level method (*Helmberger and Wiggins*, 1971), time domain deconvolution method (*Gurrola et al.*, 1995), Multiple taper Correlation (MTC) method (*Park and Levin*, 2000), and multivariate autoregressive method (*Shiomi et al.*, 2004) and so on. The width of the low velocity layer below Mt. Fuji is estimated to be about 10 km (*Nakamichi et al.*, 2007; *Kinoshita et al.*, 2015) so that high frequency data need to be used in this study. We adopt MTC method proposed by *Park and Levin* (2000) because this method resists the spectral leakage and estimate valuable RFs at the frequencies where the P wave spectrum have low-amplitude. In the MTC method, an orthonormal sequence of tapers called as Slepian tapers (*Slepian*, 1983) is designed to minimize spectral leakages. The set of Slepian tapers and the associated eigenspectra can be combined to reduce the variance of the overall spectrum estimate (*Park et al.*, 1987). We set the parameters of the MTC method appropriate for the velocity boundaries above 100 km depth according to *Park and Levin* (2000).

$$p \quad = \quad 2.5 \tag{2.18}$$

$$K \quad = \quad 3 \tag{2.19}$$

where p and K represent time-bandwidth product and the number of order of Slepian tapers to calculate spectrals, respectively. We explain the details of these parameters in Apendix A.

A disadvantage of the MTC method is that the amplitude of RF decays at longer lags and finally the polarity is reversed because of the shape of tapers. *Helffrich* (2006) showed that MTC generates RFs that are reliable in only the first 10 seconds in the case of using 60 seconds of tapers,

and proposed an extended-time multi-taper technique with many sets of 10-second Slepian tapers overlapping with neighboring windows by 50 %. These sets of tapers do not decay the amplitude of RFs at long lag time, allowing us to detect converted phases from depth such as mantle transition zones. Since this study investigates the velocity structure at the depths less than 100 km beneath Mt. Fuji with RF phases of lag times less than 10 seconds, the simple MTC method by *Park and Levin* (2000) is enough to estimate the structure.

2.5   Estimation of velocity structure using RFs

There are three kinds of RF analyses to estimate velocity structures beneath seismic stations (e.g., *Igarashi et al.*, 2011): imaging of the RF amplitude along cross-sections, $H - \kappa$ stacking method, and waveform inversion method.

First, the depth and shape of distinct velocity boundaries can be estimated by tracing many RF amplitudes along ray paths with an assumed velocity model. In this method, a RF is assumed to consist of direct and Ps waves only because the amplitude of multiple phases are less than that of Ps, and the time-to-depth conversion is performed using equation (2.6). With this method, various studies have successfully imaged the Moho boundary in continental and oceanic plates beneath Japan Islands (e.g., *Yamauchi et al.*, 2003; *Shiomi et al.*, 2004).

Second, *Zhu and Kanamori* (2000) used amplitudes of RFs to estimate the crustal thickness H and Vp/Vs ratio κ. They searched the maximum value of weighted sum of the phases at predicted arrival times of Ps, PpPs, PsPs and PpSs with different H and κ. This method assumes the constant P and S wave velocity over the velocity boundary and thus inappropriate for RF analyses in regions with complicated velocity structure like collision zones and active volcanoes.

Third, inversions of RF waveforms can estimate absolute seismic velocity structure beneath seismic stations. *Ammon et al.* (1990) linearized the non-linear observation equation relating RFs and seismic velocities by iteratively correcting model parameters from the initial model that is close to the true earth velocity structure. They indicated that there is a trade-off between the

average velocity over the velocity boundary and the depth of the boundary. Also, this linearized method has a problem that the final solution strongly depends on the initial model and smoothing constraints. Previous studies have improved the inversion methods as discussed in Chapter 5.

This study images the depth and shape of velocity boundaries below Mt. Fuji using a number of seismic stations and teleseismic events from cross sections of RF amplitudes and estimate absolute S wave velocities through the RF waveform inversion.

3   Data used in this study

We used teleseismic waveform data recorded at 156 seismic stations deployed around Mt. Fuji by five institutes: Earthquake Research Institute, The University of Tokyo (ERI), Japan Meteo-rological Agency (JMA), National Research Institute for Earth Science and Disaster Prevention (NIED), Hot Spring Research Institute of Kanagawa Prefecture, and Nagoya University (Figure 3.1). Each station is equipped with a three-component short-period or a broadband seismometer. Some stations near Mt. Fuji were operated by scientists at national universities in Japan between September 2002 and April 2005 to execute dense seismic observation of Mt. Fuji (*Nakamichi et al.*, 2004). Most seismic stations of NIED used in this study are Hi-net stations and the orien-tations of Hi-net seismometers installed at the bottom of boreholes were corrected using the result due to *Shiomi* (2012).

A global earthquake catalogue edited by the National Earthquake Information Center, United States Geological Survey was used to extract teleseismic events with magnitudes larger than 6.0 and epicentral distances between 20 and 90 degrees from Mt. Fuji from October 2002 to December 2010 for the RF analysis. Event selection is based on the criteria that the number of stations with clear P arrivals checked manually is greater than or equal to 4 for each event. The total number of teleseismic event used in this study is 793 and the number of events at each station is from 24 to 690, depending on the signal-to-noise ratio and the deployment time. Figure 3.2 shows the distribution of teleseismic events used in this study.
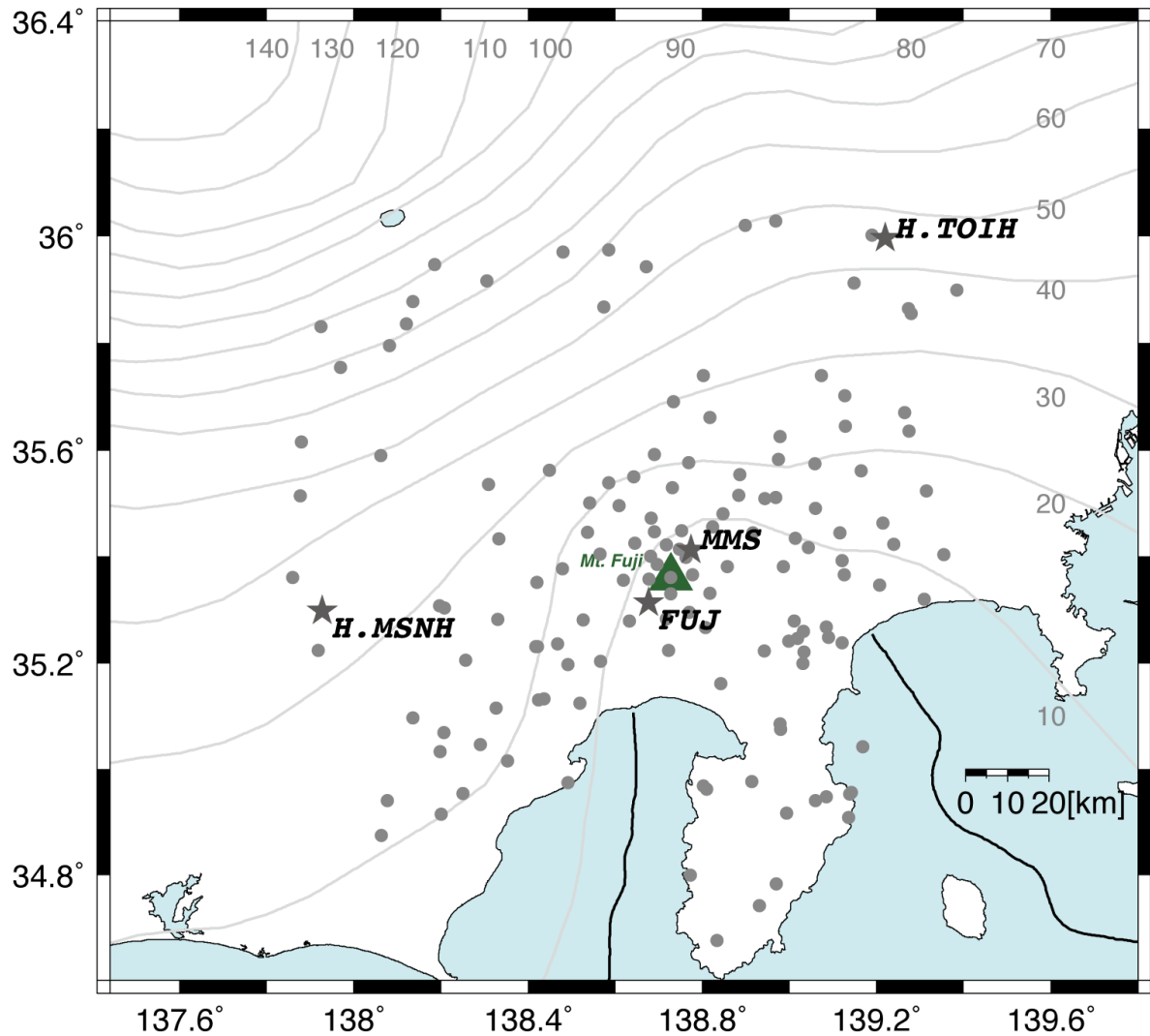
Figure 3.1: Distribution of the seismograph stations used in this study.
Gray circles represent seismic stations operated by five institutes: ERI, JMA, NIED, Hot Spring Research Institute of Kanagawa Prefecture and Nagoya University. A green triangle represents Mt. Fuji. Four gray stars are stations used in Chapter 4 as RF examples. Black solid line represents Suruga and Sagami troughs, and gray solid lines with numbers are the upper boundary of subducting PHS plate estimated in *Nakajima et al.* (2009).
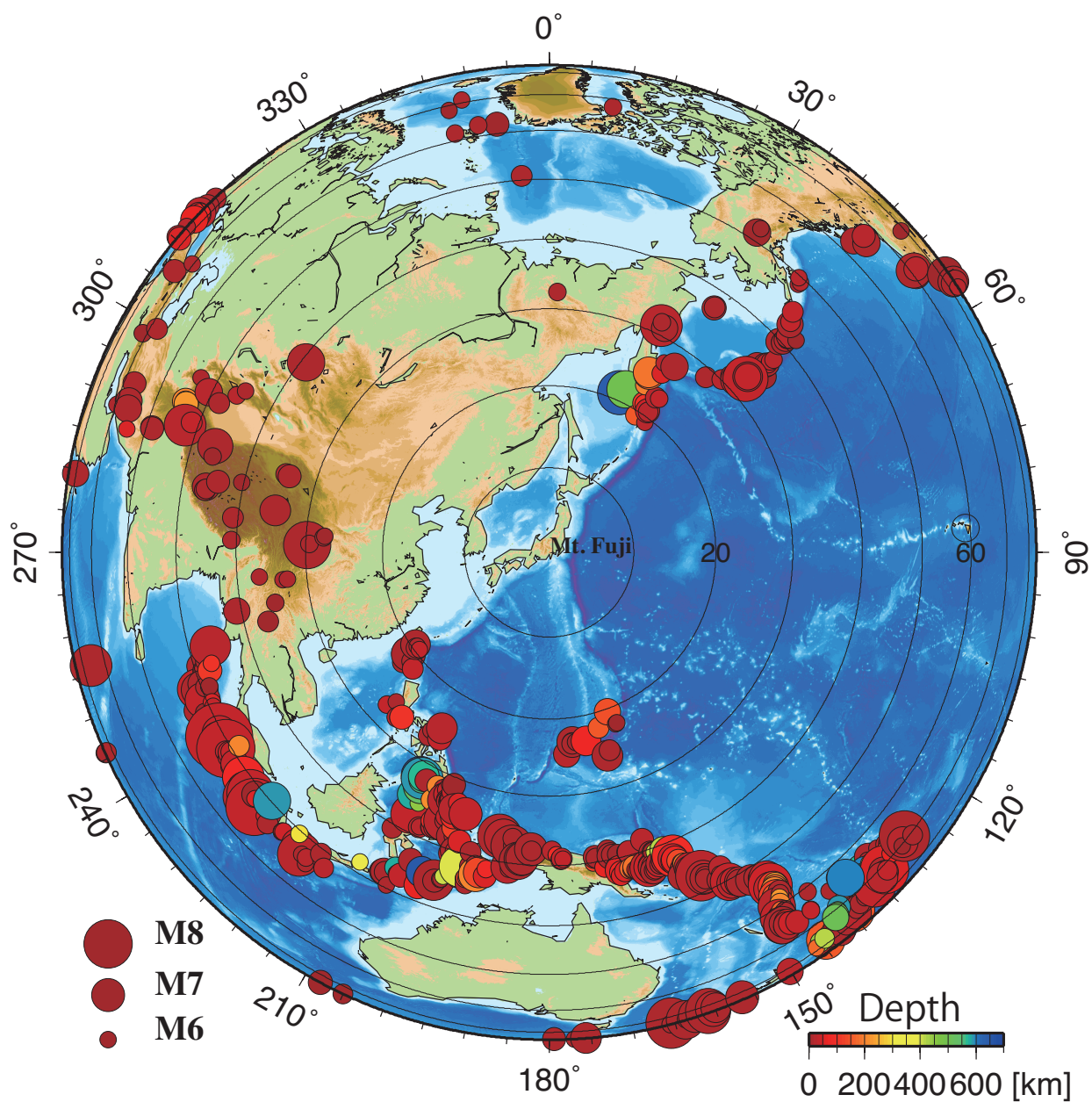
Figure 3.2: Distribution of epicenters of the 793 teleseismic events used in this study.
Each circle represents the location of the hypocenter. Black solid lines represent epicentral distance
(degrees) from Mt. Fuji. The color and sizes of circles represent depths and magnitudes of events.

4   Observation of Receiver Functions

Characteristics of RFs at some stations and cross sections of radial RF amplitudes were previously discribed in *Kinoshita et al.* (2015). The numbers of teleseismic events and seismograph stations used in this study were changed from those in *Kinoshita et al.* (2015). We extracted two 80-second windows, one ends 15 seconds before the expected P-wave arrival from the Ak135 velocity model (*Kennett et al.*, 1995) and the other starts right after the one, as the noise and signal windows, respectively, from teleseismic waveforms recorded at 156 stations (Figure 3.1). After pre-processing such as mean removal, de-trend, and rotation to the great circle path, total of 71533 radial and transverse RFs are calculated using MTC method (*Park and Levin*, 2000) as described in Chapter 2.

4.1   Examples of Receiver Functions

An isotropic and horizontally layered structure gives radial RFs which are independent of the arrival direction and transverse RFs with an amplitude of zero. In reality, however, derived transverse RFs have non zero amplitude and the shape both radial and transverse RFs depend on arrival directions. To reduce the noise and azimuthal dependency in derived RFs, we calculate weighted means of RFs with similar arrival directions by setting bins with a width of 10 degrees and spacing of 5 degrees. Each RF is weighted according to the inverse variance in frequency domain (*Park and Levin*, 2000). Composite RFs thus calculated are filtered by a cosine-squared low-pass filter with a cut-off frequency of 1.0 Hz to avoid Gibbs-effect ringing in the RFs. This procedure obtains a total of 7168 stacked RFs in both radial and transverse components. Figure 4.1 shows an example of radial (left) and transverse (right) RFs lined up with back azimuth at four stations marked by star signatures in Figure 3.1.

In general, a positive and negative amplitudes of the radial RFs shown in red and blue in Figure 4.1 are interpreted as velocity interfaces below which the velocity is higher and lower than the

upper layer, respectively. A dipping and anisotropic structure can generate the energy in transverse RFs. Transverse RFs aligned with back azimuths gives common polarity reversals of a focusing phase if dipping boundaries or anisotropic materials exist below the stations (e.g., *Levin and Park*, 1997; *Savage et al.*, 2007). On the other hand, the dipping isotropic structure causes the 2-lobed back azimuthal pattern in transverse RFs whose periodicity is 360 degree. The anisotropic flat structure results in two kinds of periodicity (*Levin and Park*, 1997): 2-lobed back azimuthal pattern whose periodicity is 360 degree caused by a dipping anisotropy symmetry axis, and 4-lobed back azimuthal pattern whose periodicity is 180 degree caused by a horizontal anisotropy symmetry axis. Below radial and transverse RFs of selected seismic sites shown in Figure 3.1 are examined.

4.1.1   Station H.MSNH

RFs at the station H.MSNH show distinct positive amplitudes at 2-3 and 4-6 seconds in the radial component. The distinct positive phase at about 4-6 seconds in the radial component can be considered as a Ps conversion from the Moho boundary of the PHS plate, considering that a travel time tomography of *Nakajima et al.* (2009) gives the upper surface of subducting PHS below H.MSNH at about a depth of 35 km , the crustal thickness of normal oceanic plates is 5-7 km, and thus the Moho depth of the subducting PHS there is at around 40 km. Also, the arrival times from the Moho vary with the arrival direction: about 6 seconds from the northern direction (back azimuth of 300 degrees) and about 4 seconds from the southern direction (backazimuth of 210 degrees). Furthermore the transverse phase at about 6 seconds changes polarity at about 210 degree. These observations reflect the dipping Moho boundary from south to north below H.MSNH.

4.1.2   Station H.TOIH

The station H.TOIH has distinct positive phases in radial RFs at about 2 and 4-5 seconds, representing velocity boundaries in the continental crust such as the Conrad and Moho boundaries. The Moho depth in the subducting PHS plate below H.TOIH is likely to be at about 50 km depth con-

sidering the depth of the upper boundary of the PHS plate at about 45 km (*Nakajima et al.*, 2009). The Moho phase of the PHS plate cannot clearly be detected because of multiple reverberations from the velocity interfaces in the continental crust.

4.1.3   Station MMS

Radial RFs at the station MMS, to the northeast of Mt. Fuji (Figure 4.1c), multiple reverberations generated by thick volcanic sediment layers below Mt. Fuji shift the direct P pulse from zero time lag and broad the pulse width (*Cassidy*, 1992). There are distinct positive phase at both 3 and 6 seconds in radial RFs, representing a positive velocity boundary below the station. Transverse Ps pulses at 3 second change polarity at about 210 degree. Also, the polarity of transverse pulses at 6 seconds changes at between 50-125, about 160 and 180 degrees. The transverse phase at 3 seconds shows almost 2-lobed pattern whose periodicity is 360, that is, the transverse phases at 3 seconds is positive at the backazimuth between 215 and 315 and those is negative at the backazimuth between 30 and 210. These characteristics represent isotropic dipping structure or anisotropic flat structure with tilted symmetry axis as described above. On the other hand, the transverse phase at 6 seconds shows almost 4-lobed pattern, representing anisotropic flat structure with horizontal symmetry axis or anisotropic dipping structure with tilted symmetry axis.

4.1.4   Station FUJ

At the station FUJ, to the southwest of Mt. Fuji, the direct P pulse shifts toward a positive time with a broadened shape caused by a volcanic sediment layer as is the case with the station MMS discussed above. The amplitude of radial and transverse RFs of FUJ is larger than MMS, representing differences of basement structure between northeast and southwest of Mt. Fuji (*Kagiyama*, 2007). There are distinct positive phases in radial RFs at about 4 and 6 seconds. The transverse Ps pulse at 4 second change polarity at about 50, 190, 220, 280 degree The transverse Ps pulse at 6 second change polarity at about 50, 190, 220, 280 degree. The transverse phase at 4 and 6 seconds shows almost 4-lobed pattern, representing anisotropic flat structure with horizontal symmetry axis

or anisotropic dipping structure with tilted symmetry axis.
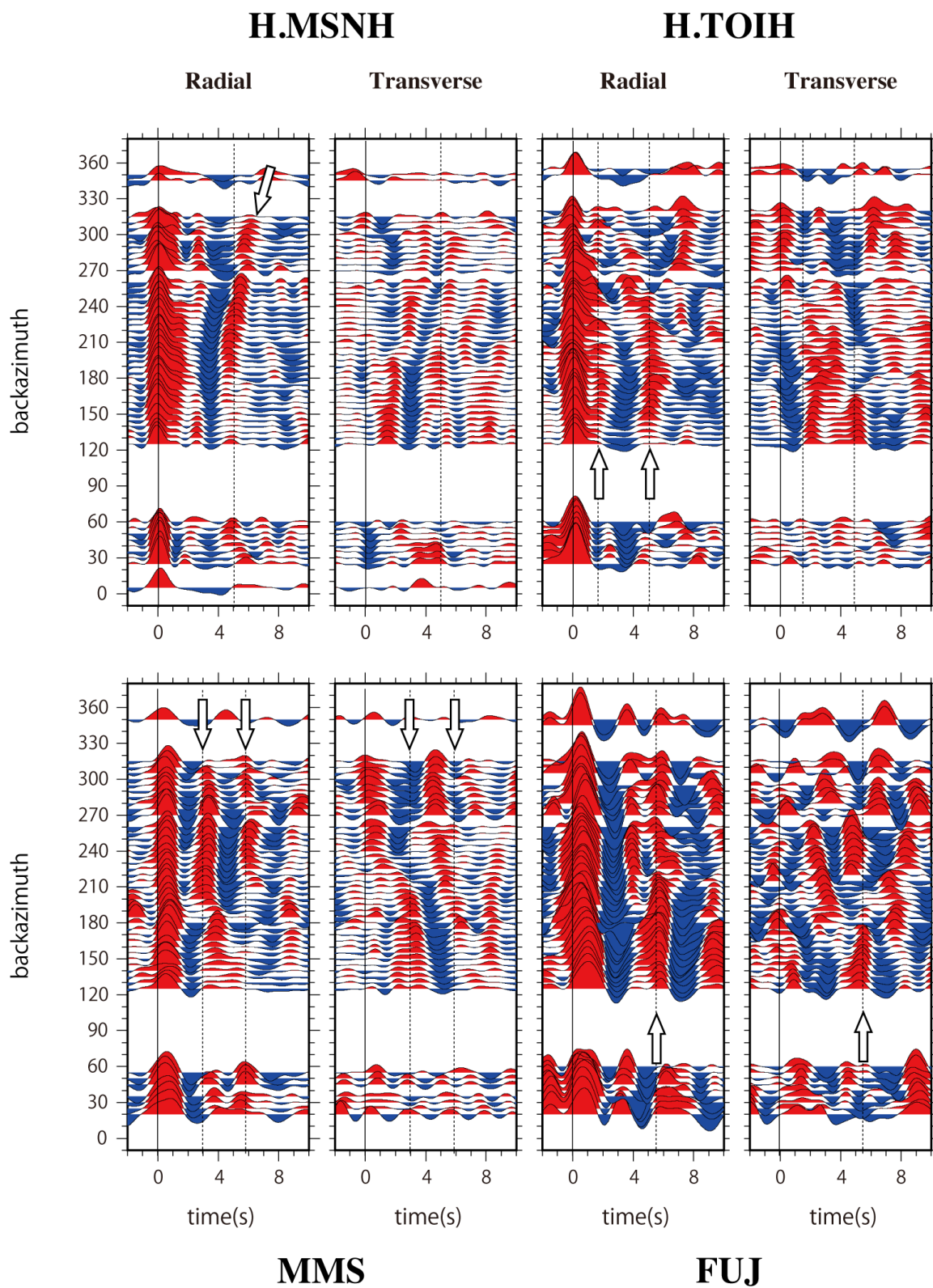
Figure 4.1: Examples of radial and transverse RFs at four stations.
Stations H.MSNH and H.TOIH are operated by NIED far from Mt. Fuji and stations MMS and FUJ are operated by ERI near Mt. Fuji. The vertical and horizontal axis represent back azimuths and delay times, respectively. Red and Blue are positive and negative velocity boundaries, respectively. White arrows are distinct phases discussed in the text.

4.2   Cross sections of Receiver Functions

Many previous studies have imaged the depth distributions of seismic velocity boundaries from radial RFs' amplitude using densely installed seismic stations (e.g., *Yamauchi et al.*, 2003; *Shiomi et al.*, 2004). The time axis of RFs can be converted to the depth axis by assuming velocity structures below each station using equation (2.6). In this study, we converted the lag time in RFs to the depth with P and S velocities beneath each station by Nakamichi et al. [2007] and those employed in the earthquake locations by JMA (*Ueno et al.*, 2002) in areas where the seismic velocities by *Nakamichi et al.* (2007) are not available. Ray parameters for each event-station pair are calculated using the AK135 model (*Kennett et al.*, 1995). RFs are high-pass filtered using a zero-phase second order butterworth filter with a cutoff frequency of 0.1 Hz, depth converted, and mapped along their ray paths of the S-wave with Snell's law through a flat-layered velocity model used in the time-depth conversions. The bin widths are set as 4 km in horizontal, 1 km in depth, and 20 km in perpendicular to the direction of cross section. If more than one ray path intersects the same bin, the RF amplitudes are averaged in each bin. Then, the amplitude in each grid is averaged with those in the right and left grid, that is, the amplitudes are averaged over 12 km in horizontal direction.

Figures 4.3-4.5 show examples of RF cross sections along the lines in Figure 4.2a-g. White solid lines in the cross sections (Figure 4.5) indicate positive amplitude (red color) found in this study, representing positive velocity boundaries. White broken lines represent the upper surface of subducting PHS plate estimated by *Nakajima et al.* (2009). We hereinafter call the boundaries between the crust and the mantle as "Moho boundary" where back-arc and fore-arc are subducting, that is, the normal oceanic plate with the thin oceanic crust over the mantle are subducting below a continental plate. By contrast, we do not use the word "Moho" where IBM are colliding and subducting because *Kodaira et al.* (2007) and *Takahashi et al.* (2009) found CMTL between the crust and the mantle below IBM (as described in Chapter 1) and it is difficult to define the Moho

boundary below IBM.

The southeast-northwest (SE-NW) cross-sections show positive velocity interfaces at 20–120 km in Line a (phase a1 in Figure 4.5a) and at 50–120 km in Line b (phase b2 in Figure 4.5b) , suggesting a velocity boundary subducting from the southeast to northwest. Comparing the upper boundary of the PHS plate with hypocenters indicated by gray dots shows that these interfaces represent the Moho boundary of the subducting PHS slab. Similarly, there are distinct positive phases representing the Moho about 10 km beneath the top of the subducting PHS plate on the southwest-northeast (SW-NE) cross sections at 80–120 km in Line f (phase f2 in Figure 4.5f) and at 90-130 km in Line g (phase g2 in Figure 4.5g).

Below the region where the IBM collides with central Japan, distinct continuous positive phases are seen at depths between 40 and 60 km (phase b1 in Line b, phase c1 in Line c, phase d1-d3 in Line d, phase e1-e3 in Line e, phase f1 in Line f, and phase g1 in Line g in Figure 4.5). *Kodaira et al.* (2007) obtained a seismic velocity structure of the crust and uppermost mantle of the IBM before subduction that reveals the existence of a 10 km thick middle crust below basaltic volcanoes. They suggest that the upper boundary of the uppermost mantle is at the depth of about 30–35 km beneath volcanic islands. Considering the volume of Izu peninsula and the influence of collision, we interpret the positive phases at 40 km depth below the Izu collision zone as the upper boundary of the mantle in IBM. Ps polarity of radial RFs is sometimes reversed when the interface dips larger than about 30 degree (*Abe et al.*, 2010). The PHS plate subducts steeply to the northwest of our study region, so that positive Moho phase does not continued to a depth more than 80 km in Figure 4.5. Both the Moho of subducting PHS slab and the upper boundary of the mantle of IBM show the discontinuities (between phase d1 and d2 in Line d, between phase e1 and e2 in Line e, phase f1 in Line f, phase g1 in Line g in Figure 4.5), whereas the Moho of PHS shows a continuous image in south-west Japan (e.g., *Shiomi et al.*, 2004). Those characteristics strongly suggest the structural complexity of subducting PHS in area where IBM with thick arc crust collides and subducts. On the other hand, the velocity boundary of the mantle of IBM in Line

c (phase c1) shows the continuous positive phase without gap, representing the collision of IBM is different between western and eastern part. The discontinuities of positive velocity boundaries in RF images (the gap between phase b1 and b2 in Line b, phase d1 and d2 in Line d, and phase e1 and e2 in Line e) might reflect the existence of a low velocity zone above the positive phases that is not included in the assumed velocity model. For example, if there is a low velocity region above phase d2 in Line d, the phase d1 and d2 become continuous. However, the gap of positive phase (indicated by white arrows between phase d2 and d3 in Line d and between phase e2 and e3 in line e) could not be explained only by the existence of low velocity region, suggesting the gap of positive velocity boundaries. In Line d and e, another positive phases are found at depths of 20–30 km (phase d4 and e4 in Figure 4.5), representing the local positive velocity boundary. Just above the velocity boundary represented as phase d4 in Line d, LFEs of Mt. Fuji indicated as pink circles occurred (*Nakamichi et al.*, 2007).

Figures 4.6-4.8 show the RF cross sections in the radial component around Mt. Fuji along lines A-D in Figure 3.2 with a cut-off frequency of 1 Hz. RF images around Mt. Fuji have similar features in all directions, with distinct and broad positive and negative amplitudes at the depth of 0–10 km and 10–20 km, representing that are caused by thick volcanic sedimentary layers erupted from Mt. Fuji. As described in Figure 4.5, there are positive phases representing the Moho where back-arc and fore-arc, that is, normal oceanic plate subducts in Figure 4.8 (phase A1 in Line A, phase B1, B6 in Line B). The discontinuities of positive velocity boundaries (between phase B2 and B3, B5 and B6 in Line B, between C1 and C2 in Line C) show the complexity of the velocity structure of subducting IBM and imply the existence of a low velocity region. Figure 4.8 also reveals a gap in the positive velocity boundaries at a depth of 40 km just below Mt. Fuji as shown by white arrows. Above the gap, there is a high-velocity boundary at a depth of 20–30 km in all directions (phase B4, C3, D2 in Figure 4.8) just beneath the region, where LFEs of Mt. Fuji are located.
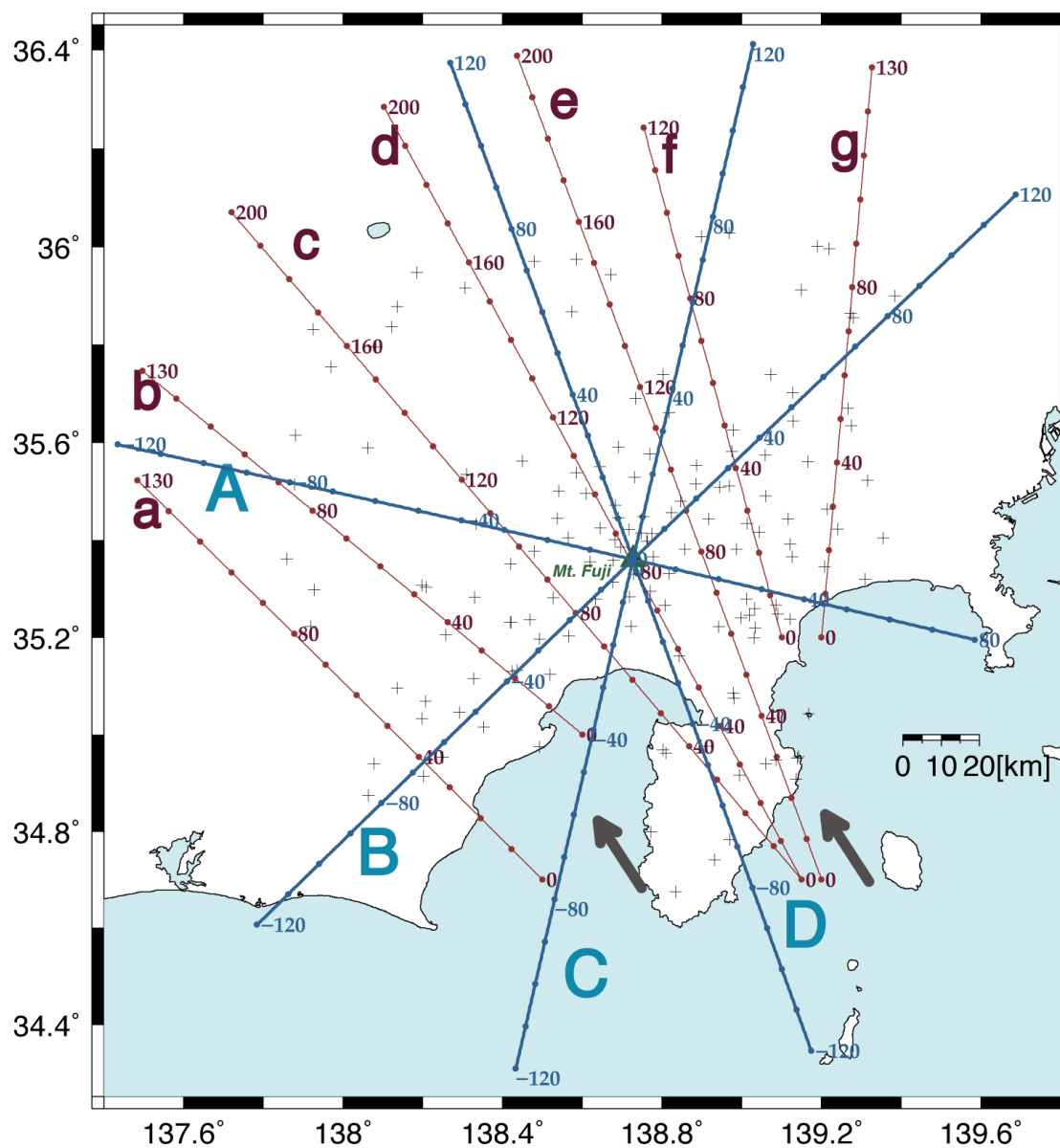
Figure 4.2: Locations of the cross sections of the radial RF amplitudes.
Red and blue solid lines represent the locations of cross sections in Figure 4.5 and 4.8, respectively.
Cross denotations represent seismograph stations.
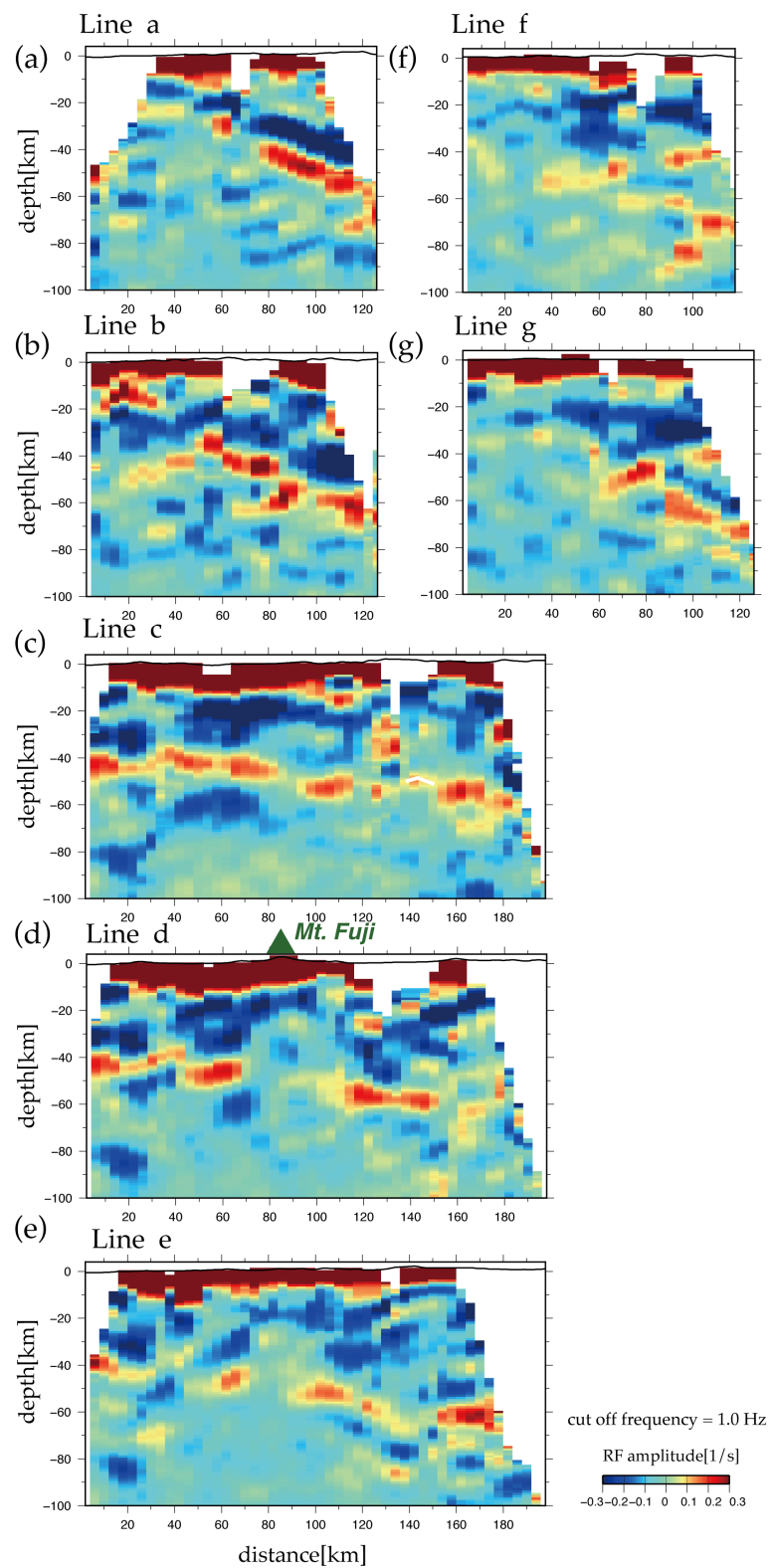
Figure 4.3
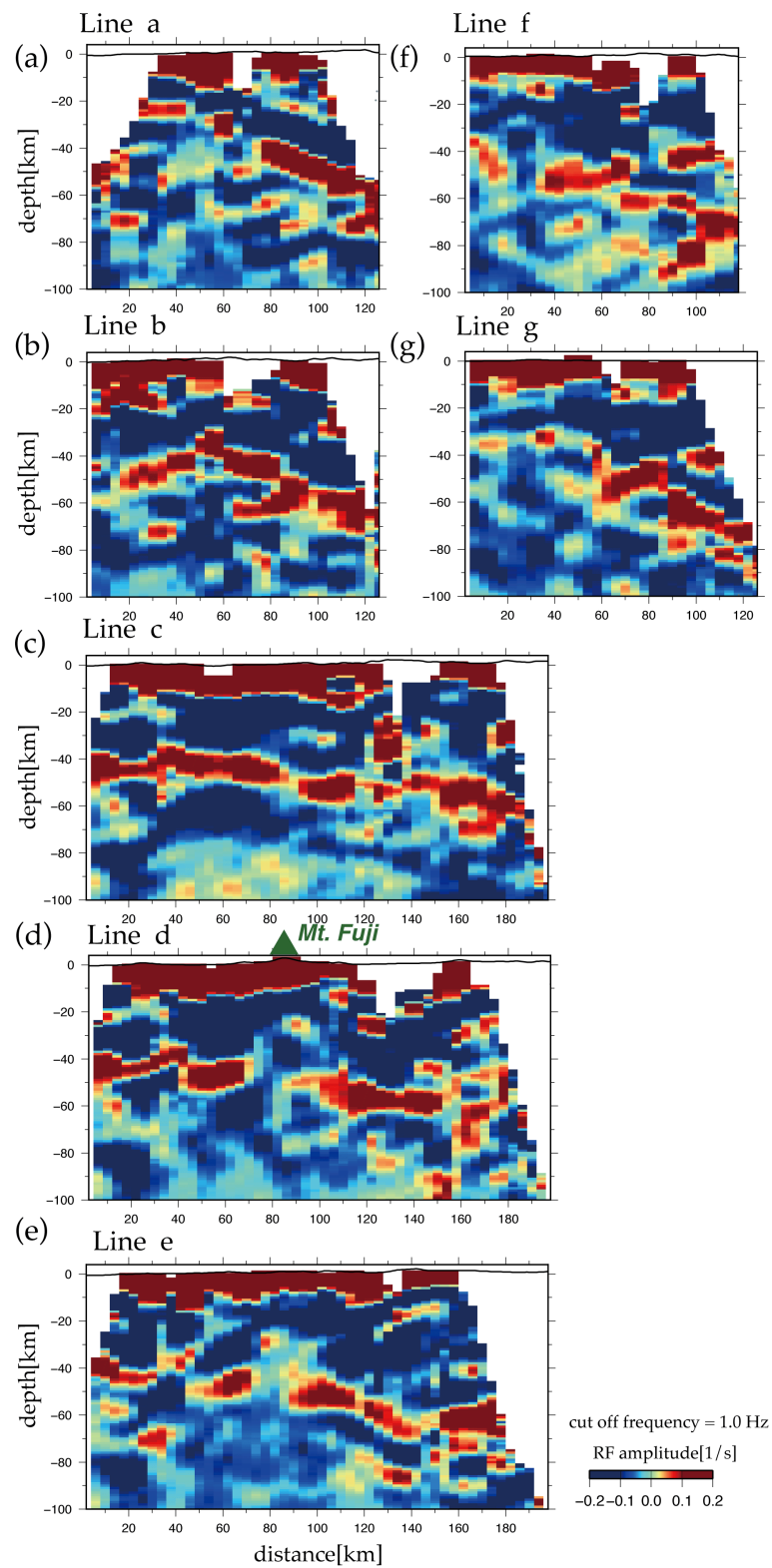
Figure 4.4
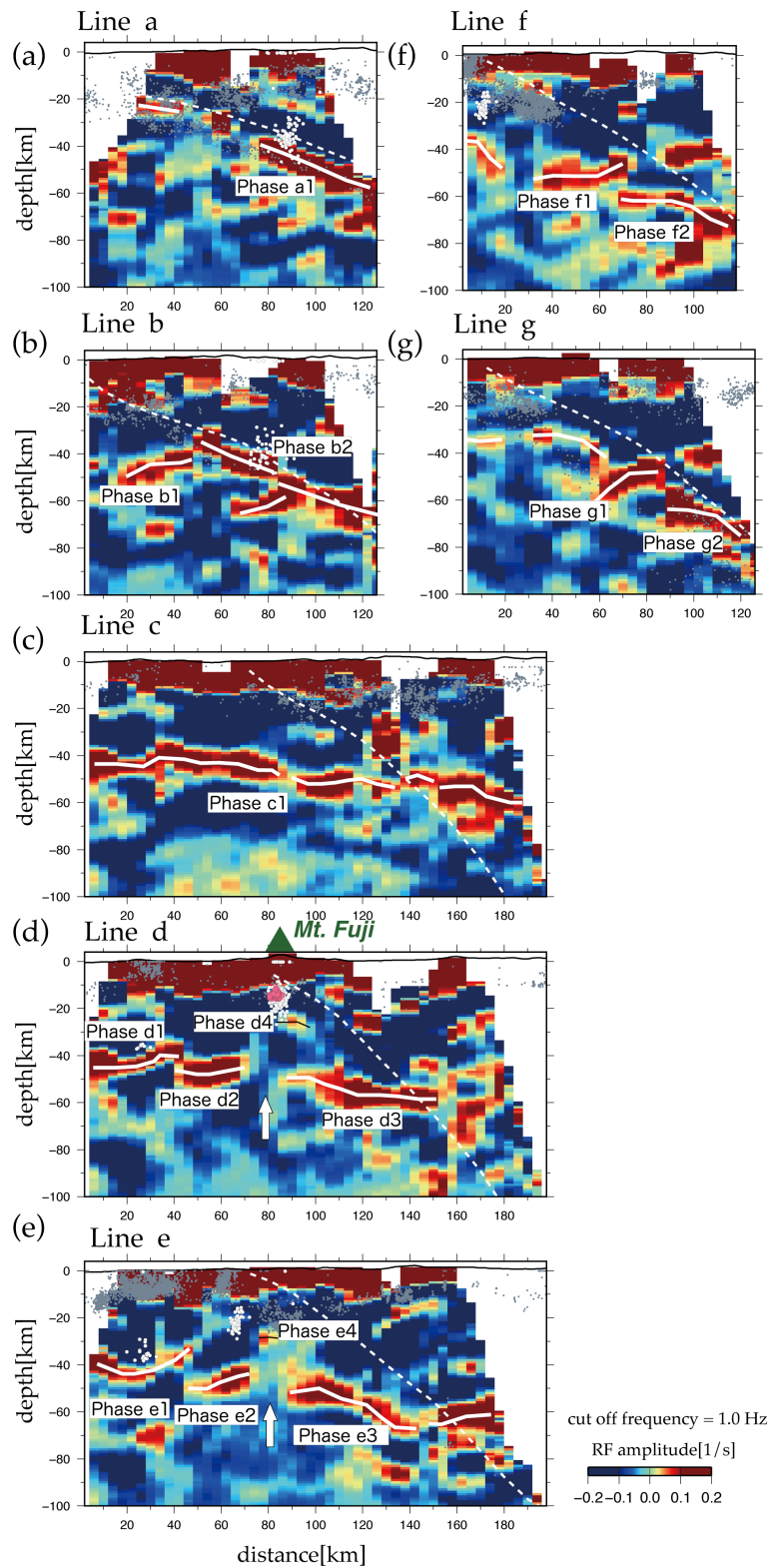
Figure 4.5

Figure 4.3: An example of cross sections of the RF amplitude along the subduction direction of IBM.
Each panel represents the cross section of the radial RF amplitude with a cutoff frequency of 1.0 Hz along seven red lines in Figure 4.2. The color scale of the amplitude is shown at the bottom.

Figure 4.4: An example of cross sections of the RF amplitude along the subduction direction of IBM.
Same as Figure 4.3 but for the different color scale.

Figure 4.5: An interpretation of the velocity boundaries found in the RF image along the subduction direction of IBM.
Same as Figure 4.4 but with the remarkable phases. Gray dots and white circles in each panel are the hypocenters with magnitude 0.1 or larger occurring between 2002 and 2006, taken from the JMA hypocenter catalogue. White circles represent low-frequency earthquakes (LFEs). Pink circles show relocated hypocenters of LFE below Mount Fuji (*Nakamichi et al.*, 2007). The green triangle in line d represents the summit of Mount Fuji projected onto the cross section. White dashed lines indicate the upper surface of the PHS plate (*Nakajima et al.*, 2009). White solid lines are inferred positive velocity boundaries from this study. Black solid line in Line d is the inferred positive velocity boundary below the region where LFEs of Mt. Fuji occur. White arrows indicate the gap in the velocity boundary described in the text. The remarkable positive phases named in each panel are explained in the text.
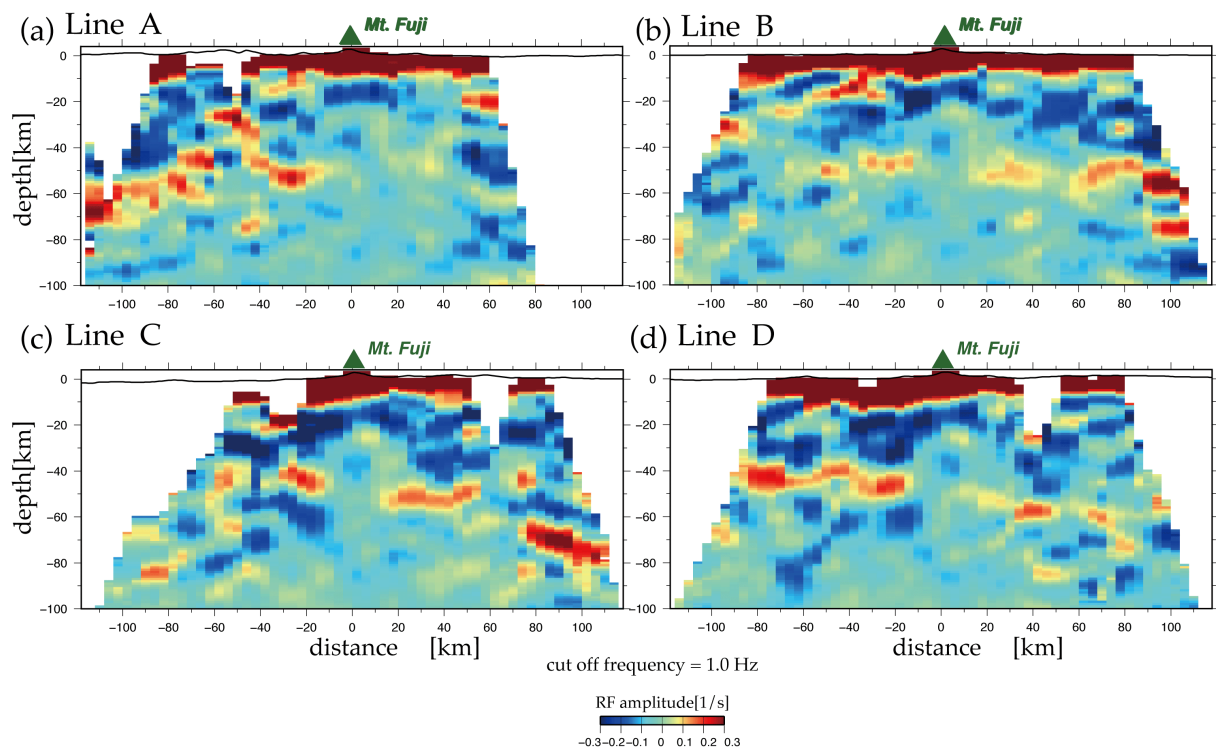
Figure 4.6: An Example of cross sections of the RF amplitude around Mt. Fuji.
Each panel represents the cross section of the radial RF amplitude with a cutoff frequency of 1.0 Hz around Mt. Fuji along four blue lines shown in Figure 4.2.
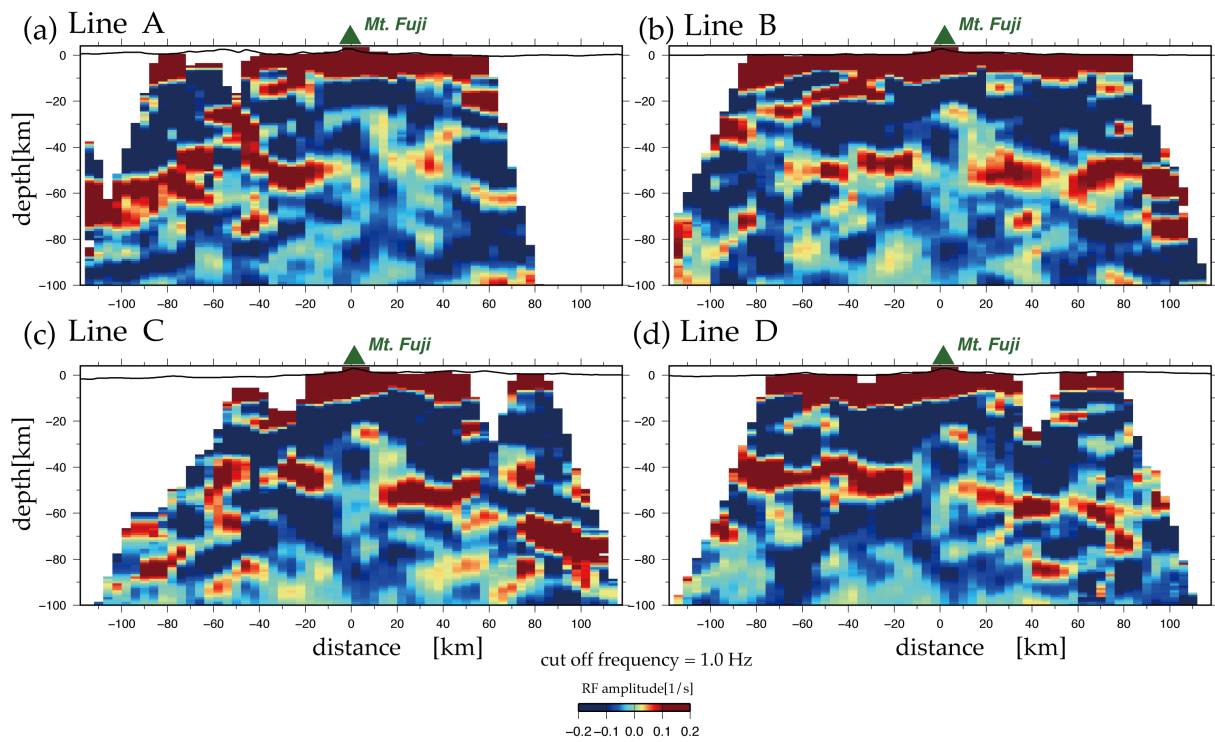
Figure 4.7: An Example of cross sections of the RF amplitude around Mt. Fuji. Same as Figure 4.6 but for the different color scale.
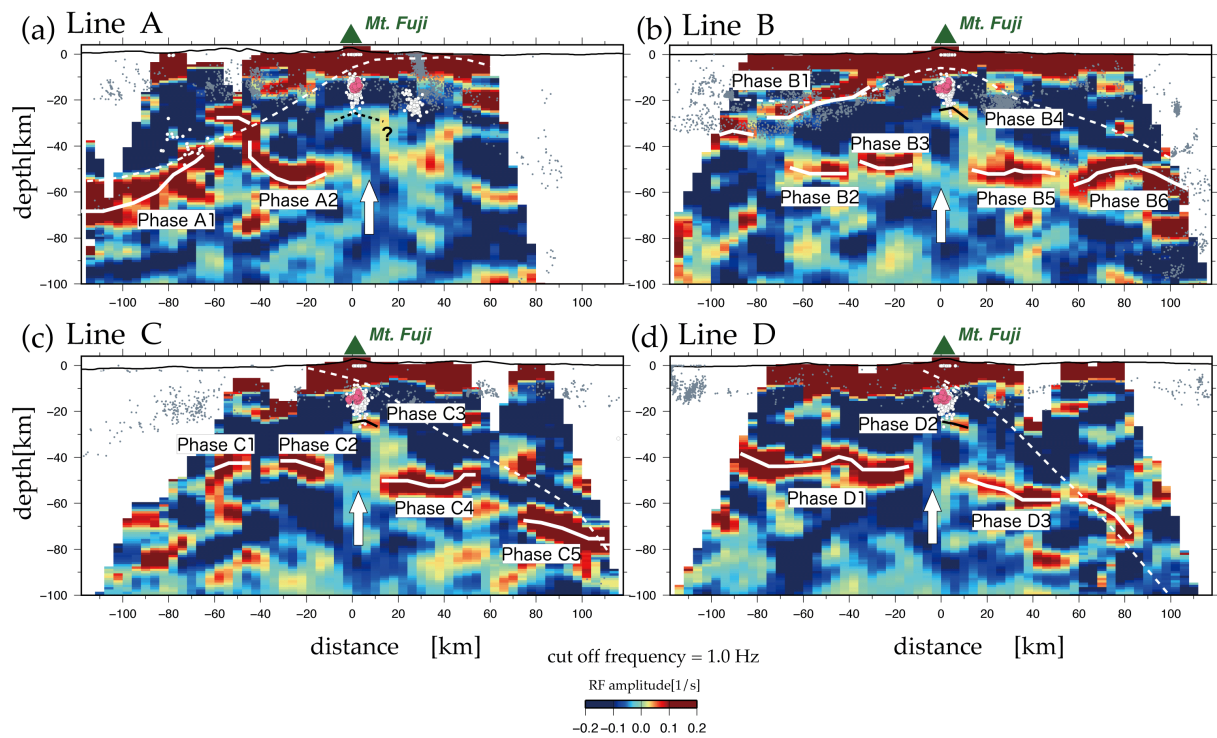
Figure 4.8: An interpretation of the velocity boundaries around Mt. Fuji.
Same as Figure 4.7 but with the remarkable phases. Parameters are the same as those in Figure
4.5. The black dot line in (a) represents the positive boundary below the region where LFEs of Mt.
Fuji occur whose amplitudes are smaller than that in (b)-(d) indicated by black solid lines.

4.3   Uncertainties of amplitude of radial RFs

4.3.1   The depth of velocity interfaces

We checked the influence of velocity structures on the time-to-depth conversions by trying standard velocity models by four previous studies. Figure 4.9 represents cross sections of radial RFs around Mt. Fuji along the Line c in Figure 4.8. From velocity models of (a) *Nakamichi et al.* (2007) (same structure in Figure 4.5 and 4.8), (b) the JMA one dimensional structure by *Ueno et al.* (2002), (c) *Nishida et al.* (2008) and (d) *Matsubara and Obara* (2011). The depths of velocity interfaces detected in RF cross sections are common in all panels in Figure 4.9, in that there are distinct positive phases between depths of 40 and 60 km and local positive phases at about a depth of 20 km below Mt. Fuji.

Line D

(a) Nakamichi et al. [2007] + JMA

(b) JMA

(c) Nishida et al. [2008]

(d) Matsubara and Obara, [2011]

RF amplitude[1/s]

distance [km]   cut off frequency = 1.0 Hz   distance [km]
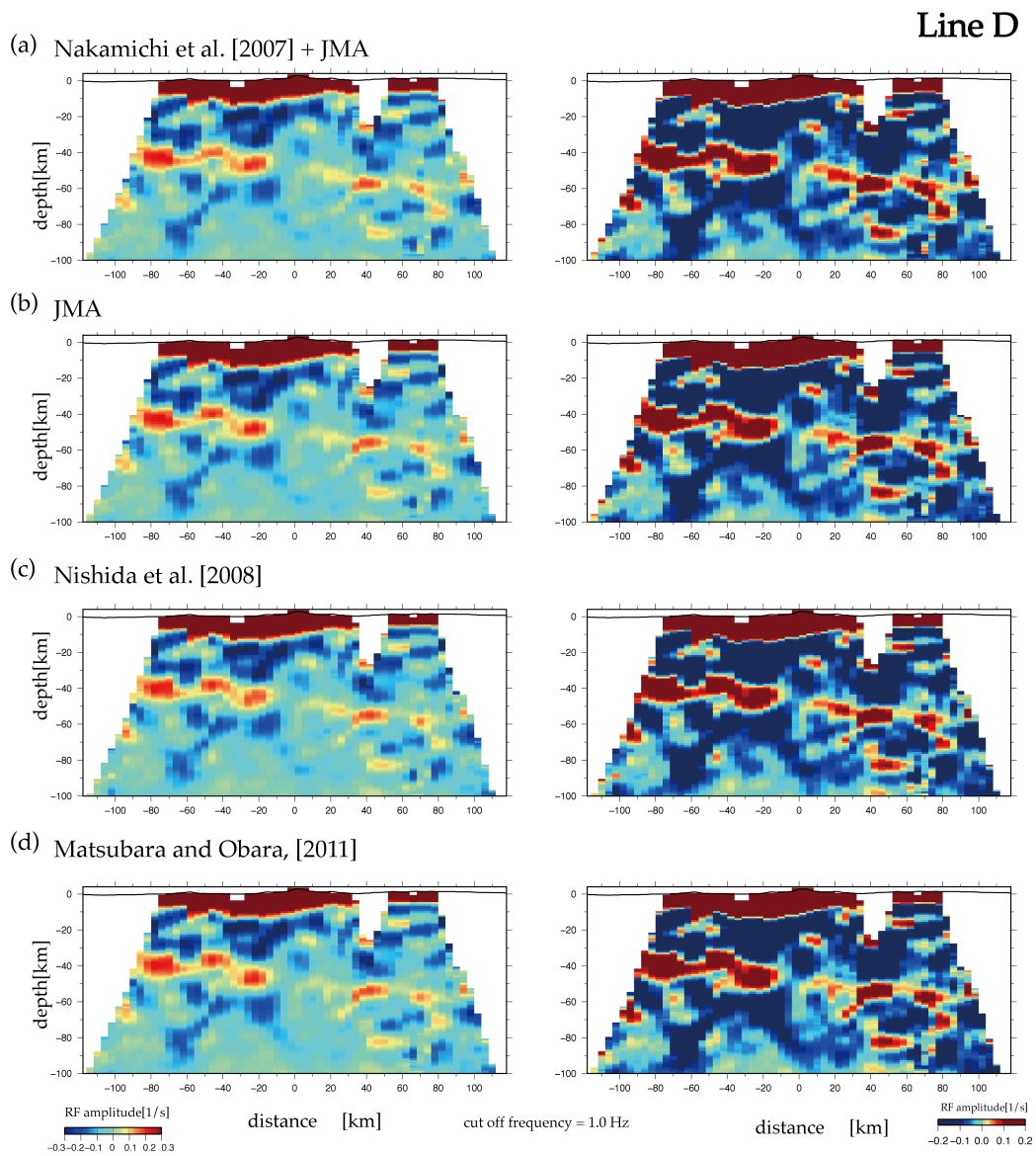
RF amplitude[1/s]

Figure 4.9: Comparison of RF cross sections with different velocity models.
Each panel represents the cross section of radial RF amplitudes along the Line D in Figure 4.2 with a cutoff frequency of 1.0 Hz around Mt. Fuji. The left and right panels use different color scales shown at the bottom. (a) A combination of *Nakamichi et al.* (2007) and the JMA structure (*Ueno et al.*, 2002), (b) JMA structure (*Ueno et al.*, 2002), (c) *Nishida et al.* (2008) and (d) *Matsubara and Obara* (2011).

4.3.2   Dipping velocity interfaces

The depths of velocity interfaces represented by black and white solid lines in Figures 4.5 and 4.8 have errors in time-to-depth conversions of RFs caused by the assumption of a flat layered structure. Dipping structures such as velocity interfaces in the subducting slab may cause errors in the depth estimation from radial RFs because the arrival times of Ps conversion at velocity interfaces vary by different back azimuths. *Shiomi et al.* (2004) calculate the lag time of the Ps phase from the velocity interface with various dip angles and conversion depths using the JMA velocity structure (*Ueno et al.*, 2002) to evaluate the error of the depth conversion in dipping velocity structures. Their results show that the errors of the depth conversion with a dipping angle of 20 degree are about 3, 4 and 5 km from the boundary at the depth of 30, 40 and 50 km. The dipping angle of the velocity contrast below Mt. Fuji in Fig 4.8 is less than 20 degree, so that errors originated from the dipping interface can be less than 5 km.

4.3.3   Anisotropy

As discussed in Chapter 4.1, 2-lobed and 4-lobed polarity patterns of the phase in transverse RFs suggest a possibility of the existence of an anisotropic media below the seismic station. Anisotropic layers also change arrival times of the Ps conversion in radial RFs. *Wirth and Long* (2012) executed forward modeling calculations of RFs including dipping layers and anisotropy between 3-8 percent in the mantle wedge and oceanic crust to reconstruct RFs in the subduction zone around northeast Japan. Although their analysis focused on the subducting Pacific slab and our study focused on the subducting PHS slab, we believe the influence on radial RFs by anisotropic conditions in subducting plate is similar to that in our study area. They show that the arrival times of Ps converted phases in radial RFs are mostly constant regardless of back azimuths. The difference of arrival times between the back azimuths is within 0.5 second, so the error of depth conversion caused by the anisotropic layer is within 5 km in that study.

4.3.4   Multiple phases

Cross sections of RFs' amplitude are contaminated by multiply converted phases (e.g., PpPs, PsPs) at shallow velocity discontinuities. Arrival times of these multiple phases can be calculated assuming a flat-layered velocity structure (equation 2.7 and 2.8). We can separate Ps and PpPs arrivals because the arrival time of the Ps phase increases with increasing ray parameter, whereas that for PpPs decreases with increasing ray parameter (*Salmon et al.*, 2011). Figure 4.10a-c shows an example of RFs stacked according to ray parameters for all the rays that intersect regions 1, 2 and 3 in Figure 4.8a, with bin widths of 0.006 s/km and a spacing as 0.003s/km. Predicted arrival times of Ps phases (solid gray lines in Figure 4.10) are also calculated with the velocity structure used in time-to-depth conversions of RFs. Figure 4.10a shows that the arrival times of focusing positive phases are found at a depth of 30 km. This corresponds to that of the Ps phase from about 30 km depth, increasing with increasing ray parameter shown in Fig 4.10a. Similarly, stacked RFs in Figures 4.8b-c show that delay times of focusing phases increase with increasing ray parameters, supporting the idea that these phases are not multiples from shallow velocity boundaries.
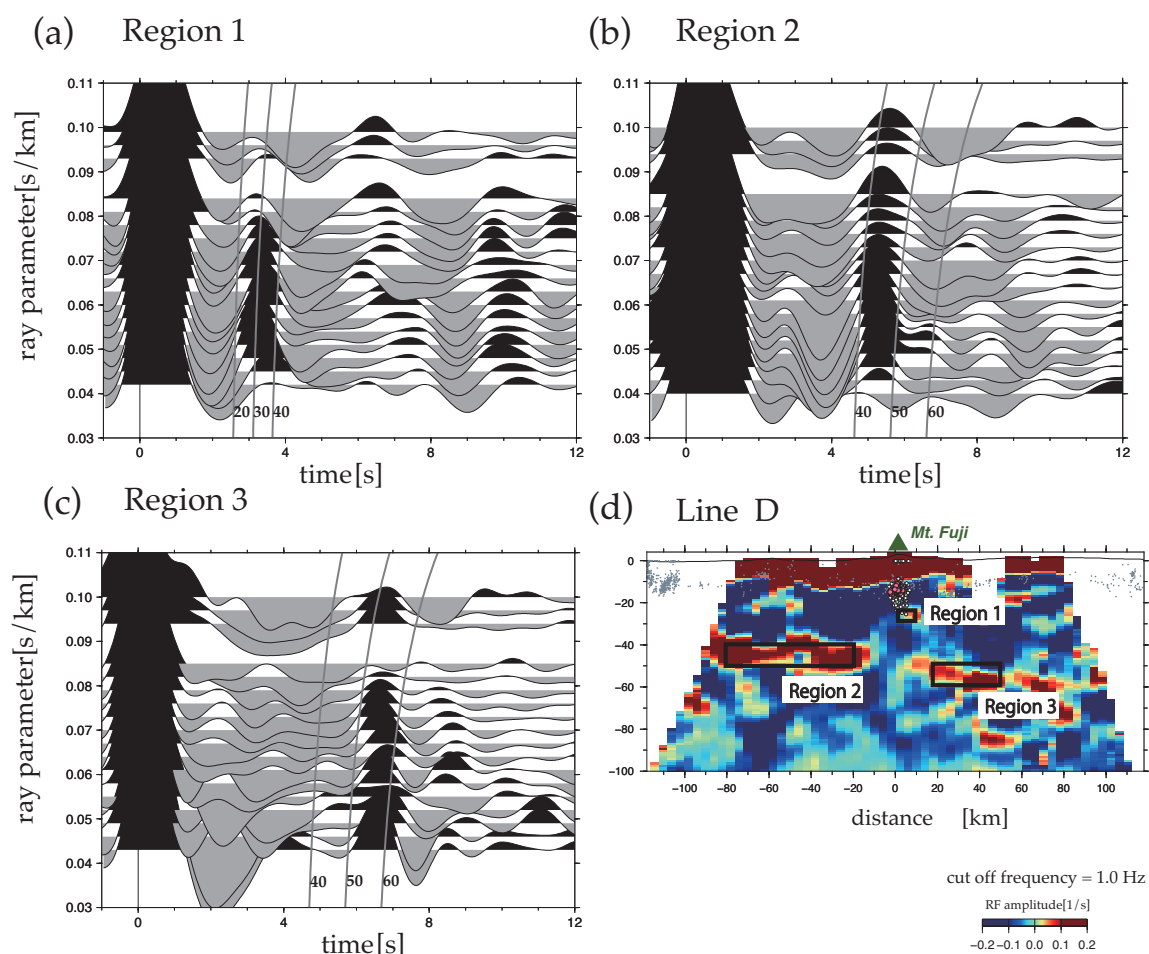
Figure 4.10: Stacked RFs according to ray parameters.
Stacked RFs according to ray parameters whose raypaths intersect (a) region 1, (b) region 2 and (c) region 3 indicated by black solid lines in (d). Gray solid lines represent the arrival time of Ps converted waves at the depths of 20, 25, 30 km in (a), 40, 50, 60 km in (a)-(c), respectively, calculated from the velocity structure by *Nakamichi et al.* (2007).

4.3.5   Resolutions of velocity interfaces

Vertical resolutions of Ps converted phases correspond to a half wavelength of the incoming P wave (*Bostock*, 1999; *Rychert et al.*, 2007). On the other hand, horizontal resolutions are generally taken as the radius of the first Fresnel zone of incoming P wave (e.g., *Darbyshire et al.*, 2000; *Abe*

et al., 2010) by

$$R = \sqrt{\left(z + \frac{\lambda}{2}\right)^2 - z^2} \tag{4.1}$$

where λ and z represent the wavelength of incoming P wave and the depth of the velocity interface, respectively. In our analysis, RFs are low-pass filtered using the cosine squared filter with the cut off frequency of 1.0 Hz, so the dominant frequencies are less than about 0.33 Hz (e.g., *Igarashi et al.*, 2011). The averaged P and S wave velocities below Mt. Fuji used in the calculation of RF cross sections are about 6 and 3–3.5 km/s at depths of 20–25 km, so that the vertical and the horizontal resolutions are about 9 and 20 km, respectively. Similarly, P and S wave velocities are about 7.8 and 4.4 km/s at a depth of 50 km, so that the vertical and horizontal resolutions are about 12 and 35 km, respectively.

5 Inverting of Receiver Functions for S-wave velocities

5.1 Background

Kinoshita et al. (2015) concluded that two conditions are required to satisfy a positive phase near zero time lag towards positive time followed by a negative phase in radial RFs observed at stations near Mt. Fuji: a near-surface low-velocity sediment layer and a low velocity region at about 20 km depth beneath Mt. Fuji. These features change positive amplitudes in radial RFs of Ps converted phases from high velocity interfaces because a low velocity layer and multiple sediments phases generate negative phases.

Figure 5.1 shows the influences of a low velocity layer and a surface sediment layer on the radial RF amplitudes from the velocity boundaries. The amplitudes of RFs are normalized by those corresponding the direct P wave. With a four-layer velocity structure in which the velocity gets higher in a lower layer (Figure 5.1a), positive velocity boundaries at depths of 20 and 40 km make the positive phases at about 2.5 and 5 seconds. An addition of sedimentary surface layers with low velocity from the first model (Figure 5.1a) generates a distinct negative phase at about 2.5 second and a change in the amplitude of Ps converted phase from the interfaces at 20 and 40 km (Figure 5.1b). Furthermore, multiple sediments phases shift the direct P pulse from zero time lag and broad the pulse width as described in Chapter 4 (*Cassidy*, 1992).

An addition of a low velocity layer at a depth between 10 and 15 km from the first model (Figure 5.1a) generates a negative phase at about 1 and 4 seconds originated from a negative velocity boundary at 10 km (Figure 5.1c). RFs could not separate the velocity interfaces of 15 and 20 km in this frequency. The positive phase from a depth of 40 km is distorted from that in Figure 5.1a as is the case with Figure 5.1b.

As explained above, we could not evaluate a magnitude of velocity contrasts only from cross sections of radial RF amplitudes in volcanic regions where both thick volcanic sediment layer and low velocity layers are expected to exist. Inverting RF waveforms including low velocity layers

and sediment layers can extract more information about the velocity structure below the station than only evaluating RF amplitudes. Amplitudes of radial RFs are sensitive to the S wave velocity around velocity boundaries, so that inverting radial RFs for seismic velocities is effective to verify the velocity boundaries found in RF cross sections.
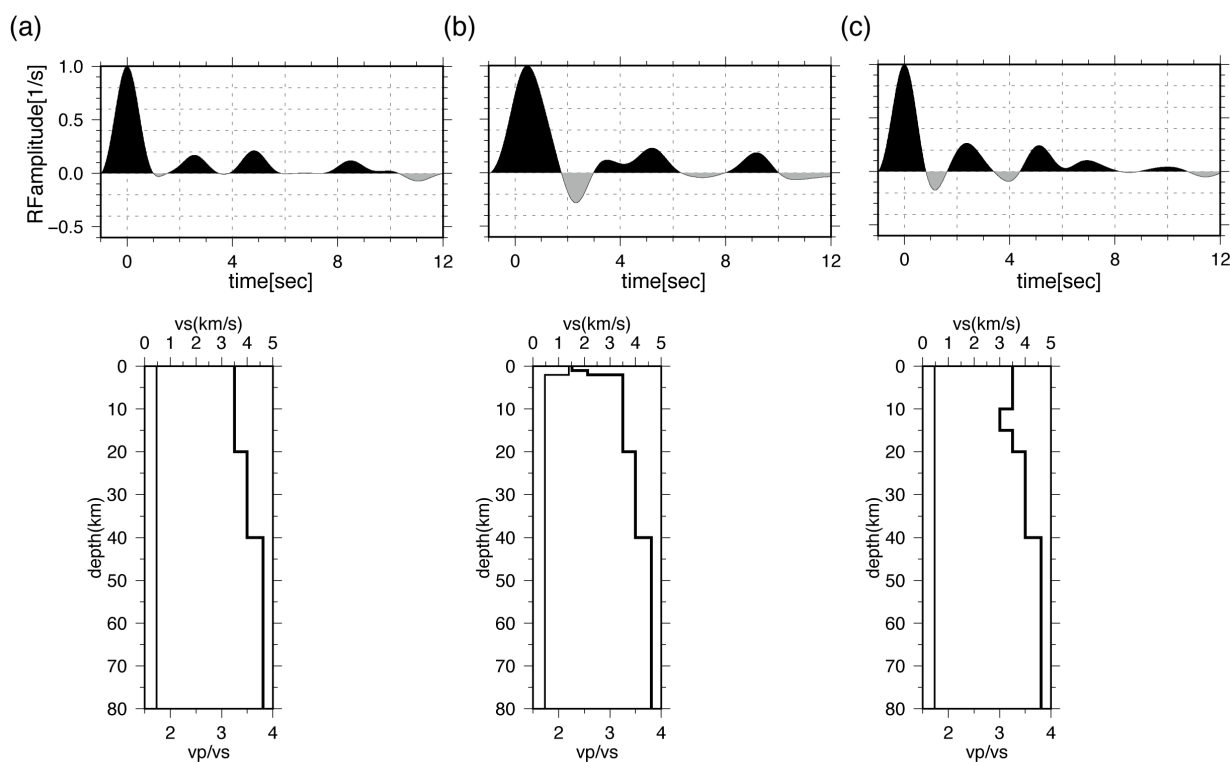
Figure 5.1: Comparison of the RF amplitude in three velocity models. Synthetic RFs estimated from three different velocity models: (a) a simple three-layered structure, (b) a simple three-layered structure with low velocity sedimentary layers, and (c) a simple three-layered structure with a low velocity layer at 10-15 km. RF amplitudes are normalized to those of the direct phase.

Inversions of RFs solve nonlinear equations between velocity structures and RFs. The inversion methods are classified into two categories: one is the linearized inversion method and the other is the Monte Carlo inversion method.

Ammon et al. (1990) proposed a technique to estimate layered and isotropic velocity structures from RFs by solving iteratively the linearized equation. This method has three problems. First, the

best solution is searched iteratively by changing model parameters from the initial model, so the obtained model parameters depend strongly on the initial model. Second, the smoothing parameters to solve the inversion stably result in blurring the contrast of sharp velocity boundaries. And finally, there is a trade off between the depth of velocity interfaces and the average velocity over interfaces, so the absolute S wave velocities are unconstrained in principle. The third problem, in fact, is not due to a linearization of equations but an inherent problem of the inversion of RFs for the velocity structure.

Joint inversions of RFs and surface wave dispersion can adress the third problem (*Julia et al.*, 2000). While RFs are sensitive to the velocity contrasts of S wave, not to the absolute velocity value of that, as described in Chapter 2 (e.g., *Julia*, 2007), wave dispersions have sensitivity to averaged S wave velocities below the seismograph stations. *Julia et al.* (2000) formulated linearized equations to jointly solve RFs and dispersion curves by better constraining the absolute velocities. However, *Julia et al.* (2000) did not solve the first and the second problem shown above because of the linearized equations. In our case, it is difficult to assign an appropriate initial model that is not far from the true velocity model, so it is not adequate to execute the linearized inversion.

The Monte Carlo Inversion method is generally used in the geophysical problems which solve the nonlinear problems such as the estimation of seismic velocity models. This method samples a parameter space directly and needs not to constrain by damping, nor solve a complex matrix like the linearized inversion method described above (*Sambridge and Mosegaard*, 2002). *Shibutani et al.* (1996) adopted the Generic Algorithm (GA) to the RF inversion to estimate the S wave velocities without linearization. GA is one of the Monte Carlo methods that generate succeeding populations through selections, crossovers and mutations. They calculated a weighted average model using 1,000 acceptable models whose residuals are small in 10,000 generated models. Note that the solution does not depend on initial models. RF inversions using the Monte Carlo method are very effective in detecting a distinct low velocity region that is indefinite from previous studies. For example, *Abe et al.* (2010) executed a RF inversion using GA around Mt. Aso, a large active

volcano with caldera in southern Japan, and found a low velocity zone with S wave velocity of 2.0–2.4 [km/s] at depths between 15 and 20 km.

Other branches of the Monte Carlo methods include Neighbourhood algorithm (*Sambridge*, 1999a,b), Simulated Annealing algorithm (e.g., *Vinnik et al.*, 2004), all of which have successfully been applied for the RF inversions. Also, simple grid search approaches are performed by supposing four or five isotropic flat layers (e.g., *Lodge and Helffrich*, 2009; *Igarashi et al.*, 2011; *Kinoshita et al.*, 2015). The grid search, in theory, successfully finds an optimum set of model parameters but is often computationally too expensive. In this study, we adopt Simulated Annealing method (SA) to invert the absolute S wave velocity model around Mt. Fuji because this method can search the optimum solution efficiently.

5.2   Simulated Annealing methods

SA is one of the Monte Carlo methods that solve an optimization problem by searching for a global minimum (or maximum) of an objective function $E(m)$, where m represents model parameters (e.g., *Sen and Stoffa*, 2013). This algorithm mimics a physical annealing process in computers where particles in liquid phase at higher temperature make a fine crystalized structure with lower energy in solid phase through decreasing temperature very slowly. Figure 5.2 shows the flowchart of SA after *Beaty et al.* (2002).
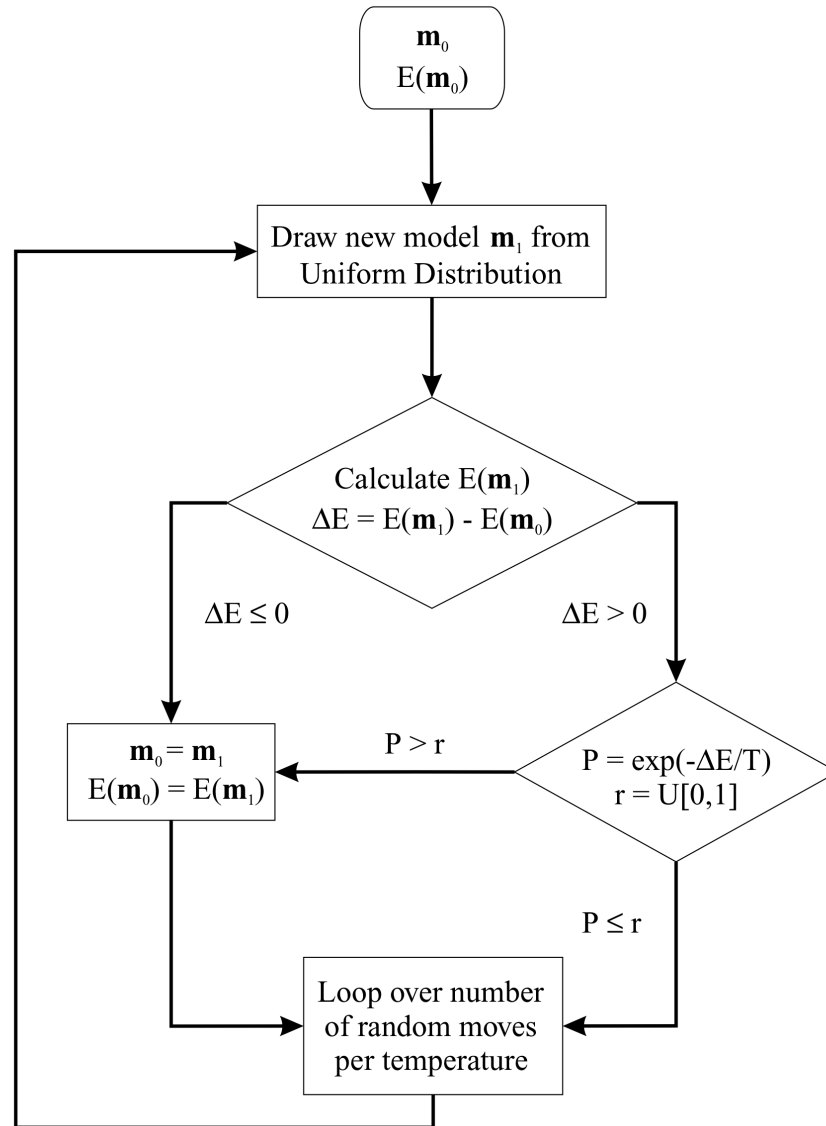
Figure 5.2: Flowchart of the SA method after *Beaty et al.* (2002).

m_0 and $E(m)$ represent initial model parameters and the objective function, respectively. If the objective function $E(m_1)$ is smaller than $E(m_0)$, the new model is accepted. If $E(m_1)$ is larger than $E(m_0)$, a random number between 0 and 1 is calculated and the new model is judged if the random number is smaller than the probability P (*Metropolis et al.*, 1953).

There are three general steps in SA: generation, acceptance and reduction. In the generation step, one of the model parameters is updated by random sampling within the prescribed range for each model parameter. In the acceptance step, the new model generated in the previous step is judged to be acceptable or not. If the objective function $E(m)$ is less than that of the previous model, the new model parameter is accepted. Otherwise, the new model parameter will be accepted by the probability P_{accept} according to Metropolis rule (*Metropolis et al.*, 1953):

$$P_{accept} = \exp\left[-\frac{\Delta E}{T}\right] \tag{5.1}$$

where ΔE and T are the difference in the objective function between the previous and generated model, and temperature, respectively. In Metropolis rule, we calculated a random number between 0 and 1, and judge whether the random number is greater or smaller than P_{accept}. The new model is accepted if a random number is smaller than P_{accept}, and that is rejected if the random number is greater than P_{accept}. P_{accept} become 1 with high temperature, resulting that almost all models are accepted. On the other hand, P_{accept} become almost 0 with low temperature, resulting that the new model parameter will be almost rejected if ΔE is greater than 0. These generation and acceptance steps are repeated sufficiently. In the reduction step, the temperature in equation (5.1) is updated according to a time schedule. A theoretical consideration requires a logarithmic schedule

$$T(n) = \frac{T_0}{\ln n} \tag{5.2}$$

to converge to the global minimum for SA (e.g., *Sen and Stoffa*, 2013). Parameters n and T_0 represent the iteration number and the starting temperature, respectively. However, this time schedule requires too much computational power to converge within a realistic time. With this, we use a practical time schedule as

$$T(n) = rt \cdot T(n-1) \tag{5.3}$$

where rt represents a constant parameter for reducing the temperature. This algorithm has the

advantages that large numbers of variables can be employed without any constraint on the objective function E(m) and can easily add complicated conditions for constraining model parameters. However, to get global minimum, an extensive computation is required. Also it is difficult to gain insights into uncertainties of the inferred optimum model parameters because SA gives one optimum solution without any information on uncertainties.

5.3   Synthetic tests

Igarashi et al. (2011) successfully calculated the crustal and upper mantle structure using a simple four-layered structure, in which the velocity of a deeper layer is always higher than a shallower layer, by a grid search method searching for broad velocity ranges. We use a similar parameterization to that employed in their study. A five-layered structure is used in our study area because previous studies have suggested an existence of a low velocity region (*Nakamichi et al.*, 2007; *Kinoshita et al.*, 2015). We calculated a four-layered structure that the velocity in a deeper layer should be always higher than a shallower layer as is the case with *Igarashi et al.* (2011) for comparison.

Nine model parameters v1, v2, v3, v4, v5, Da, Db, Dc, and Dd in the five-layered structure, and seven parameters v1, v2, v3, v4, Da, Db, and Dc in the four-layered structure are assumed. Parameters Da-Dd represent the depth in kilometers of the bottom boundary of each layer. Parameters v1 and v2-v5 represent the S wave velocity km/s at the top of Layer 1 and in Layers 2-5, respectively. In Layer 1, the velocity increases from v1 km/s to v2 km/s gradually.

Based on the results of the traveltime tomography by *Nakamichi et al.* (2007), we set the Vp/Vs ratio to 2.2 in Layer 1 and 1.73 in other layers. Possible parameter ranges which we believed broad enough are listed in Table 5.1 and shown in Figure 5.3. Although *Nakamichi et al.* (2007) shows that the Vp/Vs ratio in a low velocity region below Mt. Fuji is more than 2.0, difference of the Vp/Vs ratio is not essential in this study because amplitudes of RFs are sensitive to S wave contrast as discussed in Chapter 2 (*Julia*, 2007). The density ρ is estimated from Ludwig's law (*Ludwig*

et al., 1970) as follows.

$$\rho = 1.2475 + 0.3992 * V_p - 0.026 * V_p^2 \quad (V_p < 6.6) \tag{5.4}$$

$$\rho = 0.3788 * V_p + 0.252 \quad (V_p > 6.6) \tag{5.5}$$

We also constrain the average P wave velocity above 60 km to be less than 7.0 (km/s) to avoid a situation in which all boundaries are located shallow depths and all the observed phases are created only by the reverberations at shallow depths. Furthermore, the width of each layer is set to be more than 5 km.

		bottom depth [km]			Vs [km/s]			Vp/Vs
	Layer	name	lower	upper	name	lower	upper	
	Layer 1	Da	1	9	v1	0.5	2.7	2.2
	Layer 2	Db	2	30	v2	2.5	4	1.73
5−layered model	Layer 3	Dc	3	40	v3	1.5	4.1	1.73
	Layer 4	Dd	4	60	v4	2.5	4.2	1.73
	Layer 5				v5	4.3	4.8	1.73
	Layer 1	Da	1	9	v1	0.5	2.7	2.2
	Layer 2	Db	2	40	v2	2	4	1.73
4−layered model	Layer 3	Dc	3	60	v3	2.5	4.3	1.73
	Layer 4				v4	4.3	4.8	1.73

Table 5.1: Parameter ranges used in SA inversions.
Names, lower bounds and upper bounds of model parameters are listed. Vp/Vs values are fixed and P wave velocities are calculated using the Vp/Vs ratio in each layer.

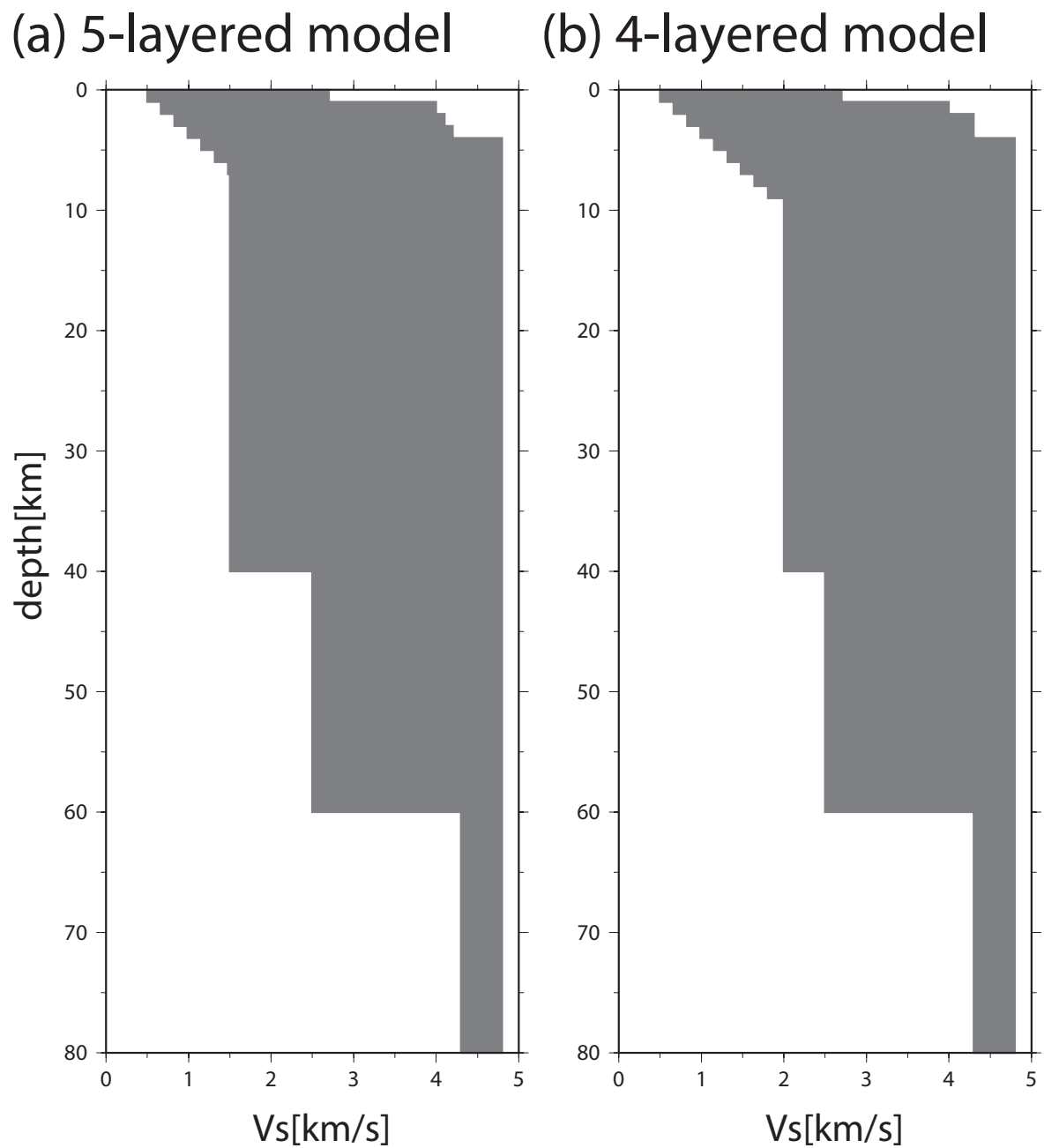# (a) 5-layered model (b) 4-layered model

Figure 5.3: Ranges of S wave velocities used in SA inversions.
Ranges of S wave velocities with (a) a 5-layered structure and (b) a 4-layered structure. In a 4-layered structure, the velocity in a lower layer should be always higher than a higher layer. Possible parameter ranges are listed in Table 5.1

As discussed above, a joint inversion of RFs with dispersion curves of surface waves can improve the trade-off between the depth of the velocity boundary and the average velocity over the boundary (*Julia et al.*, 2000). In this study, we use the dispersion derived by *Nishida et al.* (2008) from an ambient noise tomography using Hi-net tilt-meters operated by NIED. We calculate dispersion curves of both the Rayleigh and the Love wave in the fundamental mode below each station using their S wave model that is inverted from phase velocities of surface waves. Because the distribution of seismic sites is sparser around Mt. Fuji in *Nishida et al.* (2008) than our study, local strong velocity anomalies around Mt. Fuji may not be imaged in their model. The dispersion curves of the Love and the Rayleigh wave have different sensitivities in depths, so inversions with both dispersion data can constrain the velocities in different depths. The objective function to be minimized, E, is defined as follows:

$$E = (1 - c)E_{rf} + \frac{c}{2}\left[E_{dispLOVE} + E_{dispRAY}\right] \tag{5.6}$$

where E_{rf} and E_{disp} represent the least squares errors of RFs and dispersion curves, respectively, as defined below. The subscripts $LOVE$ and RAY denote the Love and the Rayleigh waves, respectively. c is a constant parameter that defines the weight of individual errors. Each least squares error is calculated from following equations:

$$E_{rf} = \frac{\sum_{i=1}^{N_{rf}}[RF_{obs}(i) - RF_{pre}(i)]^2}{\sum_{i=1}^{N_{rf}}[RF_{obs}(i)]^2} \tag{5.7}$$

$$E_{disp} = \frac{\sum_{i=1}^{N_{disp}}[DISP_{Nishida}(i) - DISP_{pre}(i)]^2}{\sum_{i=1}^{N_{disp}}[DISP_{Nishida}(i) - DISP_{reference}(i)]^2} \tag{5.8}$$

where N_{rf} and N_{disp} are the numbers of data in RFs and dispersion curves, RF_{obs} and RF_{pre} represent observed and calculated RFs, respectively. $DISP_{Nishida}$ and $DISP_{pre}$ represent the dispersion curves based on *Nishida et al.* (2008) and calculated velocity models, respectively. E_{rf} is normalized by the power of observed RFs, whereas E_{disp} is normalized by the power of the difference of

the dispersion curves between *Nishida et al.* (2008) and reference velocity models, which are based on the structure of *Nakamichi et al.* (2007) and the JMA structure (*Ueno et al.*, 2002). Synthetic seismograms from a given isotropic and layered velocity model are calculated using the propagator matrix method (*Kennett and Kerry*, 1979). The synthetic RFs are filtered by cosine-squared filter with a cutoff frequency of 1.0 Hz. The horizontal slowness is set to 0.07 s/km. The range of RF time window used in the inversion is between -1 and 10 seconds because we focused only on the structure shallower than 60 km below Mt. Fuji. The sampling rate is set to be 0.1 second and N_{rf} in equation (5.7) is 111. Although *Nishida et al.* (2008) obtained dispersion curves between 0.05 and 0.20 Hz, we use dispersion curves only between 0.05 and 0.15 Hz because the surface low velocity sediment layer around Mt. Fuji is not detected by *Nishida et al.* (2008) because of the sparse distribution of seismograph stations around Mt. Fuji used in their study. Dispersion curves of the Rayleigh and Love wave are calculated using DISPER80 (*Saito*, 1988). The sampling rate is set to be 0.005 Hz and N_{disp} in equation (5.8) is 21. In this section, we first verify the utility of the method with a synthetic dataset before dealing with the real dataset.

5.3.1   Synthetic test 1: Four-layered structure without a low velocity layer

We first performed synthetic tests to understand the characteristics of the RF inversion with the SA method by calculating the synthetic RFs from simple layered structures. Figure 5.4 shows the result of synthetic calculation for a four-layered structure. Synthetic RFs and dispersion curves associated with the synthetic structure represented by a black solid line in Figure 5.4e are inverted with SA. The parameters in SA in this study are set as

$$T_0 = 10 \tag{5.9}$$

$$rt = 0.90 \tag{5.10}$$

$$c = 0.05 \tag{5.11}$$

$$ns = 40 \tag{5.12}$$

where T_0, rt, and c represent the initial temperature, the temperature reduction parameter, and the weight coefficient in equations (5.3) and (5.6). Parameter ns represents the number of calculations performed in generation and acceptance steps to each model parameter. Least squares errors are reduced as the number of iteration increases with decreasing temperature (Figure 5.4a-c). Random samplings of model parameters in a wide range (Figure 5.3a) produce velocity models far from the true model in the beginning. Velocity models generated by SA gradually approach to the true model with increasing iterations (Figure 5.4d). The inverted model (red solid lines in Figure 5.4e-g) is well reconstructed compared with the synthetic model of the S-wave velocities, RFs and dispersion curves (black solid lines in Figure 5.4e-g).

5.3.2 Synthetic test 2: five-layered structure with a low velocity layer

In the next step, we checked the SA inversion is useful in the region with a low velocity layer because previous studies have suggested an existence of a low velocity region (*Nakamichi et al.*, 2007; *Kinoshita et al.*, 2015). Figure 5.5 shows the result of synthetic calculation with assuming a five-layered structure with a low velocity layer. There is a negative phase at 2.5 second generated by a combination of multiple phases generated at surface sediment layers and the Ps phase at the top of the low velocity boundary at a depth of 20 km. Comparison between the synthetic and inverted models demonstrates that the inverted model is well reconstructed.

5.3.3 Synthetic test 3: five-layered structure with a low velocity layer inverted for four-layered structure

Because a five-layered velocity structure assumed in the SA inversion may be too simple to represent the realistic complicated structure around Mt. Fuji, we test the inversion using the same five-layered structure in test 2 with a four-layered structure model (Figure 5.6). The results shown in Figures 5.5 and 5.6 indicate that the final model does not reconstruct the synthetic structure completely because of the lack of the layer number we assumed. The inversion in this study preferentially fits the larger amplitude in RF because we do not use the time-domain weighting

function. The largest pulse in the synthetic RF in Figure 5.6f is the direct phase at about 0 second and the following negative phase generated by the multiple reverberation of sediment layers and the upper boundary of the low velocity layer, so the result in Figure 5.6 can reconstruct the direct and following negative phase completely. Although the final model does not contain the positive velocity boundary at the depth of 35 km, the large velocity contrast in this structure, the velocity boundary at 25 km depth, is almost reconstructed. This shows that a RF inversion using simpler structure than the realistic structure preferentially detects large velocity contrasts. In other words, this test shows a possibility of small other velocity interfaces that remain undetected in the inversion process.

5.3.4   Synthetic test 4: five-layered structure with a low velocity layer with the Vp/Vs ratio 2.2

Because a local earthquake tomography shows that the Vp/Vs ratio in a low velocity region below Mt. Fuji is more than 2.0 (*Nakamichi et al.*, 2007), the influence of the difference of Vp/Vs ratio is tested. Figure 5.7 represents the result of the SA inversion solving the five-layered structure with a low velocity layer whose Vp/Vs ratio is 2.2. We solve the inversion using a five-layered structure whose Vp/Vs ratio of the uppermost layer is 2.2 and that of other layers 1.73. The result shows that the inverted model (red solid lines in Figure 5.7e-g) is well reconstructed. The inverted depth of the bottom boundary of the low velocity layer and the average S-wave velocity in the low velocity layer are slightly offset by within 5 (km) in depth and 0.1 (km/s) in velocity from the synthetic model to match the arrival time of Ps phase.
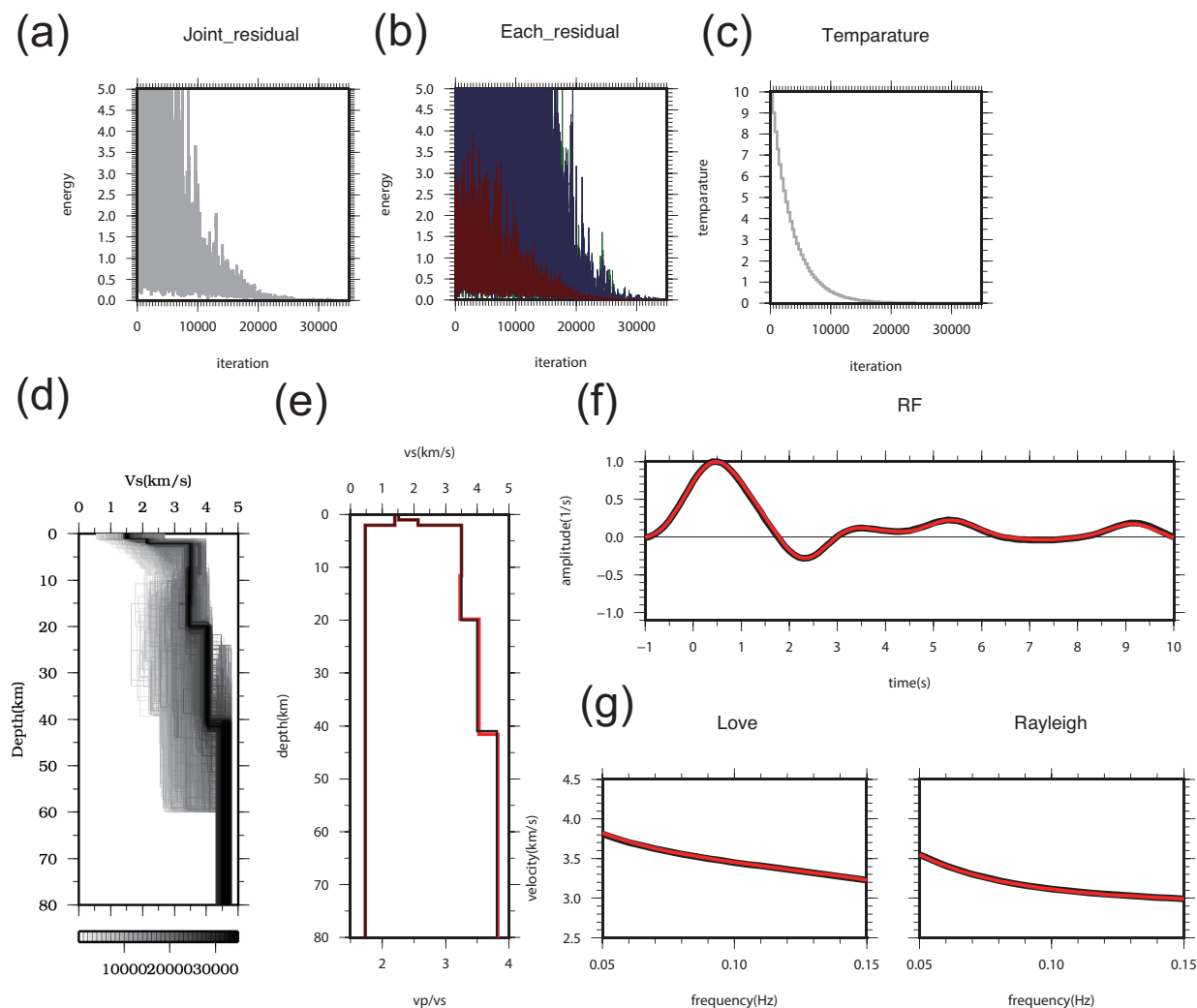
Figure 5.4: The result of synthetic test 1: four-layered structure without a low velocity layer. (a) Least squares errors defined in equation (5.6). (b) Individual least squares errors in equations (5.7) and (5.8). Red, green and blue colors represent the least squares of RFs, the dispersion curve of the Love wave and that of the Rayleigh wave. (c) Temperature schedule in this calculation. (d) All models generated in this calculation. The velocity models proceed from white to black plots. (e)-(g) Comparison between the synthetic (black) and inverted (red) models. (e) S wave velocity model and Vp/Vs value. (f) RFs. (g) Dispersion curve of the Love (left) and Rayleigh (right) waves.
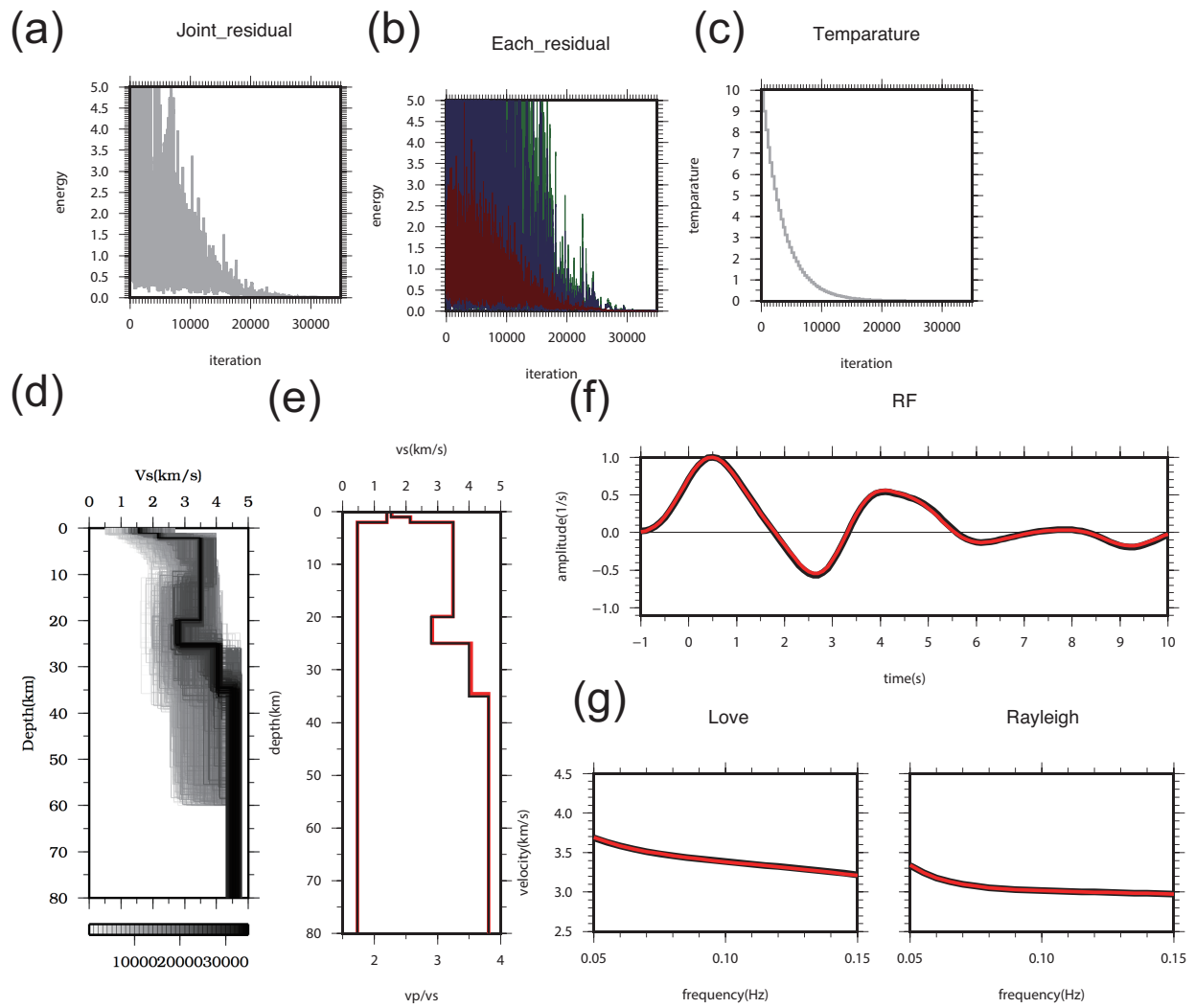
Figure 5.5: Same as Figure 5.4 but for the synthetic test 2.
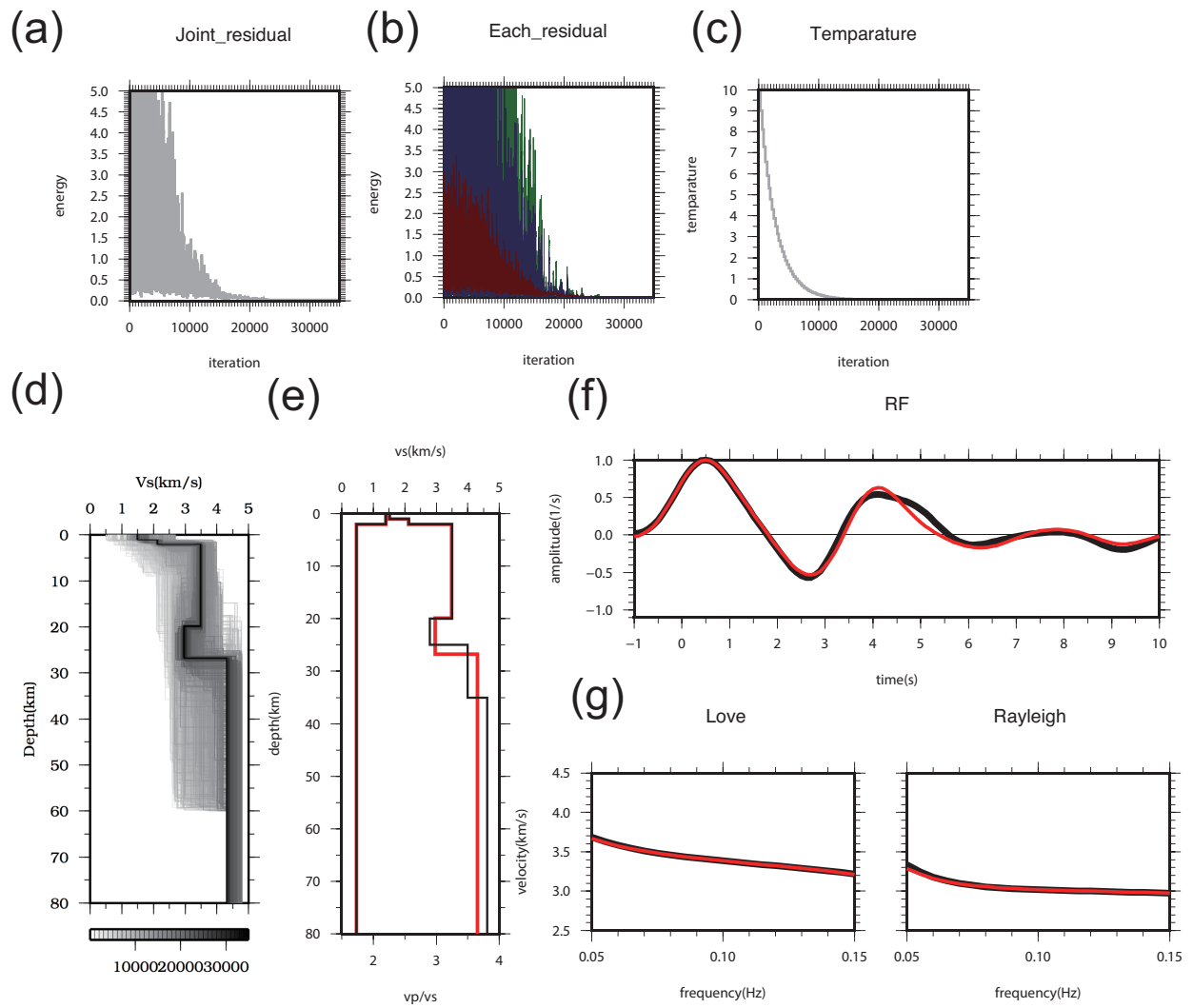
Figure 5.6: Same as Figure 5.4 but for the synthetic test 3.
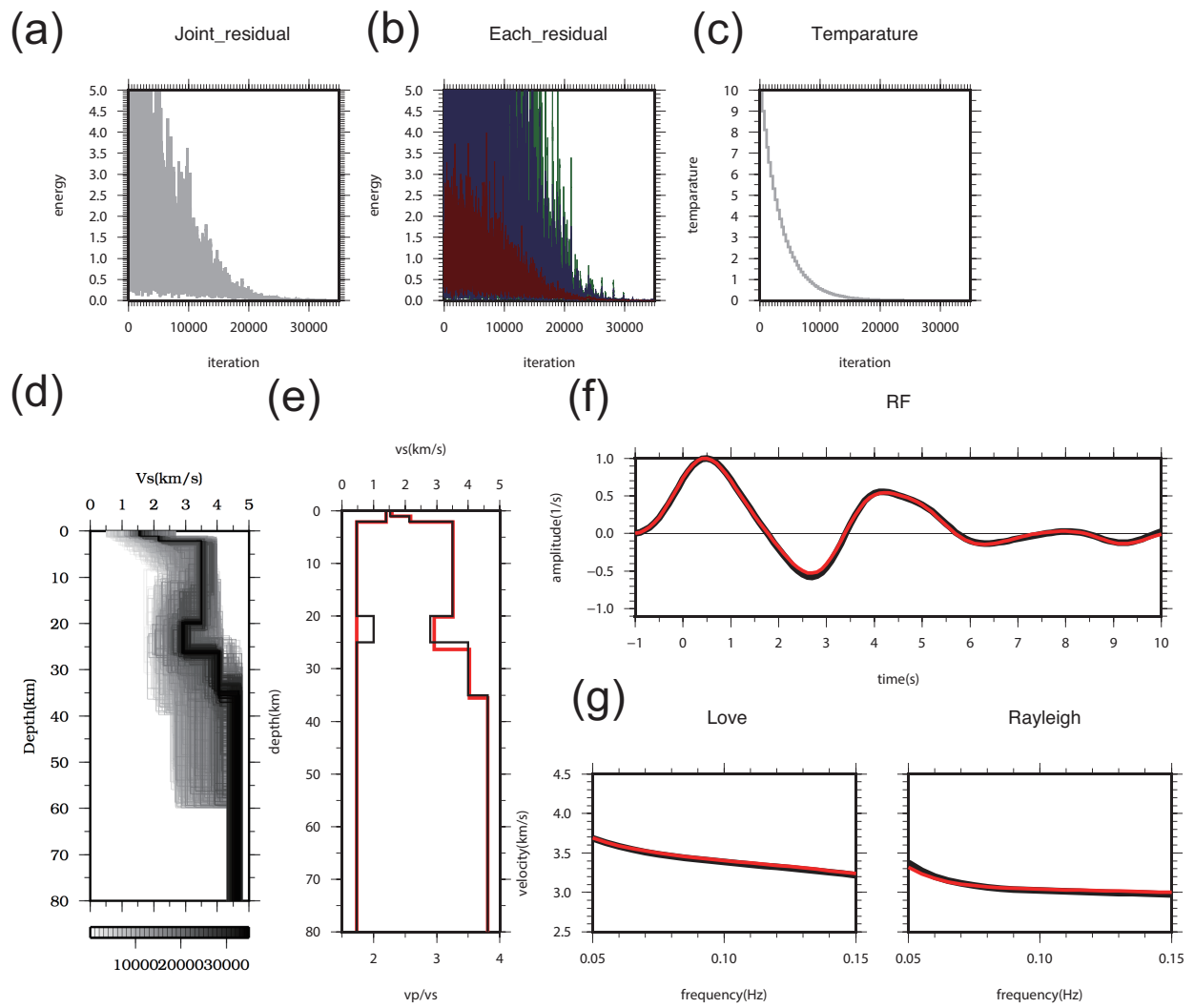
Figure 5.7: Same as Figure 5.4 but for the synthetic test 4.

5.4 Examples of inversion results at two stations

In this section, we show examples of the inversion results at two stations near Mt. Fuji with uncertainties. We calculated composite radial RFs by stacking all RFs with a specified bin of back azimuths to reduce noise. We set the bins with a width of 60 degrees and spacing of 30 degrees (Figure 5.8). Each RF is then averaged by being weighted according to the inverse variance in frequency domain (*Park and Levin*, 2000).
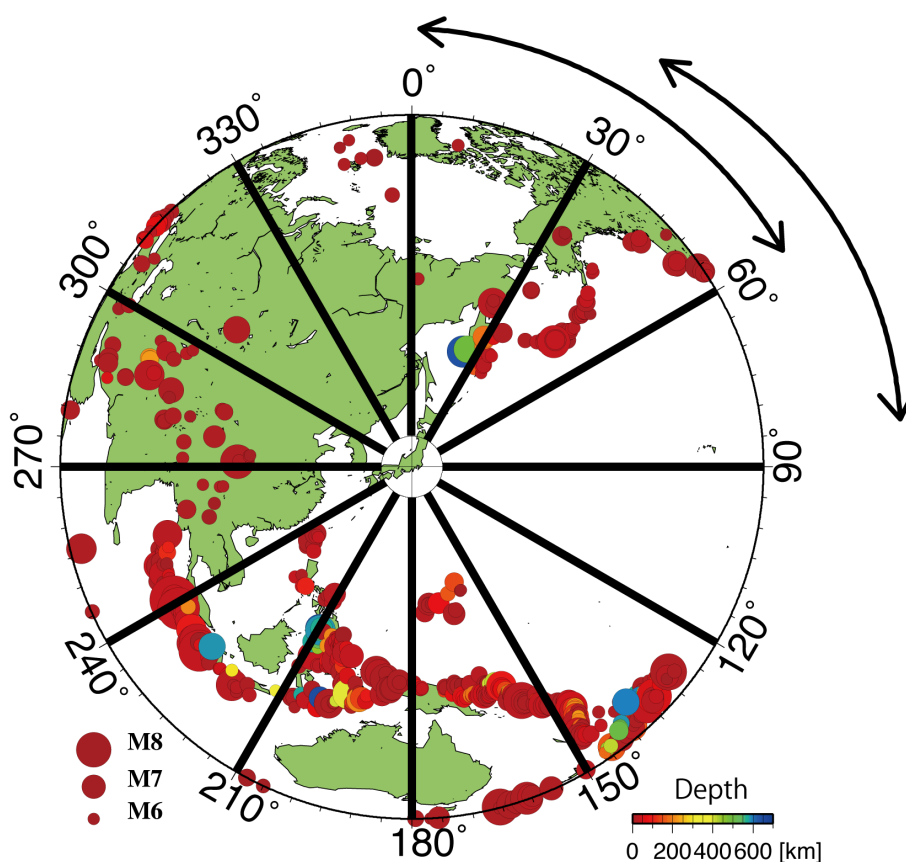
Figure 5.8: The backazimuth range used in calculating composite RFs.
Same as Figure 3.2 but with the distribution of bins. Black solid lines indicate the bin spacing and range used in the stacking.

5.4.1 Station FUJ

Figure 5.9a and b denote the observed and composite RFs at the station FUJ from the back azimuth of between 120 and 180 degrees, respectively, as an example. The number of RFs used in this bin is 149. A bootstrap estimation (e.g., *Efron and Tibshirani*, 1991) evaluates errors in the stacked RF. Bootstrap estimations can calculate the distribution of a statistic (e.g., average values) without assuming the probability distribution of the data. First, averaging resampled 149 RFs by allowing overlapping among the original 149 RFs gives an averaged RF. Repeating this one hundred times gives one hundred averaged RFs. Gray solid lines in Figure 5.9b show one-hundred RFs generated by resampling and averaging. Figure 5.9b indicates that the uncertainty of resampled RFs is small and all of these RFs have large negative phases at about 3 and 7.5 seconds, representing a low velocity region below the station.

Figure 5.10 shows the result of the SA inversion for S-wave velocities, showing that a distinct low velocity layer between about 16 and 21 km (Figure 5.10e). The dispersion curve of the Rayleigh wave is not reconstructed at all because the parameter c in equation (5.6) is only 0.05, so the inversion favors a model whose RF fits well with the observed data. Also the low velocity layer required to fit the observed RF is too deep for surface waves of the period in this study to be locally sensitive. We discuss the detail about this problem in Chapter 5.6 and 6. Then, inversions are executed with one-hundred bootstrap RFs to estimate uncertainties in the result of the SA inversion (Figure 5.11). The mean value and the standard deviation σ of model parameters are listed in Table 5.2. The uncertainties of model parameters are basically larger at depth except that for those in Layer 5. In other words, our inversion constrains velocities and the depths of interfaces at shallower depth better.

5.4.2 Station MMS

Figures 5.12 and 5.13 show the bootstrap estimations and the inversion results with bootstrap RFs at the station MMS from the back azimuth of between 120 and 180 degrees, respectively.

Velocity models obtained from the inversions are divided into three categories: 94 models in group 1, 5 in group 2, and 1 in group 3. The least squares errors defined in equation (5.6) are between 0.142 to 0.204 in group 1, between 0.186 to 0.194 in group 2, and 0.152 in group 3. Solutions in group 2 are likely those at local minima because the cooling in the SA inversions is not slow enough for a computational reason (See equation 5.3). To confirm this possibility, we have changed the cooling schedule so that the temperature more slowly with $rt = 0.95$ and $ns = 80$. Solutions with the new cooling schedule, however, are divided into three groups (Figure 5.15). This variety could be because the back azimuths of RFs being stacked are various so that the shapes of RFs generated through bootstrap are also various. However, we consider the group 1 is appropriate to represent the RF at MMS because almost all the velocity models belong to the group 1 in both Figures 5.15a and b. Furthermore, the velocity structures in group 1 reconstruct the negative phase at about 7–8 seconds better than those in group 2 and 3. The mean value and the standard deviation σ of each parameter are listed in Table 5.2.

FUJ_W

(a)

(b)
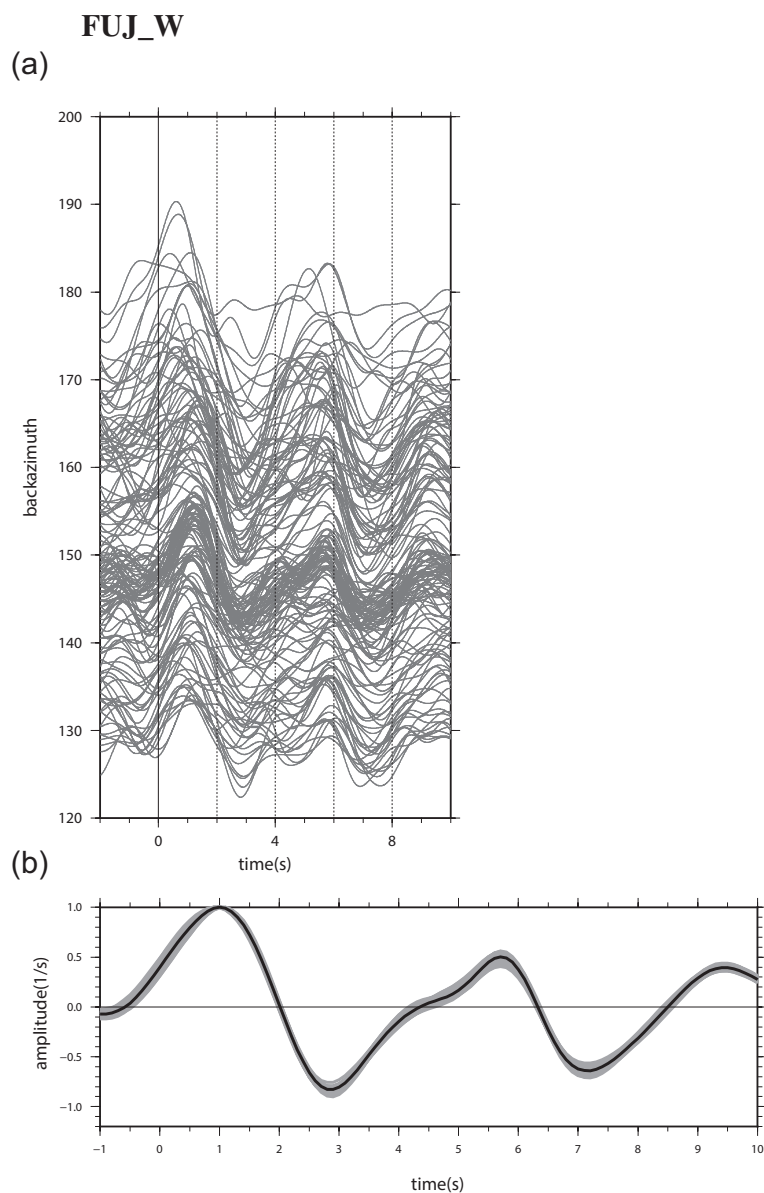
Figure 5.9: The observed and composite RFs at station FUJ.
(a) Individual RFs calculated from observed dataset used in the composite RF at FUJ from back azimuths between 120 and 150 degrees. (b) Stacked RFs (black) and the results of bootstrap estimations of the stacked RFs (gray). Bootstrap estimations are executed one-hundred times.
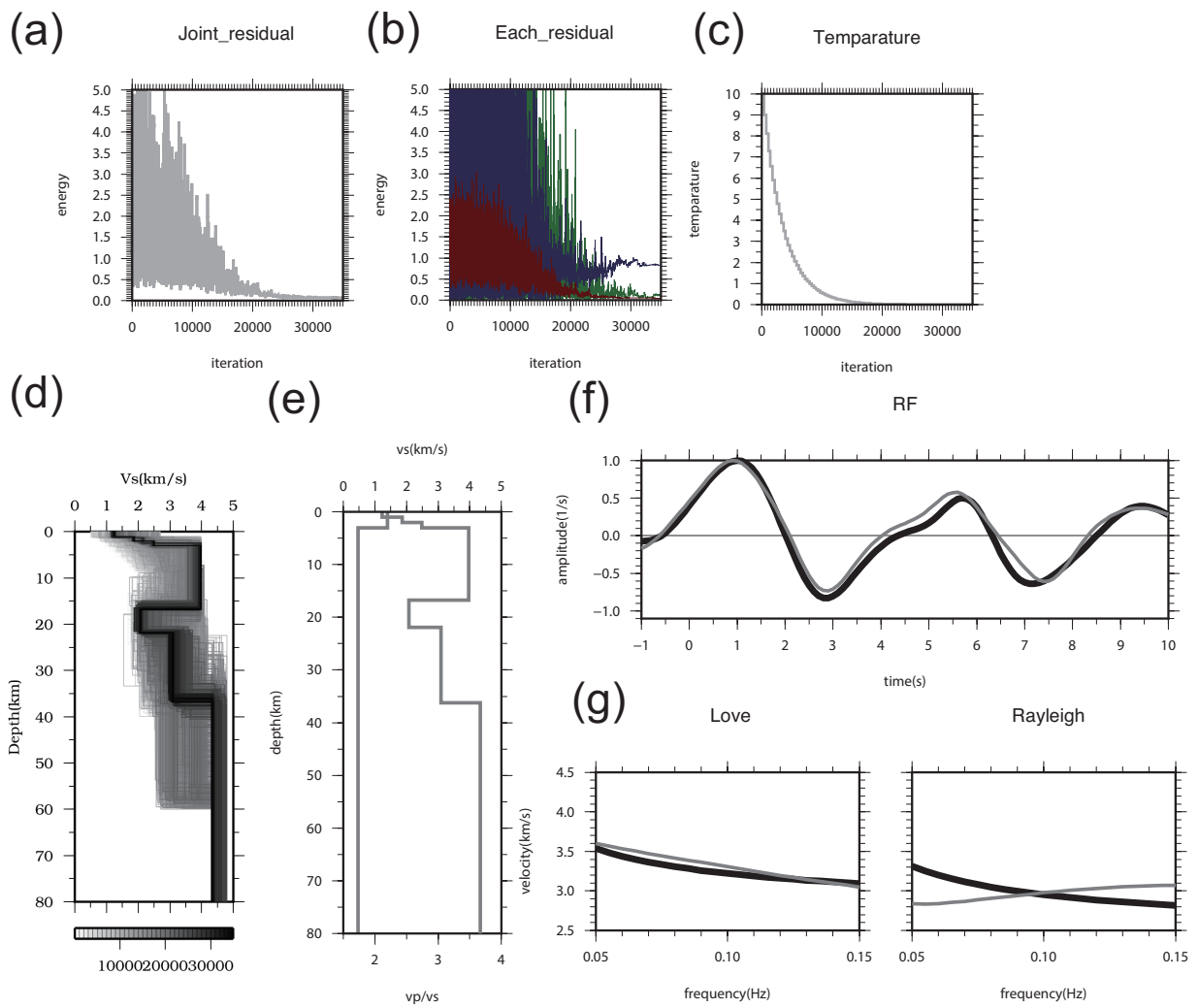
Figure 5.10: Same as Figure 5.4 but for the station FUJ.
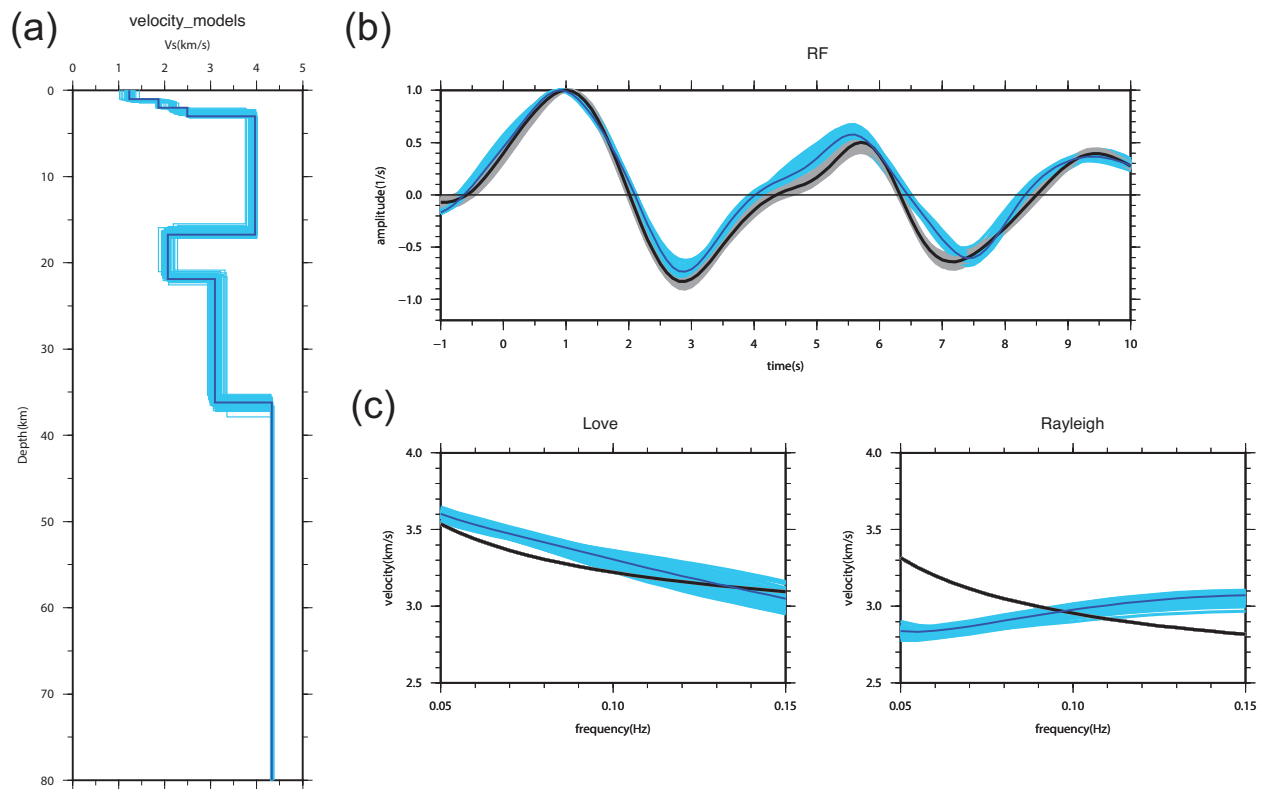
Figure 5.11: The results of SA inversions at FUJ from the bootstrap analysis.
(a) Velocity models obtained by the SA inversion to the observed RF (blue) and one-hundred bootstrap RFs (aqua). (b) Comparison of RFs between the bootstrap estimates (gray) and the optimum results from SA (aqua). Black and blue lines represent the observed data and the optimum solution derived by SA. (c) Same as (b) but for dispersion curves of Love (left) and Rayleigh (right) waves.

MMS_W

(a)

(b)
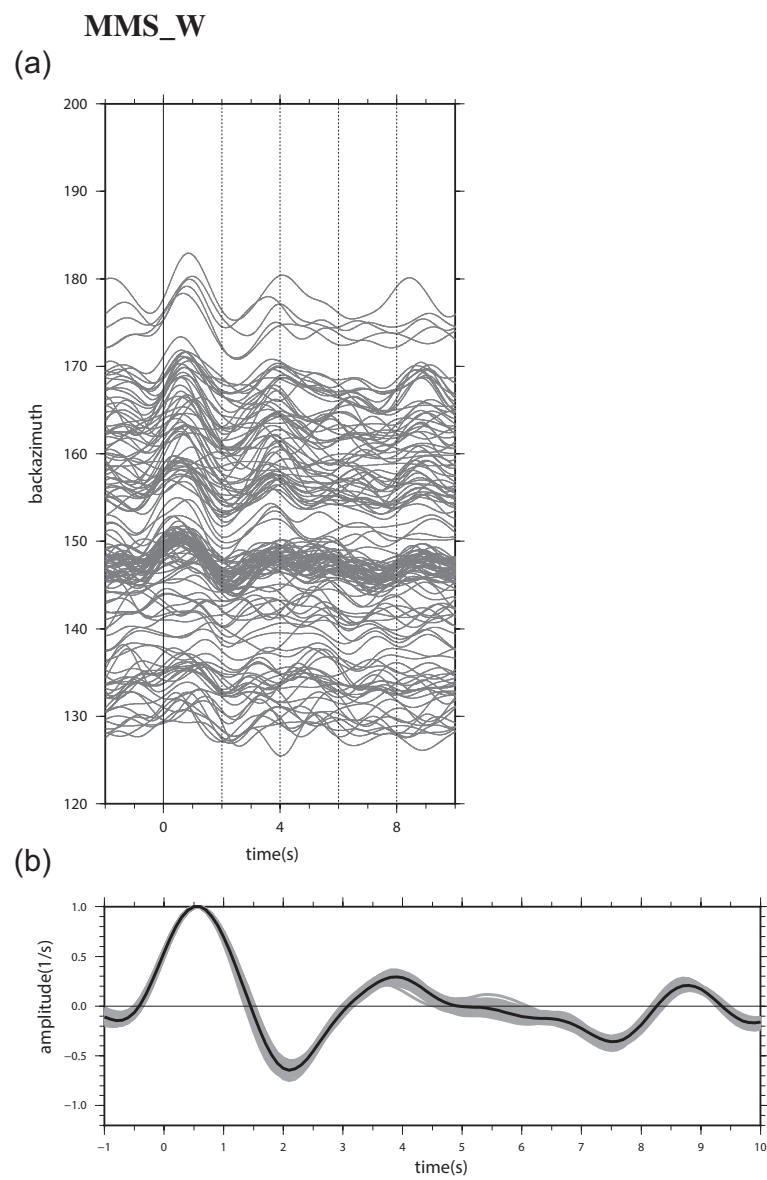
Figure 5.12: Same as Figure 5.9 but for the station MMS.
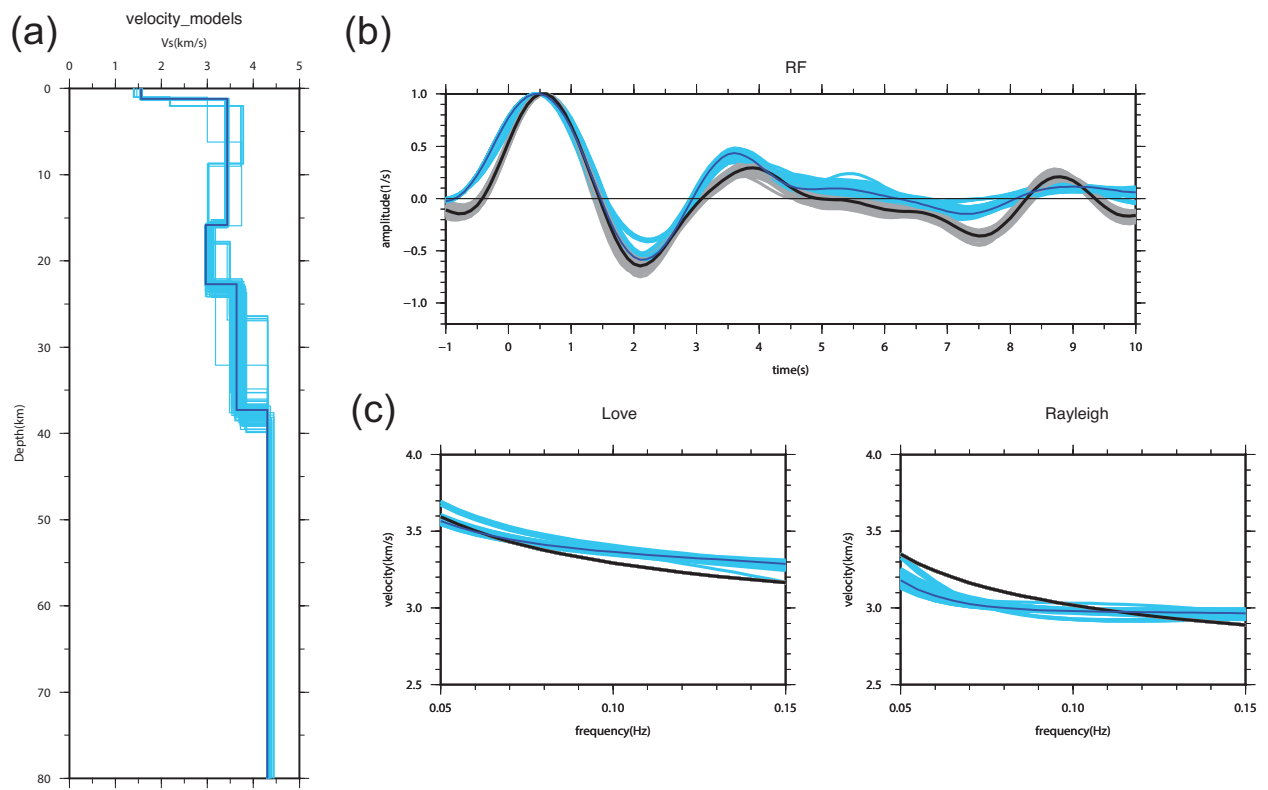
Figure 5.13: Same as Figure 5.11 but for the station MMS.
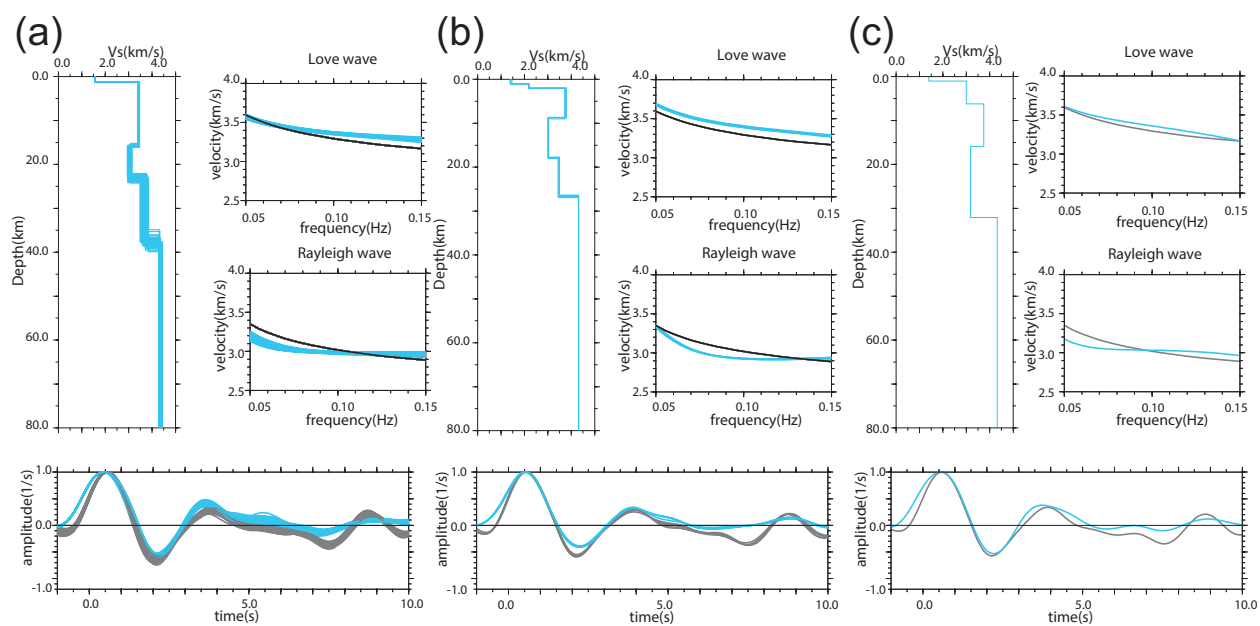
Figure 5.14: Three groups of solutions at the station MMS.
Parameters are same as those in Figure 5.13. (a) group 1 with 94 RFs. (b) group 2 with 5 RFs. (c) group 3 with a single RF.
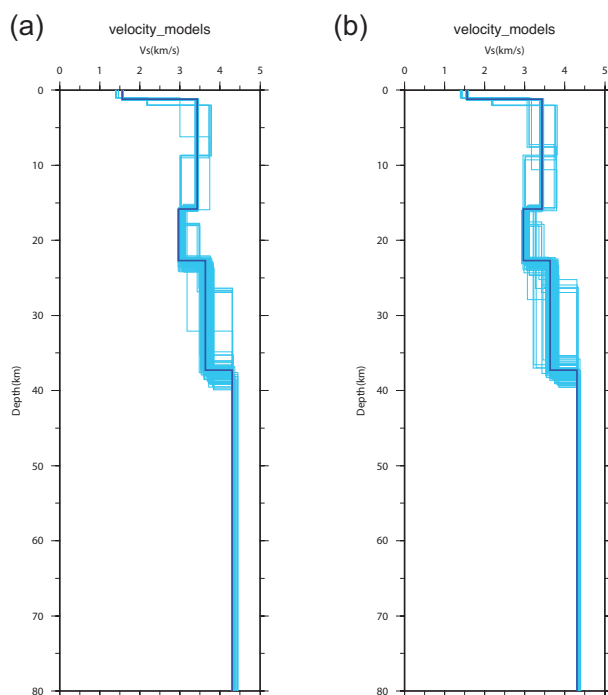
Figure 5.15: Comparison of SA results between different parameters.
(a) $rt = 0.90$, $ns = 40$ (same to Figure 5.13). (b) $rt = 0.95$, $ns = 80$.

		bottom depth [km]			Vs [km/s]		
	Layer	name	mean	σ	name	mean	σ
station FUJ	Layer 1	Da	2.807	0.285	v1	1.231	0.063
	Layer 2	Db	16.526	0.353	v2	3.958	0.048
	Layer 3	Dc	21.738	0.298	v3	2.052	0.063
	Layer 4	Dd	36.399	0.45	v4	3.104	0.08
	Layer 5				v5	4.313	0.014
staion MMS	Layer 1	Da	1.238	0.029	v1	1.556	0.01
	Layer 2	Db	15.756	0.181	v2	3.417	0.019
	Layer 3	Dc	22.973	0.46	v3	3.038	0.048
	Layer 4	Dd	37.76	0.938	v4	3.67	0.094
	Layer 5				v5	4.32	0.029

Table 5.2: Uncertainties of the SA inversions at stations FUJ and MMS. Parameter names and standard deviations of model parameters are listed. Standard deviations of model parameters are estimated by the bootstrap calculation at the station FUJ and the main solutions at the station MMS.

5.5   S wave velocity around Mt. Fuji

We conducted SA inversions for RFs observed at all stations around Mt. Fuji. The selections of RFs used in the inversions follow two criteria, which are 1) more than 15 RFs are used to compose a stacked RF, and 2) depths of seismic sites are less than 300 m, to incorporate only RFs with good quality in the analysis and to get rid of the effect of the reflection from the surface layer which is not taken into account in our calculations.

Figures 5.16 and 5.17 represent S wave velocities obtained from SA inversions along the SE-NW and SW-NE cross sections (same profiles as Figures 4.8b and d), respectively. The S wave velocity structures, with the least squares errors of the velocities defined in equation (5.6) less than 0.3, are mapped along their ray paths of the S wave through an inversion result as is the case with the radial RF cross sections. In these figures, we used the SA results that the depth of the upper boundary of the bottom layer (parameter Dd in Table 5.1) is determined shallower than 50 km, because we consider that the later phase of RFs is generated solely by reverberations at shallow layers and the depth of the lowest velocity boundary is not well constrained by the inversion if the parameter Dd is greater than 50 km.

If multiple rays intersect the same grid, we take the weighted average of S wave velocities obtained from multiple rays according to the least squares errors. The maximum and minimum weights in the same bin are set to be 1.0 and 0.5, respectively, and weights of other rays are set between 0.5 and 1.0 according to their least squares errors as following equation.

$$weight(n) = 1.0 - 0.5 \cdot \frac{E(n) - E(min)}{E(max) - E(min)} \tag{5.13}$$

where n, E(n), E(min), and E(max) represent the individual ray, the residual of the ray in equation (5.6), the minimum value of the residual in the grid, and the maximum value of the residual in the grid, respectively. Then, the S wave velocity in each grid is averaged with those in the right and left grid, that is, the velocities are averaged over 12 km in the horizontal direction.

Figure 5.16 shows a high velocity body subducting from south to north, representing the subducting crust of IBM, and a low velocity body with the S wave velocity about 3.0 km/s at about 20 km below Mt. Fuji (Figure 5.16a). Figure 5.17 shows two low velocity regions between -100 and -30 km at 0–20 km depths and between 60 and 100 km at 30–50 km depths. A comparison with this velocity structure with the distribution of hypocenters and the geometry of subducting plates by *Nakajima et al.* (2009) denoted in Figure 5.17c demonstrates that these low velocity layers represent the low-velocity oceanic crust in the subducting PHS. Figures 5.17a and 5.18a show that, below Mt. Fuji, there is distinct low velocity region with a width of 40 (km) in horizontal direction and 20 km width in vertical direction. Number of RFs that satisfies the conditions listed above is less with the four-layer model without low velocity layers than with the five-layer model (Figure 5.18), and the least squares errors is sufficiently smaller in the five-layered model (Figure 5.19), indicating that the five-layered model allowing low velocity layers better reconstructs the S-wave velocity structure from the observed RFs.
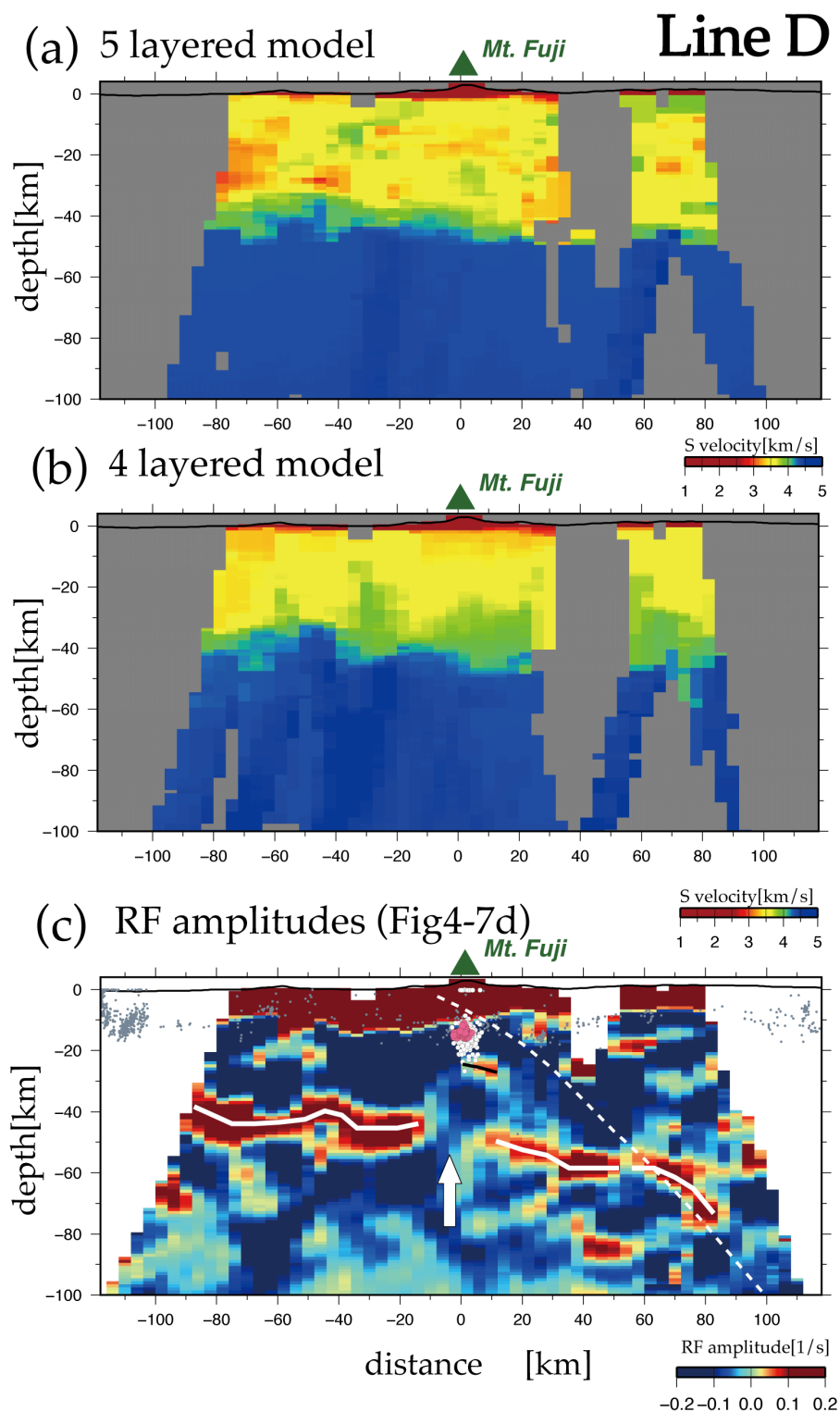
Figure 5.16: The S wave velocity structure the SE-NW cross section (same as Line D in Figure 4.1.
The cross section is the same as that in Figure 4.10d. (a) five-layered model. (b) four-layered model without low velocity layers. (c) RF amplitudes (same as Figure 4.10d)
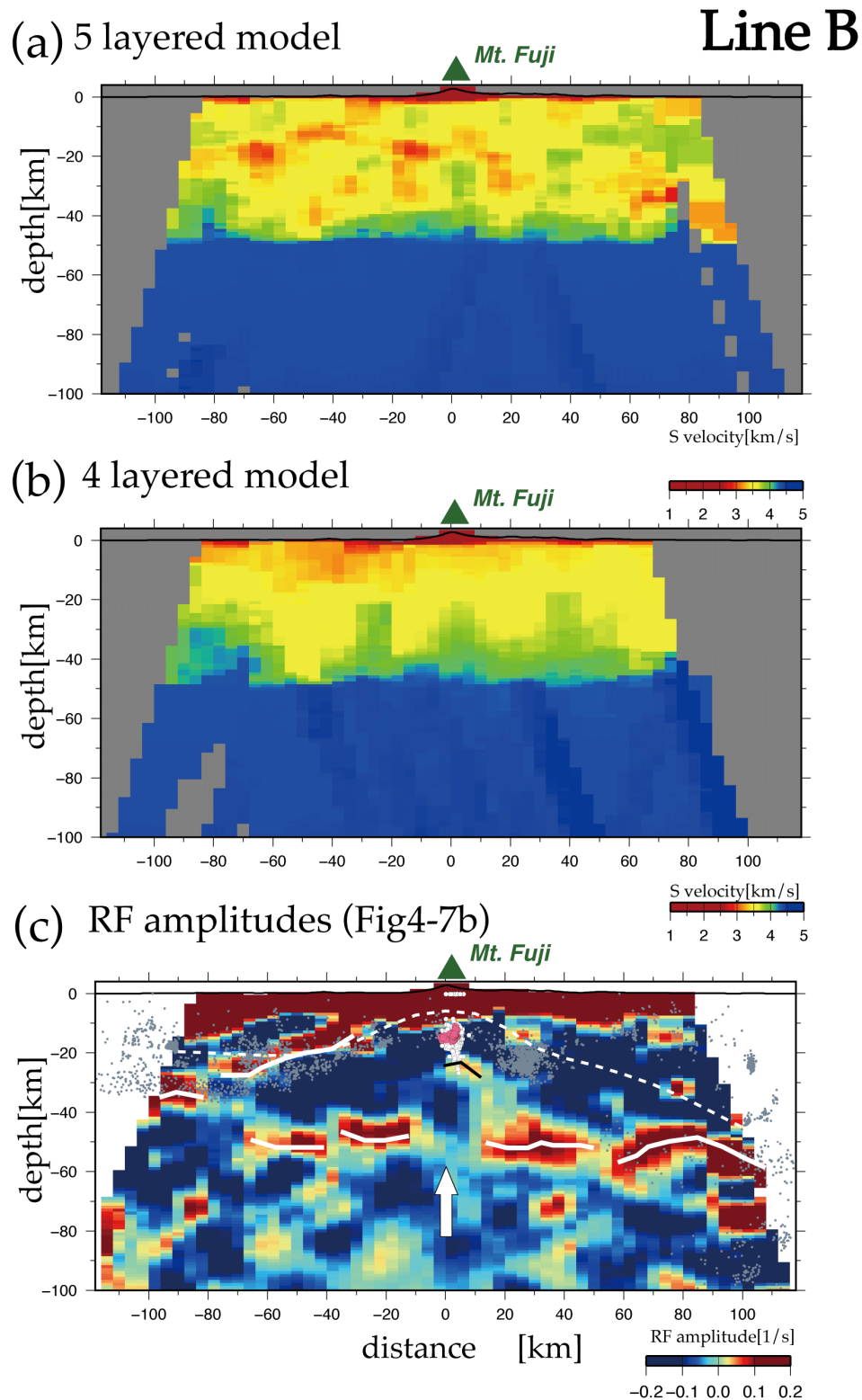
Figure 5.17: The S wave velocity model along the SW-NE cross section (same as Line B in Figure 4.1).
The cross section is the same as that in Figure 4.10d (a) five-layered model. (b) four-layered model without low velocity layers. (c) RF amplitudes (same to Figure 4.10b)
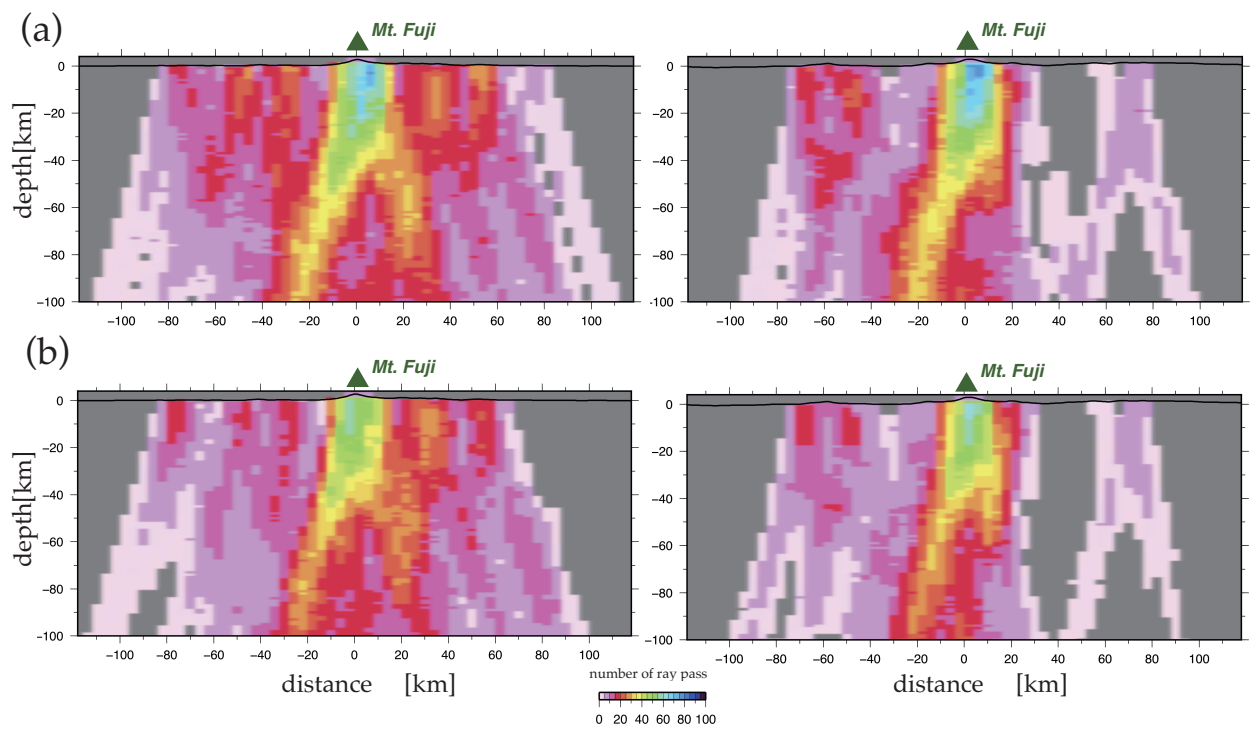
Figure 5.18: Number of RFs used to estimate the S wave velocity at each grid. Darker colors denote more rays passed through the grid. (a) Five-layered model along the SW-NE (left) and SE-NW (right) cross sections. (b) Same as (a) but with the four-layer model.
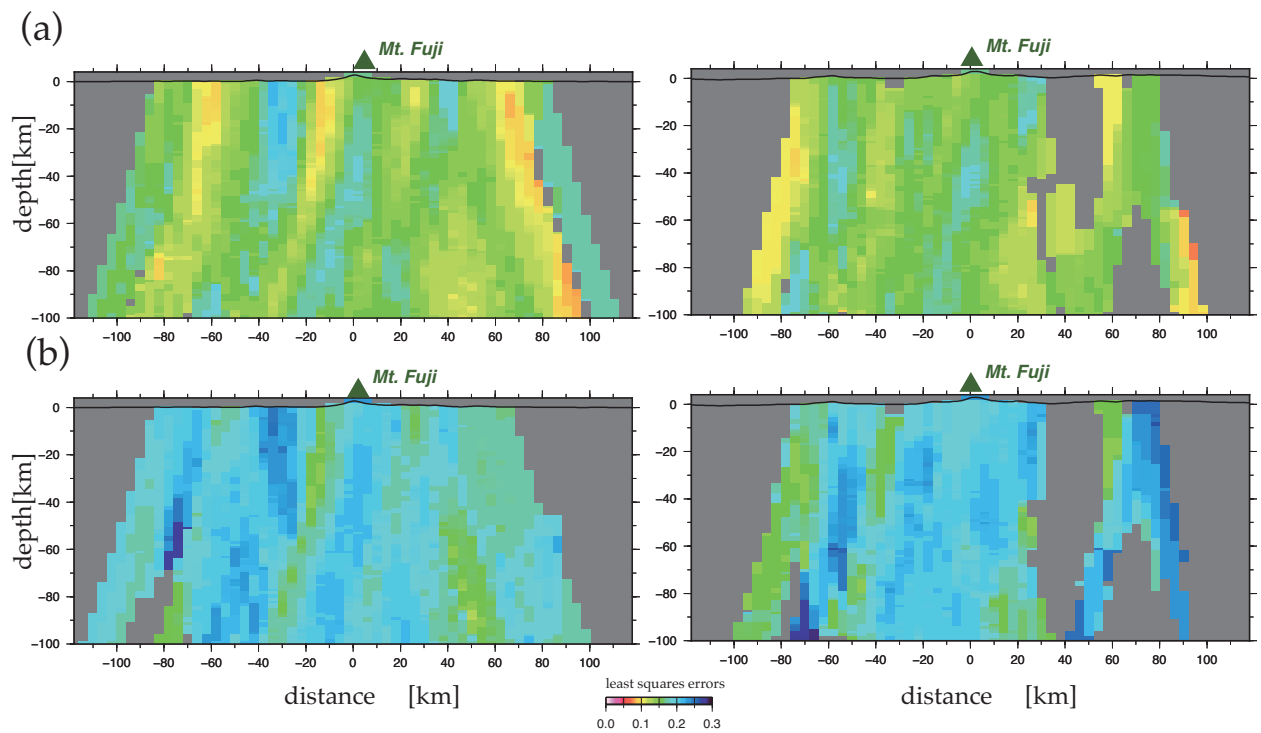
Figure 5.19: Least squares error, defined in equation (5.6), of S-wave velocities.
(a) Five-layered model along the SW-NE (left) and SE-NW (right) cross sections. (b) Same as (a)
but with the four-layer model.

5.6   Uncertainties of velocity models

5.6.1   The influences of the dispersion curve of the Rayleigh wave

Because the dispersion curves of the Rayleigh wave is not reconstructed at all as shown in Figure 5.10, we performed some tests to understand the uncertainties of the SA inversion used in this study. First, we execute the SA inversion at FUJ with RFs and the dispersion curve of the Love wave to make sure that the Rayleigh wave lead the inversion results to the incorrect velocity models. In other words, we need to confirm whether the inappropriate dispersion curves at station FUJ make the inversion stable in the results which are not the true velocity models. Figure 5.20 shows the comparison of the results of using both the Rayleigh and the Love wave and those of using only the Love wave. The results using only the Love wave show the similar velocity models with those using both the Love and the Rayleigh wave, supporting that the un-modeled Rayleigh wave have little influence on the inversion results. The reason why the Rayleigh wave is not reconstructed at FUJ is the existence of the wide and deep low velocity layer at depths between about 17 and 36 km. If there is a deep and wide low velocity layer, the dispersion shows the very complex behavior and it become difficult to discriminate the fundamental mode and the first overtone. However, the dispersion curves of *Nishida et al.* (2008) in deeper depth reflect the averaged velocity model and those do not contain the distinct deep low velocity layer. The joint inversion considering the multimode of the dispersion curves of the Rayleigh wave will improve the reconstruction of the Rayleigh dispersion in the solution. However, we believe that inversion results are not contaminated by the Rayleigh wave because the Rayleigh wave does not have negative effects at the station FUJ where a deep low velocity layer exists as described above.

5.6.2   Comparison with the different values of the weight parameter

Next, we check the validity of the weight parameter with a value of 0.05. Figures 5.21 and 5.22 depict the influence of the inversion results with c=0.0, 0.01, 0.05, and 0.1 at station FUJ. The result of the inversion using only RFs (Figure 5.21a) shows that RFs could not constrain

the absolute value and is unstable because RF amplitudes are sensitive to the contrast of S wave velocities as described in Chapter 2.3 and 5.1. On the other hand, inversions with the constant parameter as 0.01, 0.05, and 0.1 lead almost the same results. The joint inversions of RFs and surface wave dispersions can constrain the absolute value of the S wave velocity and solve the inversion without unrealistic velocity structure in a stable manner. Also, the results of inversions do not depend on the weight parameter c between 0.01 and 0.1, supporting that the constant value of 0.05 is reasonable in this study.

5.6.3   Using other velocity models as observation

In the next step, we confirm that the validity of using the velocity model of *Nishida et al.* (2008) as observation. Figure 5.23 represents the results of SA inversions with dispersion curves calculated by velocity models of JMA (*Ueno et al.*, 2002) and *Nakamichi et al.* (2007). We set $Disp_{Nishida}$ in equation (5.8) to the dispersion curves based on JMA model or *Nakamichi et al.* (2007), and set $Disp_{reference}$ to the dispersion curves based on *Nishida et al.* (2008). The velocities deeper than 30 km of *Nakamichi et al.* (2007) are calculated using the JMA velocity model. Velocity patterns of the inversion results in Figure 5.23 are very similar to those in Figure 5.22a, supporting that the results do not change significantly by the dispersion curves used in the inversion. The velocities of low velocity layers are higher and the depth of the low velocity layer are deeper in 5.23 than those in 5.22a, because the S wave velocities in JMA and *Nakamichi et al.* (2007) are faster than those in *Nishida et al.* (2008). However, we believe that the velocity model using *Nishida et al.* (2008) is worthy of trust around Mt. Fuji because the velocity models inverted with *Nishida et al.* (2008) are included in those using only RF (Figure 5.21a). Also, the RFs calculated using the results of inversion with *Nishida et al.* (2008) fit better than those with JMA and *Nakamichi et al.* (2007), especially at a negative phase at 6–9 seconds generated by the multiple reflection of the top of the low velocity zone. In other words, the velocity model by *Nishida et al.* (2008) can select the realistic velocity models among the results that are calculated using only RFs.

The RF at station FUJ requires the distinct low velocity layer as the results by *Nishida et al.* (2008)

(a)Rayleigh & Love

(b)Love
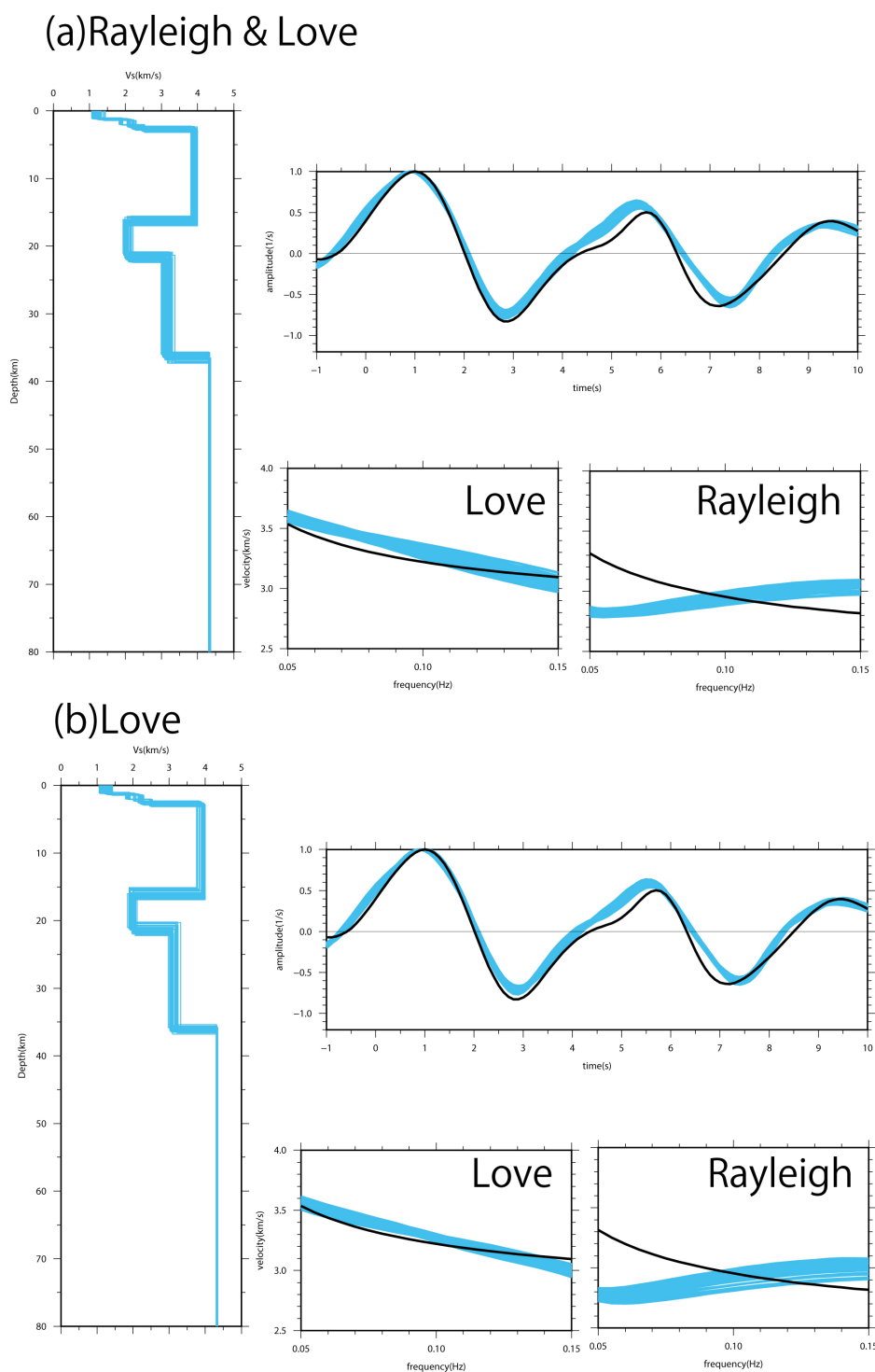
Figure 5.20: Comparison of inversion results 1.

The results of inversions at station FUJ using (a) both dispersion curves of the Love and the Rayleigh wave, and (b) only the dispersion curve of the Rayleigh wave. The weight parameter c is set to be 0.05. Aqua lines represent the best fifty models of the inversion executed one-hundred times. Black lines show the observations.
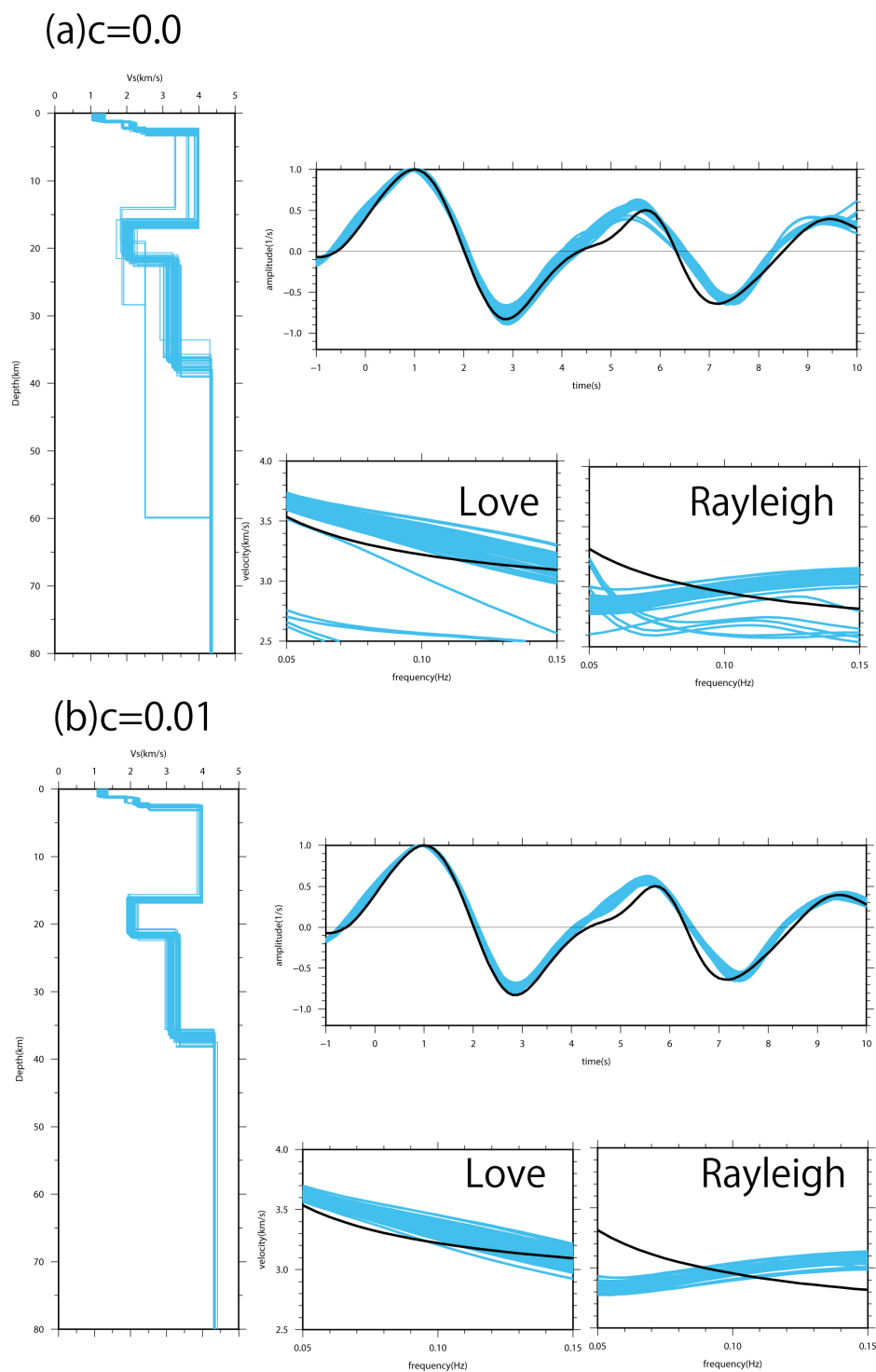
Figure 5.21: Comparison of inversion results 2.
Comparison of SA results at station FUJ with different values of the weight parameter c. The parameter c is set to be (a) 0.0 and (b) 0.01. The parameters are same as those in Figure 5.20.

(a)c=0.05

(b)c=0.1
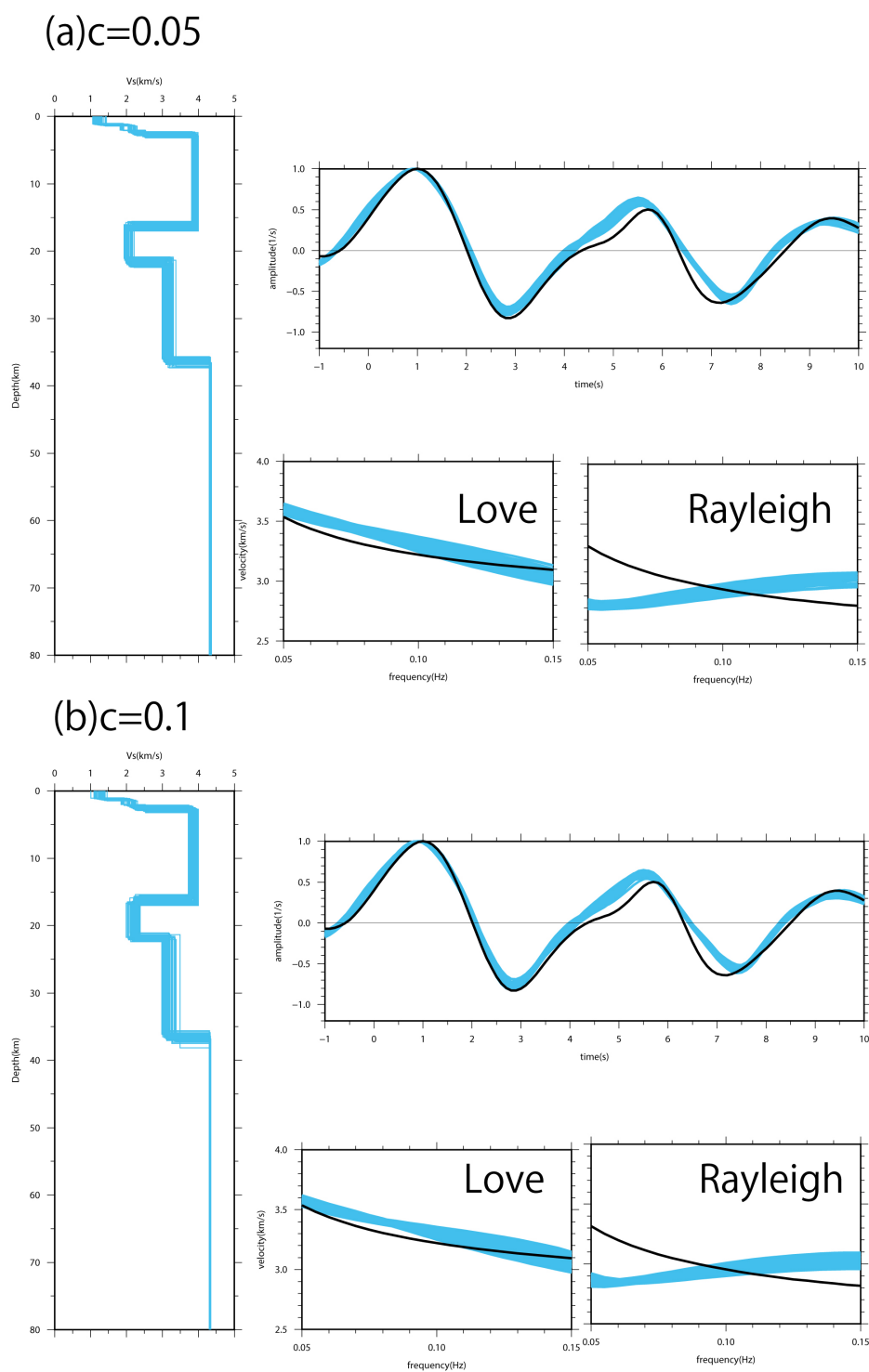
Figure 5.22: Comparison of inversion results 3.
Same as Figure 5.21, but for different c as (a) 0.05 and (b) 0.1
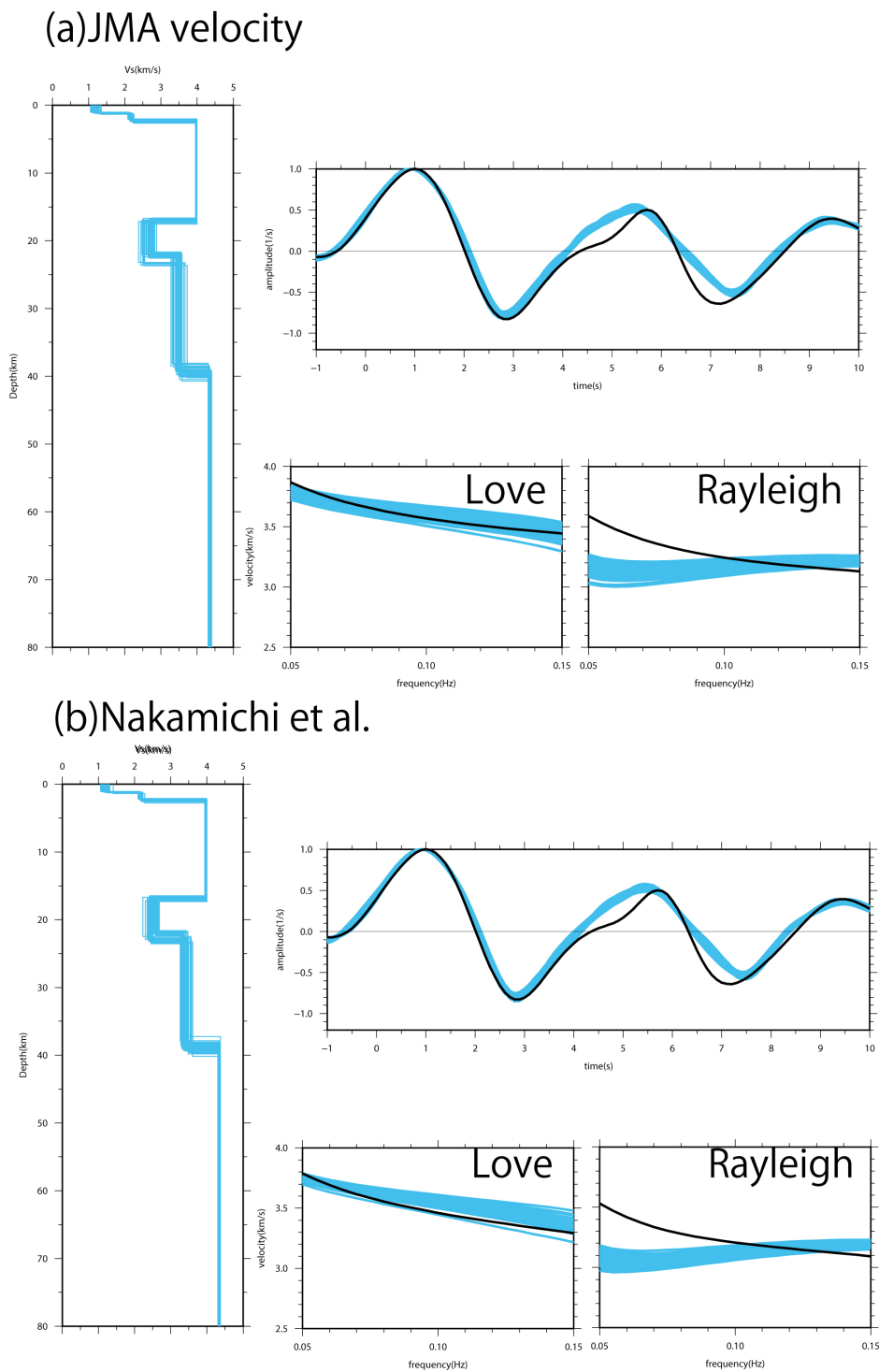
Figure 5.23: Comparison of inversion results 4.
Comparison of SA results at station FUJ with different dispersion curves as observations. (a) JMA velocity model. (b) Nakamichi et al. (2007) The parameter c is set to be 0.05.

5.6.4   Comparison of the inversion results at different stations and back azimuths

Figures 5.24-5.26 depict the examples of the inversion results at eight stations with different back azimuths.

The RF results at station H.SBKH require low velocity layers in all directions. Comparison with the S wave velocity image (Figure 5.17), the low velocity zone at depths of 30–50 km from the back azimuth of 30 degree represents the deep low velocity layer below Mt. Fuji, whereas the low velocity zones at depths of 10–20 km from the back azimuth of 120 degree and at depths of 15–20 km from the back azimuth of 300 degree represent the oceanic crust of subducting PHS plate. The low velocity zone at depths of 25–50 km required by the RF from the back azimuth between 240 and 300 degree reflects the very local structure, because this is unapparent in the velocity image (Figure 5.17).

The RFs at station ANMY are similar to those at station FUJ. Inversion results at ANMY require the narrow distinct low velocity layer at depths between 15–20 km and wide low velocity layer at depths between 20–35 km.

At station FUJ, the RF from the back azimuth of 30 degree have different characteristics as compared with that from the back azimuth of 150, 240, and 300 degrees. There is a distinct negative phase at 5 seconds in the RF from 30 degree that is not reconstructed from the inversion, representing that the complicated velocity structure at depth deeper than 30 km just below Mt. Fuji.

The results of SA inversions at FUJ2 show that there is a low velocity region at depths between 30–50 km. However, it is possible that a low velocity region exists in shallow part (about 10–20 km) because the thickened low velocity volcanic sedimentary layer below FUJ2 makes the direct phase very complicated and the inversion result does not reconstruct the direct phase (at about 2 seconds in RFs at FUJ2). Furthermore, the negative phase at 5 seconds require the low velocity layer at deep part below FUJ2, the five-layered model does not make the low velocity layer at

shallow part. The similarity of RFs from the back azimuth of 30 degree at FUJ and that from 210 degree at FUJ2 shows the complicated structure between FUJ and FUJ2 at deep part.

The characteristics of RFs observed at station MMS have different characteristics according to the back azimuth. The RFs from the back azimuths of 150 and 300 degree show the low velocity layer between 10–22 km, whereas those from the back azimuths of 30 and 210 degree show the low velocity layer between 30–50km. This result strongly suggests that the depth variation of the low velocity region below Mt. Fuji. Also, the similarity in a negative phase at about 5–6 seconds of RFs from 210 degree between MMS and FUJ2, which is not reconstructed by the SA inversion, shows the complex structure at deep part just below Mt. Fuji.

Below the station N.FY1V, there are deep low velocity layers at depths between 20 and 40 to explain the distinct positive phases at about 5–6 seconds in RFs from the back azimuths of 240 and 300 degrees. The dispersion curves of the Rayleigh wave are not reconstructed at all as is the case with the station FUJ.

At station H.TU2H, the inversion result of the RF from the back azimuth of 300 degree requires a low velocity layer at depths between 20 and 40 km, whereas that from the back azimuth of 30 degree does not require a low velocity layer, indicating the eastern boundary of the low velocity layer below Mt. Fuji.

At the station AKY, distinct low velocity layers are not required from the back azimuths of 30 and 150 degrees, representing that the low velocity zone below Mt. Fuji does not continue to the east of AKY as is the case with the station H.TU2H. The small low velocity region at 30–40 km depth from the back azimuth of 300 degree may indicate the eastern boundary of the low velocity layer below Mt. Fuji.

To summarize the inversion results at stations described above, the low velocity layer is required to satisfy the RFs at stations around Mt. Fuji.
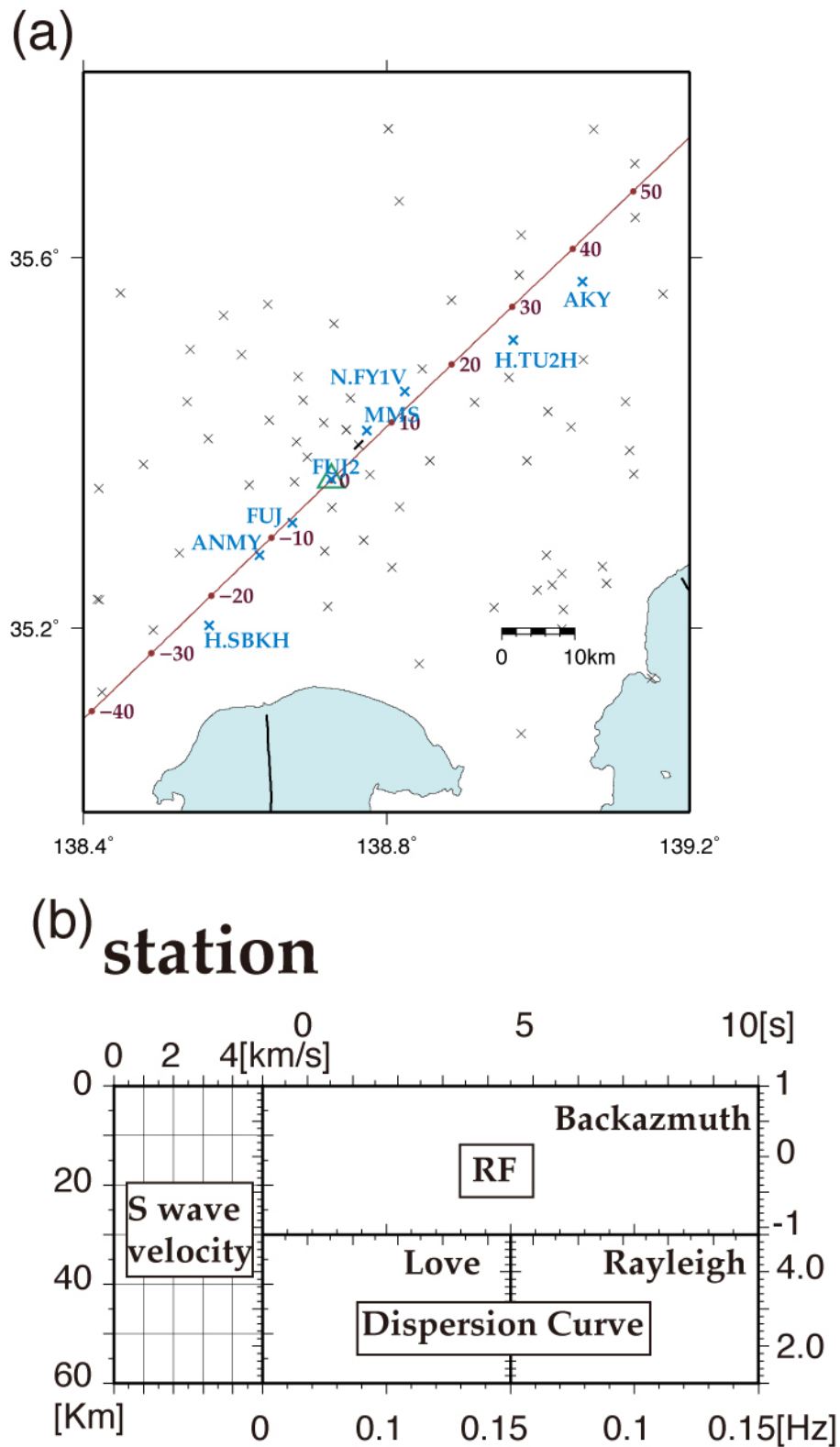
Figure 5.24: Distribution of station locations along the SW-NE cross section (Line B).
(a) Black and aqua cross signatures show the distribution of station locations. The aqua cross signatures with names represent the typical stations used in Figures 5.25-5.26 as examples. (b) Parameters used in Figures 5.25-5.26.
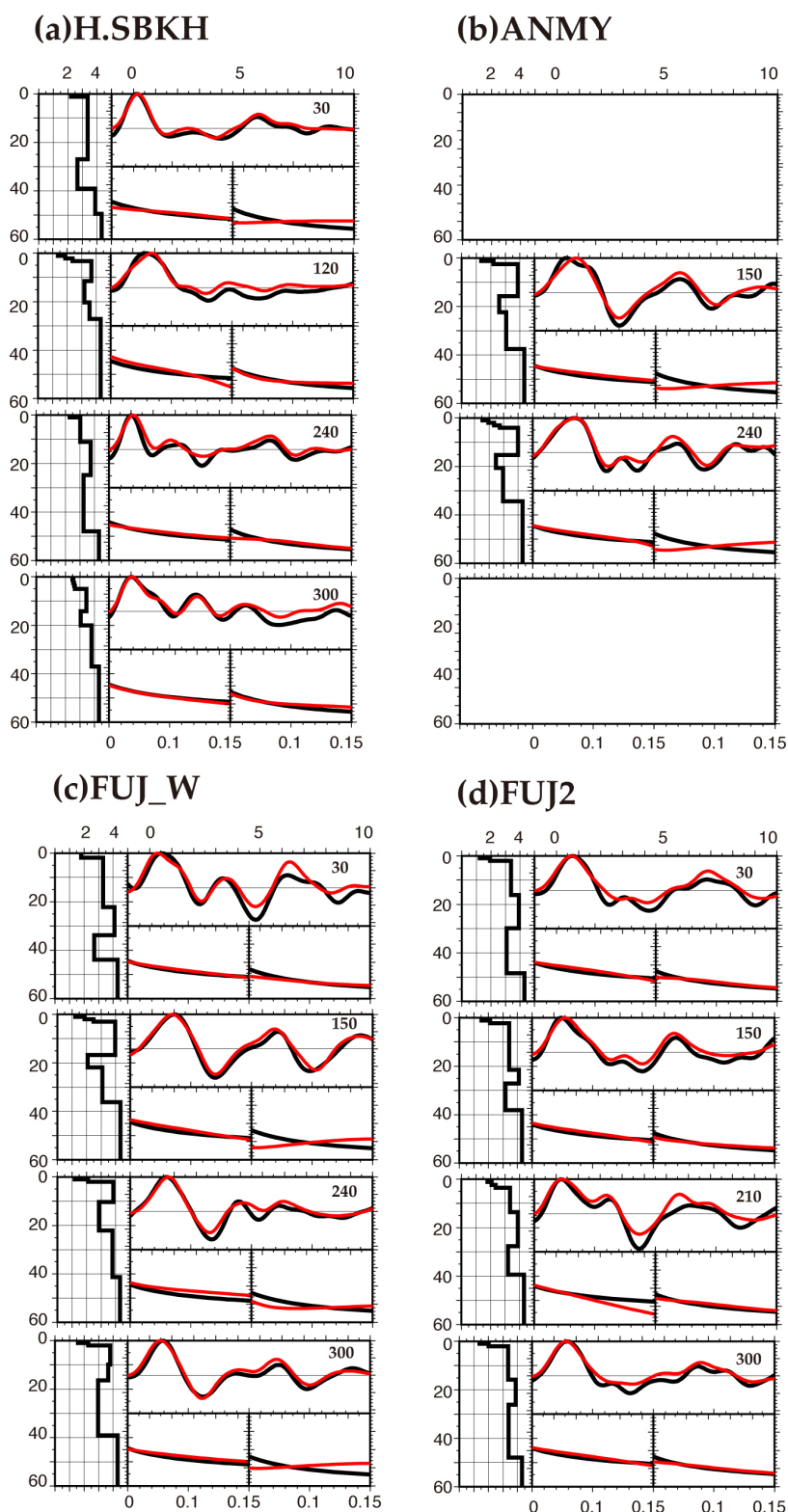
Figure 5.25: Examples of inversion results 1.

Comparison of the inversion results at different stations and back azimuths: (a) H.SBKH, (b) ANMY, (c) FUJ, and (d) FUJ2. Parameters are listed in 5.24. The value of back azimuth in each panel represents the center of the bin in Figure 5.8. For example, back azimuth 30 degree represents the range between 0 and 60. Black and Red lines in RF and dispersion curves represent the observed and the inverted models.
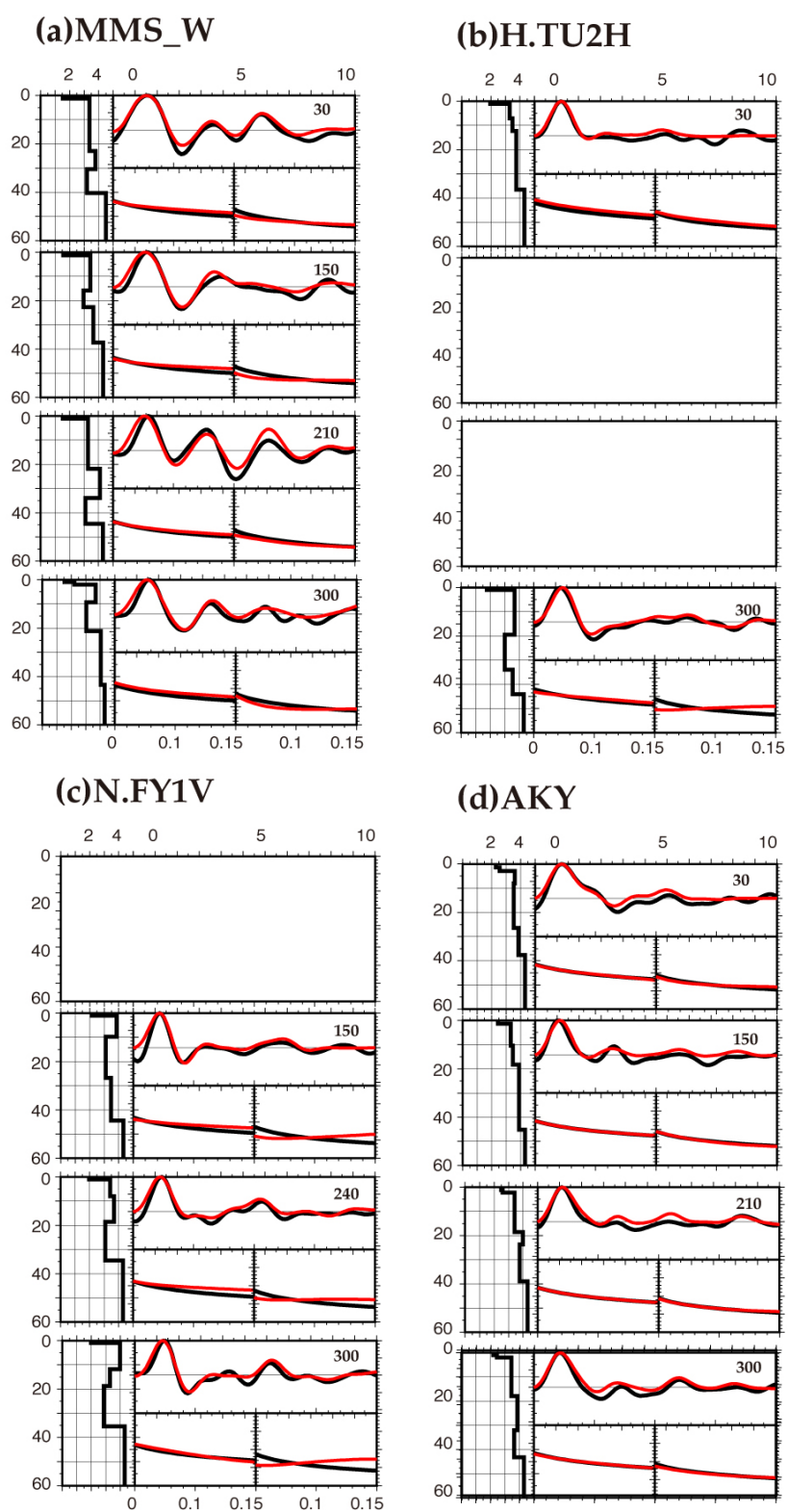
Figure 5.26: Examples of inversion results 2.
Same as Figure 5.25 but for the stations (a) MMS, (b) H.TU2H, (c) N.FY1V, and (d) AKY.

5.6.5   Probability distribution of S-wave velocities

The S wave velocity of each grid in Figures 5.16 and 5.17 are averaged over the multiple rays intersected in the same grid. Figure 5.27 depicts the standards deviations of the velocities in each grid along Line B. The standard deviations are large between -40 and -20 km at depths of 20–50 km, and between -20 and 10 at depths of 35–45 km, representing that both the west boundary of the low velocity region and the deep structure just below Mt. Fuji are not well constrained. However, the standard deviations in the low velocity region below Mt. Fuji is not so large and the number of RFs is very large, supporting the existence of the distinct low velocity region. Below the low velocity zone at -20 km at a depth about 40 km, the standard deviation become large, representing that the bottom depth of the low velocity layer is not well determined in this region. This is because the Rayleigh wave is not reconstructed at all around the region where a deep low velocity layer exists like the station FUJ as described above. The Love wave has sensitivity only in the shallow part, so the deeper part of the low velocity region is not constrained. Although the bottom depth of the low velocity boundary is not constrained, the number of rays is large and the least squares error is also small, we believe that there is a low velocity region at depths between 20 and 35 km.

Figure 5.28 shows examples of histograms of S wave velocities in fifteen regions along Line B. The number of seismic rays, averaged S wave velocities, the standard deviations, and the standard errors are listed in each panel. The standard errors are calculated using the bootstrap estimations. Velocities in each panel are resampled one hundred times by allowing overlapping among the original velocities, and the standard deviation among the average velocities of each resampled group is calculated.

Although the number of ray paths is small in the regions 1 and 13 (Figure 5.27c) where the normal oceanic PHS plate subducts, the existence of the low velocity oceanic crust is obvious because the standard deviations are not large (Figure 5.27b and 5.28) and the least squares errors are small (Figure 5.27d). The uncertainties of the velocity are large in regions 5, 10, and 12,

where the standard deviations are large in Figure 5.27b, representing that the west and the bottom boundaries of the low velocity region (region 6) and the bottom boundary of the low velocity region (region 9) are not well constrained. The bimodal behavior of the histograms in regions 7 and 9 may reflect the sharp velocity changes in horizontal direction. The S wave velocities in regions 2, 3, 4, 6, and 9 are lower than that in region 8, suggesting the "croissant-shaped" distribution of the low velocity, that is, velocities are lower in the surrounding regions and higher in the internal side. However, both the least squares errors (Figure 5.27d) and the standard deviations in regions 8 and 11 (Figures 5.27b and 5.28) indicate the uncertainties of the complicated velocity structure just below Mt. Fuji as observed in RFs at stations FUJ2 (Figure 5.25d).

Considering the aforementioned discussion, we conclude that the low velocity region below Mt. Fuji exists with a width of about 40 km in SW-NE direction. Although the lower boundary of the low velocity is not well constrained, it is clear that the low velocity zone ranges to a depth about 35–40 km as shown in the inversion results in each station.

(a) S wave velocity

(c) Number of RFs

(b) Sandard deviation

(d) Least squares error (E)
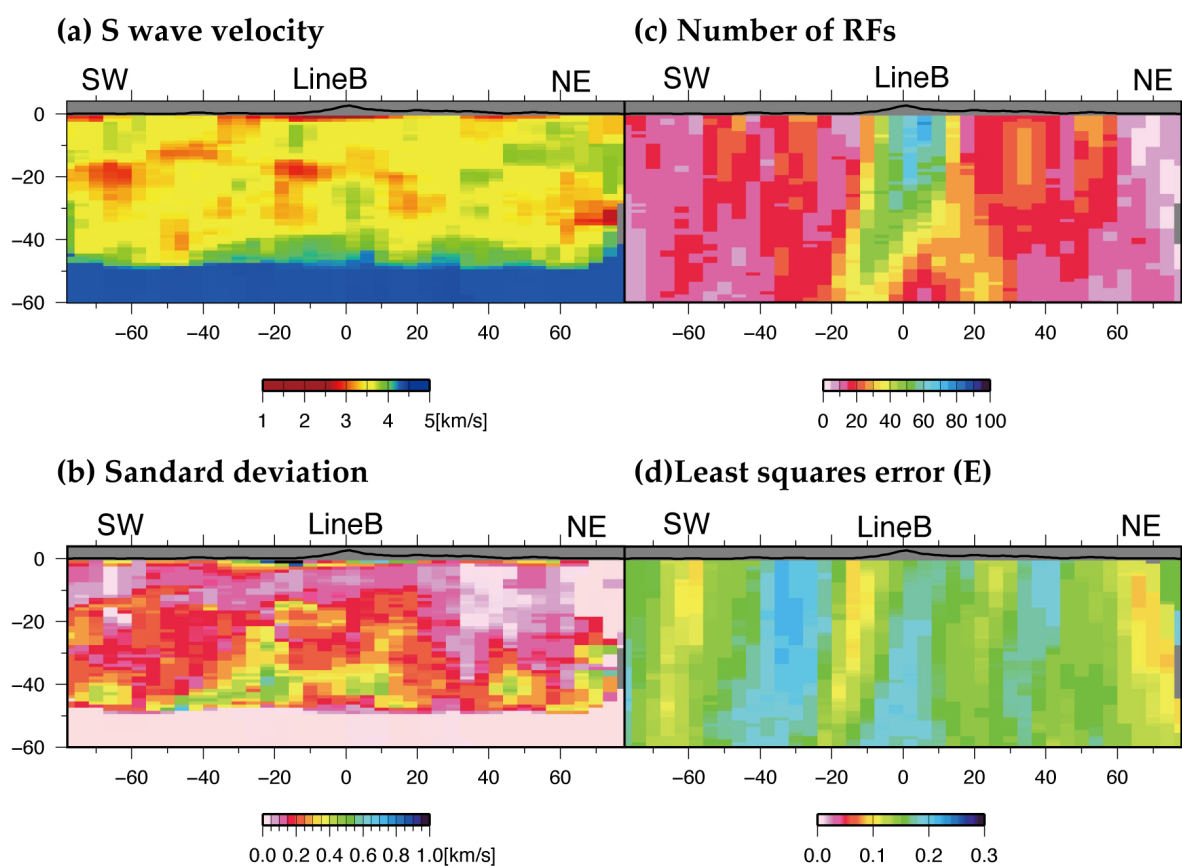
Figure 5.27: Probability distribution of S-wave velocities.
(a) The S wave velocity structure along the Line B same as Figure 5.17. (b) Standard deviation of velocities in each grid. (c) The number of RFs used to estimate the velocities same as Figure 5.18a. (d) Least squares error defined in equation (5.6) same as Figure 5.19a.
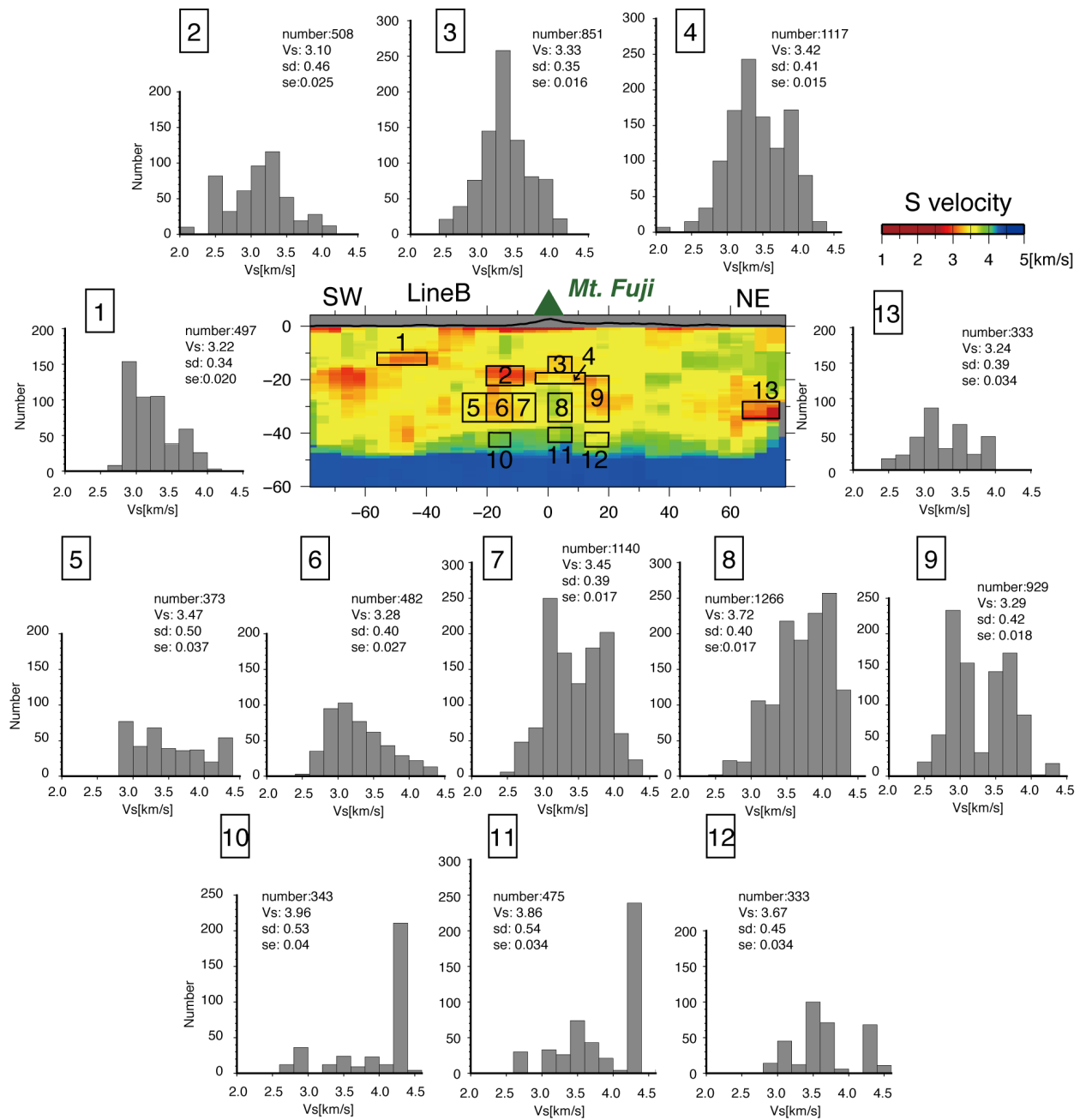
Figure 5.28: Probability distributions of S-wave velocities.
The S wave velocity histograms in areas 1–15 The location of each area is plotted in the S velocity image. Each histogram is binned every 0.2 km/s. The number of seismic rays, S wave velocities, standard deviations (sd), and standard errors (se) are stated in each panel.

6 Discussion

6.1 Evolution of the arc crust around Izu-collision zone

Figure 6.1 compares our velocity structure with that derived from an active seismic survey by *Kodaira et al.* (2007). The radial RF amplitudes (Figures 6.1a) suggest an existence of positive velocity boundaries at 40–60 km along the SE-NW cross section. Below Izu peninsula, this remarkable velocity boundary is at a depth of about 40 km. A seismic refraction analysis by *Asano et al.* (1985) also found a velocity interface at a depth of about 40 km below Izu peninsula. The S-wave velocity structure in Figure 6.1b shows a high velocity volume subducts from south to north. Although our study fixes Vp/Vs ratio and P-wave velocity is not well constrained, assuming the Vp/Vs ratio as 1.73 gives the P wave velocity at regions with green colors in Figure 6.1b as about 7.0 (km/s). *Kodaira et al.* (2007) and *Takahashi et al.* (2009) carried out a reflection/refraction survey, getting variations of P wave velocities along and across IBM before subduction. They interpret that the P wave velocity of 7.0 km/s at ∼20 km represents the lower crust consisting of mafic gabbroic plutons that are residuals in generating the felsic IBM upper and middle crust (*Kodaira et al.*, 2007). *Kodaira et al.* (2007) revealed the thickened middle crust with a 10-km thickness below basaltic volcanoes and the IBM arc crust before subduction with a width of 30-35 km. On the other hand, our result shows that the crust in IBM arc grows up to the width of more than 40 km. Considering the volume of the Izu peninsula is larger than other volcanic islands in IBM, the larger amount of basaltic melt probably ascended to Izu peninsula, resulting the volume of the crust grew below Izu peninsula become large. Also the collision near the northern tip must have thickened the IBM crust by compression.

As described in Chapter 4, cross sections of radial RF amplitudes show the differences in the boundaries of the upper mantle between the western and the eastern part of the collision zone of IBM (Line c, d, and e in Figure 4.5). The crustal structure of the colliding IBM is very complicated, while that of the Honshu arc is homogenous horizontally (*Arai and Iwasaki*, 2014). *Tamura*

et al. (2010) suggested that the middle crust of the IBM is delaminated from the lower crust during collision with the Houshu Island and the lower crust of IBM subducts below the Honshu Island. However, RF amplitudes of phase e1 and e2 (Line e in Figure 4.5e) show that the lower crust of the colliding IBM is deformed significantly. If there is a low velocity region above phase e2 in Line e, the phase e1 and e2 become continuous, but we think the depth gap between phase e1 and e2 is too large to explain only by the existence of the low velocity zone. These observations lead the idea that the collision between IBM and Honshu-arc has significant influence on the deep lower crustal structure of IBM. On the other hand, the boundary of the upper mantle in the western part of IBM (phase c1 in Figure 4.5e) is very smooth and continuous, representing the collision has no influence on the lower crust. This implies the structural difference between the western (fore-arc) and the eastern (back-arc) structures of IBM.

Furthermore, the upper boundaries of the subducting PHS plate inferred from the travel time tomography (*Nakajima et al.*, 2009) intersect with the boundary of the upper mantle of the IBM found in our study (at 140 km in Line c, d, and e). In these regions, the upper boundary of the PHS slab is ambiguous (*Nakajima et al.*, 2009), so we think the uncertainties of the upper boundary estimated by tomography are large. Because phase c1 in Line c (Figure 4.5c) continues to a depth of 60 km, we suppose the IBM does not subduct to a depth of about 100 km as estimated by tomography in this region. To clarify this assumption, further analyses with wider area need to be executed and the distribution of the Moho in Honshu-arc must have key information.
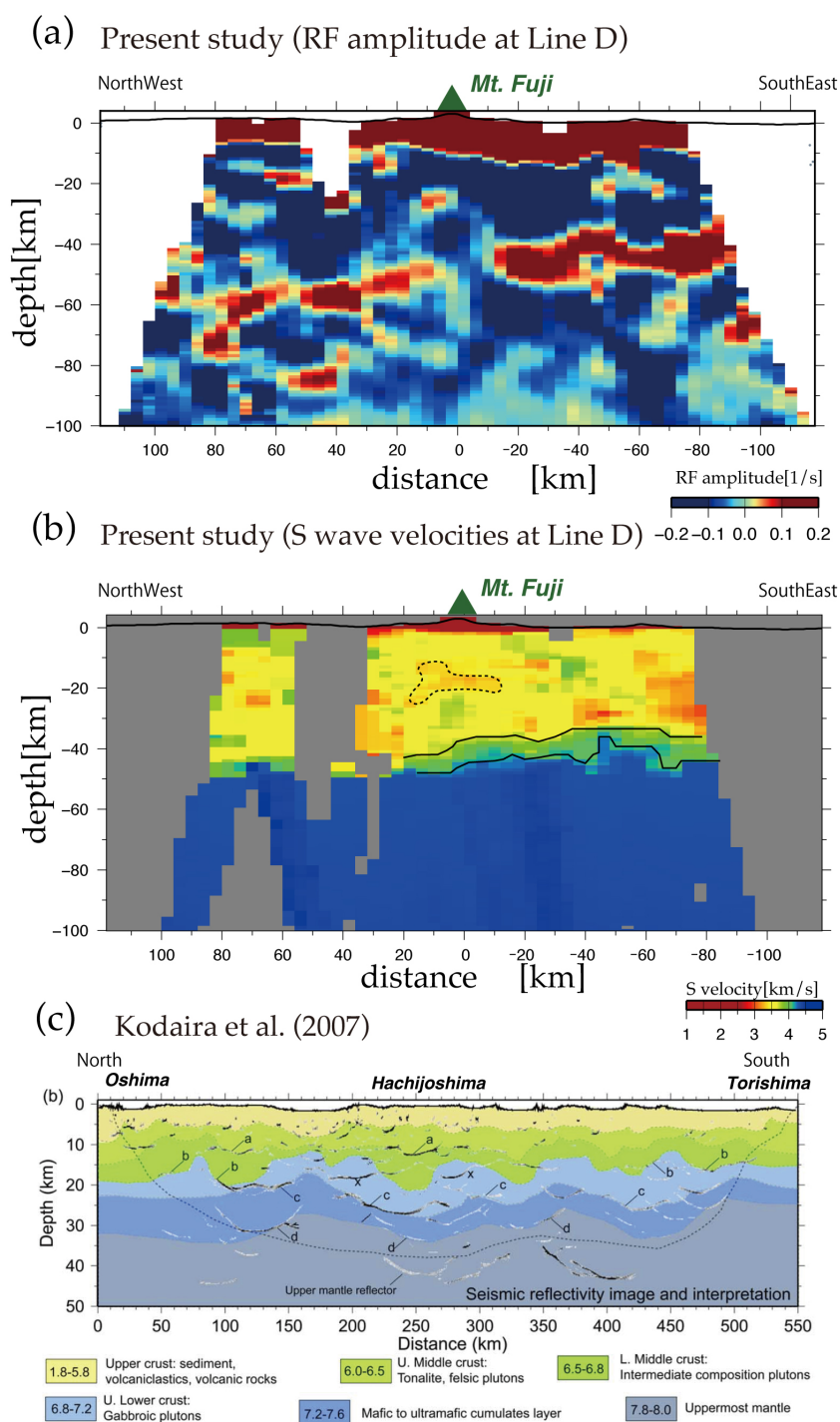
Figure 6.1: Comparison of velocity structures between the post-subducting and the pre-subducting IBM.
(a) The S wave velocity model by the RF inversion along the SE-NW line. The area circled by a black dot line represents the low velocity region below Mt. Fuji. Solid lines show the interface between the middle crust and the lower crust (upper) and the lower crust and the crust-mantle-transition layer (bottom). (b) Geological interpretation of the seismic velocity model derived from an active source seismic survey after *Kodaira et al.* (2007).

6.2   Comparison with the results of travel-time tomography in broad region

Figure 6.2 compares our velocity model with that obtained from a travel time tomography by *Nakajima et al.* (2009) and *Matsubara and Obara* (2011). The velocity models by tomographic studies have a distinct low velocity region at depths between 0 and 20 km to the southwest of Mt. Fuji, representing an oceanic crust subducting to the northwest from the Suruga trough. This is consistent with the result of our velocity model. Also, tomographic studies suggest a low velocity region at depths between 0 and 30 km (*Matsubara and Obara*, 2011) and between 20 and 50 km (*Nakajima et al.*, 2009) to the northeast of Mt Fuji, representing the subducting oceanic crust to the northeast from the Sagami trough. This is also consistent with our results. A difference between tomographic studies and our study is that the low velocity region below Mt. Fuji is broadly ranged with a connection to a low velocity zone corresponding to the low velocity oceanic crust. Our results have higher spatial resolution image to show that the low velocity region below Mt. Fuji is distributed with 20 km thickness in depth and 40 km width in horizontal as expressed by a broken line(Figure 6.2a).
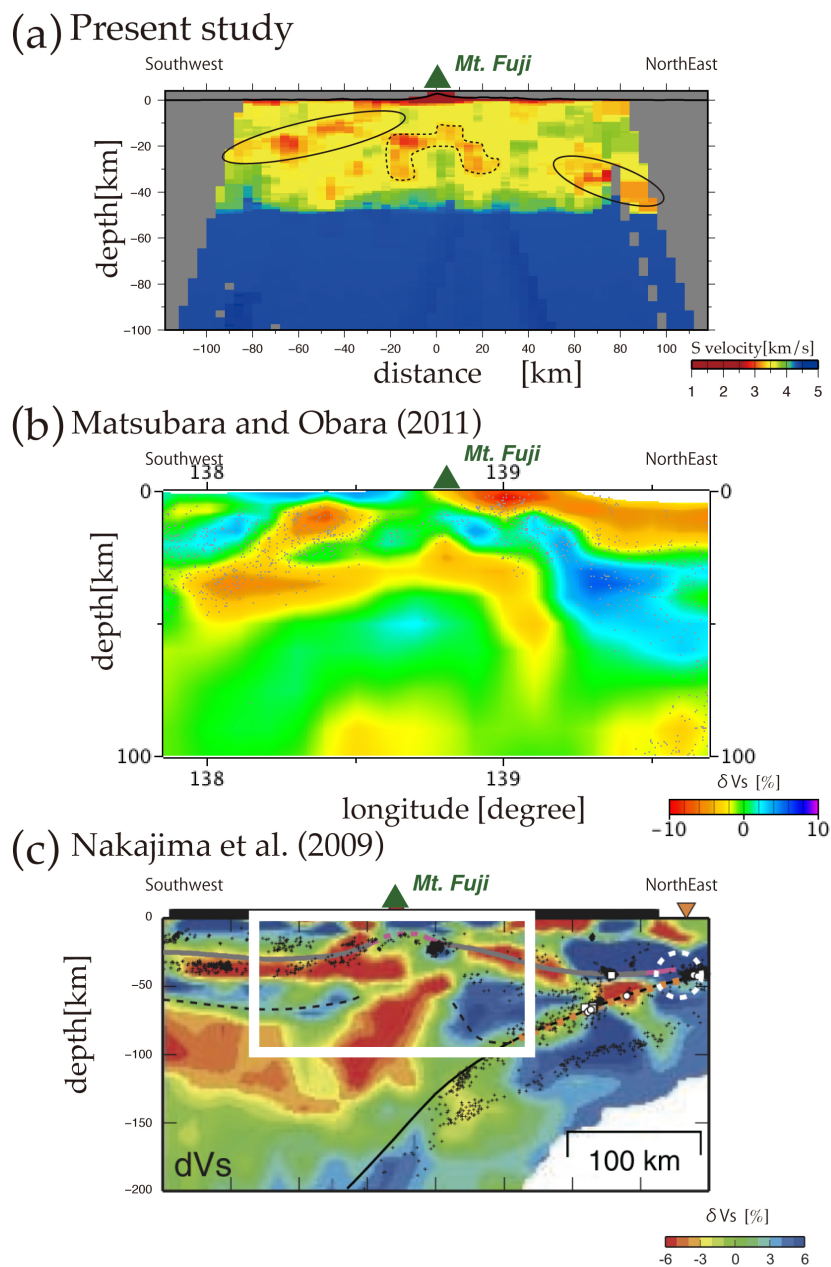
Figure 6.2: Comparison of our velocity structure with that from a travel time tomography. (a) The S wave velocity model by the RF inversion along the SE-NW line. Regions enclosed by black solid lines represent low velocity oceanic crust of subducting PHS plate. The black dot line shows a low velocity region below Mt. Fuji. (b) Perturbation of S wave velocities by *Matsubara and Obara* (2011) along the same cross section in (a). (c) Perturbation of S wave velocity after *Nakajima et al.* (2009). White rectangle represents roughly the same area as (a) and (b).

6.3   Comparison with the result of an ambient noise tomography.

Figure 6.3 compares our S wave velocity structure with that obtained from the surface wave tomography by *Nishida et al.* (2008) who found two low velocity regions (Figure 6.3b). A low velocity body at 20–120 km at the depths of 0–20 km represents a subducting oceanic crust. A low velocity body at 80–200 km at the depth of 30–40 km also represents a subducting oceanic crust. Sensitivity kernels of surface waves shown in Figure 6.3c indicate that the depths with high sensitivity are wide especially in low frequencies, resulting in a poor resolution in vertical direction. Also only surface waves of a frequency of 0.05 Hz have the sensitivity at depths more than 20 km, so that the S wave structure below 20 km is an average over a broad region in a horizontal direction. The depth of the low velocity layer is too deep to judge whether it is the oceanic crust or the low velocity region below Mt. Fuji.

It is difficult to constrain the absolute S wave velocity from RFs, but a joint inversion between RFs and surface waves enables us to constrain S wave velocities with higher resolution than those derived by *Nishida et al.* (2008). In Chapter 5, we remarked that the dispersion curve of the Rayleigh wave at the station FUJ is not well reconstructed by the inversion especially in lower frequencies. The velocity structure at FUJ has a large low velocity anomaly at 16-21 km and a smaller low velocity anomaly at 21–36 km, while *Nishida et al.* (2008) does not detect such a low velocity body (Figure 6.3d). Sensitivity kernels of surface waves show that at 0.05 Hz the sensitivity of the Rayleigh wave phase velocity is higher to S wave perturbation than that of the phase velocity of the Love wave so that the dispersion curves of the Rayleigh wave do not fit at all at the station FUJ where a distinct low velocity layer is required to fit the RFs. Furthermore, ambient noise tomography does not detect a low-velocity region with spatial scales much smaller than the inter-station distance because a seismic ray avoids a low-velocity region. Addition of seismograph stations around Mt. Fuji in ambient noise tomography can improve the resolution of the local low velocity region below Mt. Fuji as is the case with other volcanoes (e.g., *Nagaoka*

et al., 2012). However, because the low velocity region below Mt. Fuji is too deep to be sensitive in high frequencies as described above, it is difficult to detect the low velocity region solely by the ambient noise tomography.
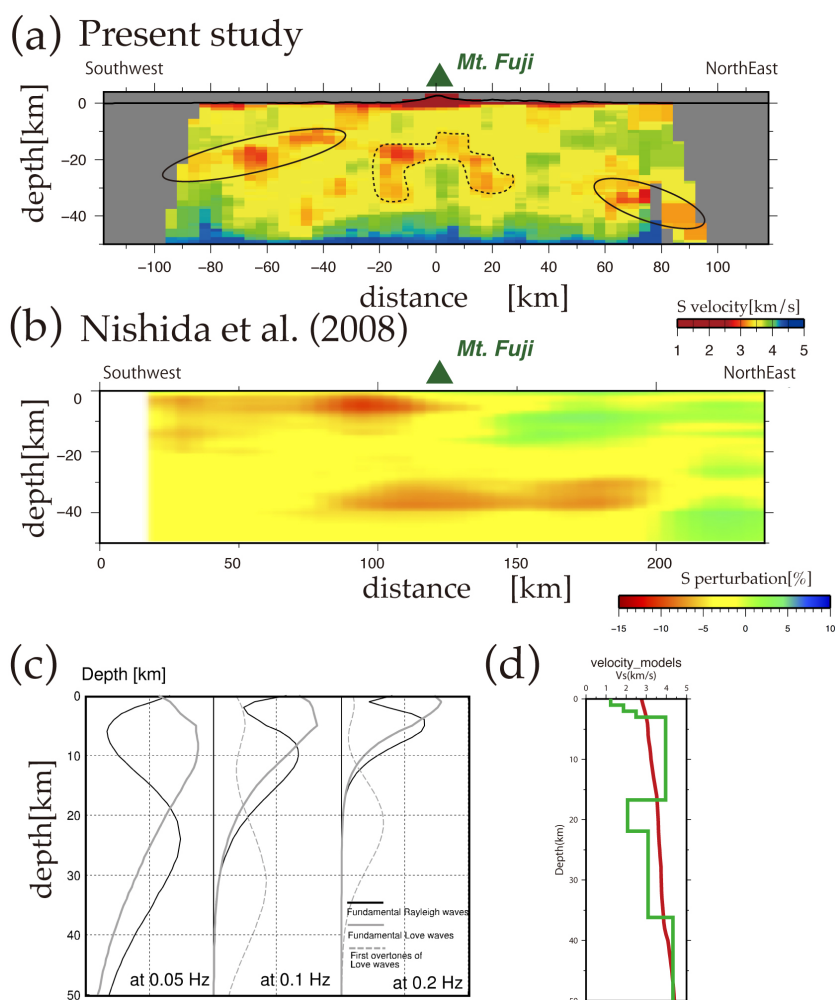
Figure 6.3: Comparison of the velocity structure by the joint inversion of RFs and dispersions of surface waves
S-wave velocity structure obtained by (a) our inversion incorporating both RFs and surface wave dispersions, and (b) *Nishida et al.* (2008). (c) The examples of the sensitivity kernel at 0.05, 0.1 and 0.2 Hz after *Nishida et al.* (2008). (d) The velocity structures at FUJ obtained from the RF inversion (green) and the surface wave inversion (red).

6.4   Comparison with the structure around Mt. Fuji by the regional tomography and the MT study

Figure 6.4 compares our results with a resistivity structure by *Aizawa et al.* (2004) and a seismic velocity structure derived from a travel time tomography by *Nakamichi et al.* (2007). *Aizawa et al.* (2004) found a gap of a distinct high resistivity layer to the northeast of Mt. Fuji (Figure 6.4b) at depths about 10–20 km with an interpretation that the magma of Mt. Fuji ascends through the gap. Our results show that the S wave velocity in the gap found by *Aizawa et al.* (2004) is about 3.0 km/s and slower than surrounding area, supporting their interpretation. Recently, a three-dimensional resistivity structure around Mt. Fuji detected a conductive region at depths of 10–20 km just below Mt. Fuji (*Aizawa et al.*, 2016). We interpret it to represent a magma reservoir of Mt. Fuji because it also corresponds to a low-velocity region. However, a low-velocity region detected by RF inversions at a depth of about 20 km and 10–15 km to the southwest from the summit of Mt. Fuji is not characterized as conductive in both two-dimensional and three-dimensional study (*Aizawa et al.*, 2004, 2016).   Old solidified magma with low porosity is imaged as a resistive body below caldera volcanoes (*Aizawa et al.*, 2008, 2014), but it is also imaged as high velocity (*Aoki et al.*, 2009), inconsistent with our results. Because Vp/Vs ratio in the low-velocity region is effective to constrain the condition of the magma below Mt. Fuji, investigating Vp/Vs ratio of the low-velocity region as model in RF inversions would be worth trackiling as a next subject.

A travel time tomography by *Nakamichi et al.* (2007) showed that a region with Vp/Vs ratio higher than 1.9 exists at depths more than 15 km below Mt. Fuji (Figures 6.4c and d). They interpreted this region as the magma chamber of Mt. Fuji. Our results also found a low velocity body in areas where *Nakamichi et al.* (2007) identified as a low velocity body. We interpret that the velocity body *Nakamichi et al.* (2007) found actually extends down to ~40 km where their study loses the resolution. Considering that *Nakamichi et al.* (2007) found a high Vp/Vs ratio at shallowest depths (15–20 km) of the low velocity body we found, we regard the low velocity body we found in this study as a magma chamber of Mt. Fuji.
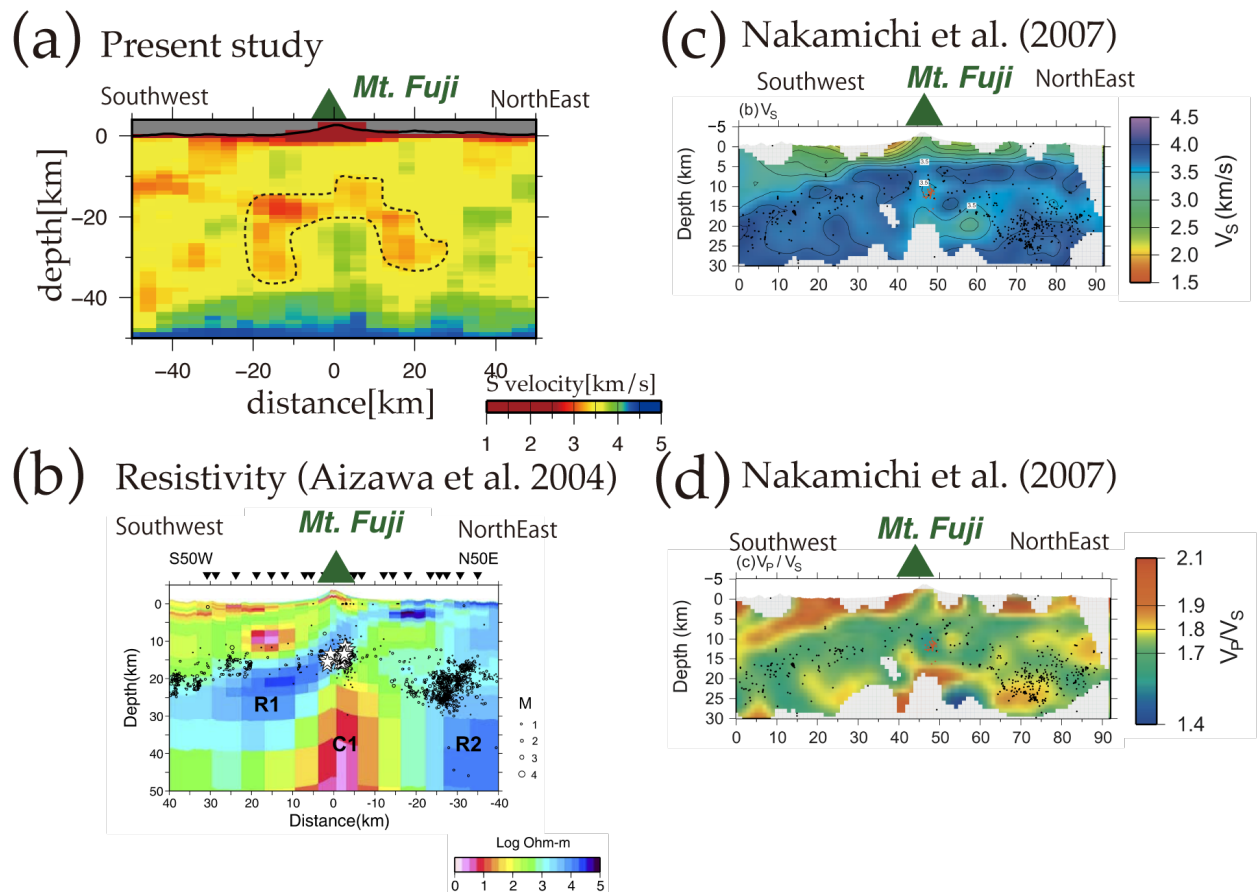
Figure 6.4: Comparison of the structure below Mt. Fuji with previous studies.
(a) The S wave velocity model by the RF inversion along the SE-NW line. (b) The resistivity structure below Mt. Fuji along almost the same line in (a) after *Aizawa et al.* (2004). (c), (d) The S wave velocity and Vp/Vs ratio along almost the same line in (a) after *Nakamichi et al.* (2007).

6.5 The gap of the positive phase below Mt. Fuji

Our results of RF inversions show that S wave velocities at 20–40 km depths around Mt. Fuji change remarkably in a horizontal direction (regions A, B, and C in Figure 6.5a). Figure 6.5b indicates a lack of distinct positive phases below region B at a depth of about 50 km. A possible interpretation for the gap is that the velocity contrast is locally gradual or there is a local low velocity layer in region B. Figures 6.5c-e compare stacked RFs that intersect regions A, B, and C in Figure 6.5a (the same cross section as in Figure 4.8b). The number of seismic rays passing through the target area is 1002, 1790, and 1049 in regions A, B, and C, respectively.

Stacked radial RFs in Figures 6.5c and 6.5e have positive phases at about 6 seconds representing the converted phase from the boundaries at about 50 km depth. The RF amplitude of this converted phase in region A (Figure 6.5a) is larger than that in Figure 6.5d, indicating that the velocity contrast at a depth of 50 km in region A is larger than that in region B. On the other hand, there is a positive phase from the interface at depths between 20 and 30 km in region B (Figure 6.5d). Also, a broad negative phase between 4 and 9 seconds in the stacked RFs of region B indicates that the velocity contrast of positive velocity boundary found in regions A and C at a depth of about 50 km is weak in region B. *Nakamura et al.* (2008) showed that the slab fluid in volcanic rocks of Mt. Fuji is originated predominantly from the PAC slab, rather than the PHS slab. This result implies that the PHS plate overriding the PAC plate does not contaminate the fluid component of magma originating from PAC. Together with our result that the existence of the velocity gap just below the magma chamber of Mt. Fuji also implies that the upwelling magma of Mt. Fuji from PAC plate passes through the area. However, because the standard deviation Figure 5.27b shows the uncertainties of velocity value in this region is large and the least squares error defined in equation (5.6) is large, further analysis need to be executed to confirm the assumption.

(c) RegionA (total RF number = 1002 , average rayP = 0.0731)

(d) RegionB (total RF number = 1790 , average rayP = 0.0688)

(e) RegionC (total RF number = 1049 , average rayP = 0.0721)
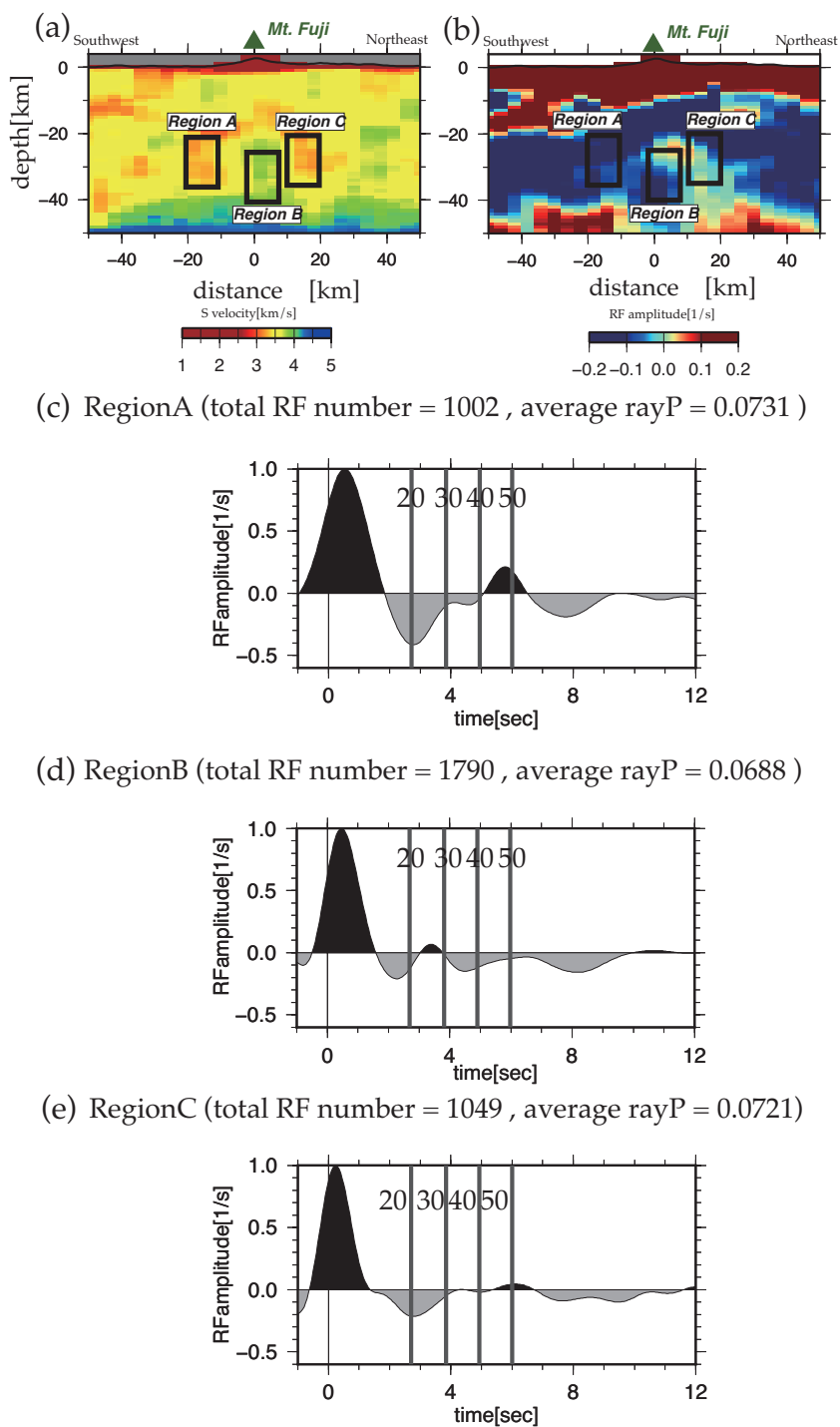
Figure 6.5: Comparisons of RFs between the regions whose velocities are different.
(a) Cross sections of RF amplitudes (left) and S wave velocity (right) along the same line in Figure
4.10. (b), (c), (d) Sacked RFs whose ray paths intersect (b) Region A, (c) Region B, and (d) Region
C. Gray solid lines with numbers represent arrival times of Ps waves converted at the depth of 20,
30, 40, and 50 km calculated from the same structure used in converting the RF time axis into
depth axis.

6.6   Magma plumbing system below Mt. Fuji

6.6.1   Two characteristics of Mt. Fuji from this study

As discussed in Chapter 1, there are two noteworthy characteristics of Mt. Fuji: the high long-term eruption rate and the basaltic composition of the magma. In this study, we cannot define the eruption rate because we have only the information about the present S wave velocity. *Abe et al.* (2010) found the low velocity layer with the S wave velocity 2.4 (km/s) at about 20 km depth below Mt. Aso by RF analysis and interpreted that the low velocity layer includes the melt or aqueous fluid because the velocity is too slow to explain only by the velocity decrease caused by the high temperature. The low velocity layer in our study is between about 2.5 and 3.0 (km/s) so that the melt or aqueous fluid possibly exists in the low velocity region. Considering the low velocity region below Mt. Fuji as a magma chamber (by black dot line in Figure 6.1b and 6.2a), the size of these regions is 40 km in horizontal and 20 km in depth at maximum.

Lees (2007) compiled the results of seismic velocity structures and attenuation structures beneath about fifty volcanoes, and the only volcanoes with the large deep low velocity zone as Mt. Fuji is Klyuchevskoy volcano in Kamchatka, Russia, one of the most active arc volcanoes in the Pacific Rim which erupts basaltic materials. The low velocity zone below Klyuchevskoy ranged 30–40 km width in the horizontal direction at depths between 20 and 35 km (Lees 2007, Lees et al. 2007). Another example of the large low velocity region in the lower crust below volcanoes is the Yellowstone, hotspot volcanoes with large caldera in North America. *Huang et al.* (2015) depicts the large low velocity zone with about 5–7 percent of Vp reduction at depths between 20–50 km with horizontal range of about 40–50 km. In Japan, the size of low velocity regions in the middle and lower crust below volcanoes are few reported. For example, *Nagaoka et al.* (2012) showed the low velocity zone below Mt. Asama with a range of 10 km in horizontally using ambient noise tomography. Also, *Yukutake et al.* (2015) shows the deep low velocity region below Mt. Hakone ranged with 10–20 km horizontally. Considering the aforementioned discussion, the low velocity

region below Mt. Fuji is one of the biggest low velocity area in the lower crust below volcanoes. Such a large magma chamber can make the long-term eruption rate remarkably large.

As referred in Chapter 1, *Fujii* (2007) argued that the crystallization of pyroxene is a key to explain the magma component erupted from Mt. Fuji. The basaltic melts with fluid crystallize in the order of pyroxene, olivine and plagioclase in high pressure suppressing the increase of the silica content, and the basaltic materials become dominant in erupted products. He concluded that the depth of magma chamber of Mt. Fuji should be deeper than 20 km. Our results show that the low velocity region below Mt. Fuji continues to the depth of about 40 km, supporting the idea of *Fujii* (2007).

6.6.2   The seismic structure around Mt. Fuji

Figure 6.6 shows a schematic illustration of our result in the SE-NW and SW-NE cross sections. In the SE-NW cross section (Figure 6.6a), IBM subducts from south to north. The IBM crust grows up to a width of about 40 km to the southeast of Mt. Fuji. The contrast of the velocity interface between the IBM crust and upper mantle is weak below Mt. Fuji. There is a low velocity region at a depth of about 20–30 km below Mt. Fuji and LFEs occurs in the uppermost part in the low velocity region. In the SW-NE cross section (Figure 6.6b), the same velocity boundaries are found where IBM is colliding with central Japan as seen in the SE-NW cross section in Figure 6.6a. The distinct low velocity regions are found, representing the oceanic crust where back-arc and fore-arc subduct are found. The low velocity region below Mt. Fuji continues to the depth of about 40 km to the northeast and southwest of Mt. Fuji, whereas continues to the depth of about 20–30 km just below Mt. Fuji.

6.7   Summaries of discussions and future works

The RF analysis executed in this study offers new insights into the magma plumbing system of Mt. Fuji, and the structure of colliding IBM. The most important result is the distribution of the

low velocity region below Mt. Fuji because previous studies did not successfully image the magma chamber of Mt. Fuji. Our results strongly support the deep magma chamber model proposed in *Fujii* (2007). Also, we indicate that the possibility of the magma plumbing path at depths about 40–50 km just below Mt. Fuji from the weak velocity contrast. Furthermore, the velocity boundaries of the subducting IBM inferred from the RF amplitudes show the complicated structure of the lower crust in IBM by the collision. The collision of IBM and the Honshu-arc has significant influence on the lower crust in eastern side of the IBM, whereas that has no influence in western side of the IBM. The intersection between the upper surface of the PHS and the boundary of the upper mantle in IBM found in our study represents that the IBM subducts shallower than expected by the travel time tomography.
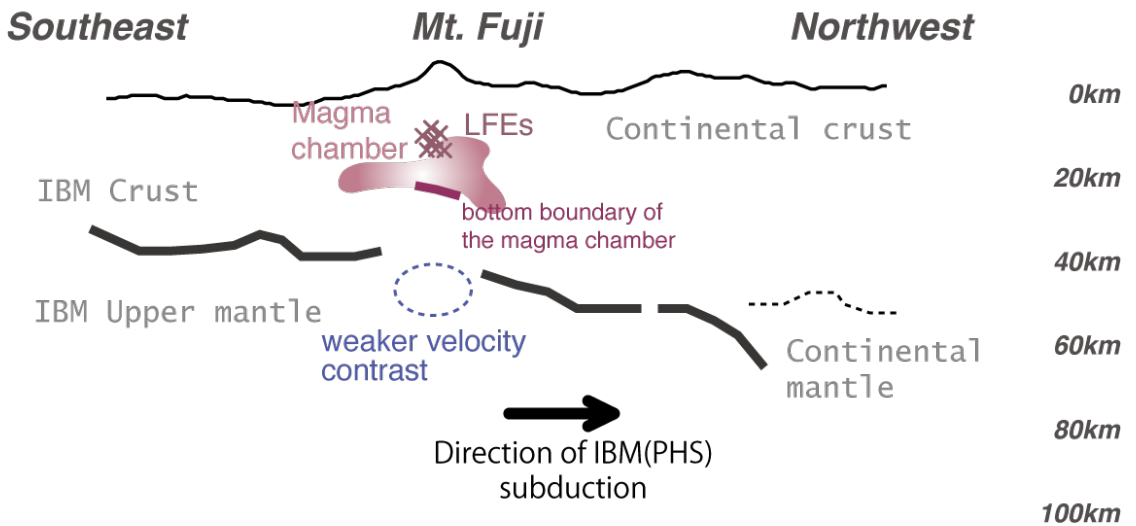
There are a lot of challenges for the next step. For example, we need to reconstruct the dispersion curves of the Rayleigh wave in the SA inversion around the area where the low velocity layer exists in deeper part. Because a deep and wide low velocity layer make the dispersion complicated, we need to take account the first overtone of the Rayleigh wave to explain the dispersion curve of the Rayleigh wave that are calculated using *Nishida et al.* (2008). This will improve the uncertainties in the bottom depth of the low velocity layer because the Rayleigh wave has larger sensitivity in deeper part than the Love wave. Also, the absolute amplitudes of RFs are effective to more detailed information on the subsurface structures around Mt. Fuji in the next step.

Furthermore, the expansion of the study area will offer more insights to the complicated collision and subduction between IBM and Honshu-arc. The wide distribution of both the Moho in Honshu-arc and the boundary of the IBM upper mantle can clarify the differences in the structure of the lower crust of colliding IBM between the eastern (fore-arc) and the western (back-arc) part, where the travel time tomography did not find the sharp upper boundary of the PHS slab.

Although the velocity structure at depths between 40 and 60 km just below Mt. Fuji leads the more detailed magma plumbing system from the upper mantle, standard deviations in this region (Figure 5.27b) shows the large uncertainties of the S wave velocities in this area. Because the

simplified five-layered model used in the SA inversion may be too simple to gain more insight into the complicated velocity structure just beneath Mt. Fuji, we need to execute the more detailed analysis in the next step (e.g., using gradually increased velocity structure model, or making the back azimuth range used in compositing stacked RFs smaller).

(a) Line D

Southeast   **Mt. Fuji**   **Northwest**

Magma chamber   LFEs

Continental crust

IBM Crust

bottom boundary of the magma chamber

IBM Upper mantle

weaker velocity contrast

Continental mantle

Direction of IBM(PHS) subduction

0km
20km
40km
60km
80km
100km

(b) Line B

Southwest   **Mt. Fuji**   **Northeast**

Continental crust   Magma chamber   LFEs   Continental crust

PHS crust

bottom boundary of the magma chamber

Upper mantle

IBM Crust   PHS crust

weaker velocity contrast

Direction of PHS subduction

IBM Upper mantle

Backarc   Izu-Bonin arc   Forearc

0km
20km
40km
60km
80km
100km

Figure 6.6: Schematic illustrations of the crust and upper mantle structure beneath Mt. Fuji. Interpretation of the subsurface structure below Mt. Fuji along (a)SE-NW and (b)SW-NE cross sections. IBM subducts from south to north beneath Mt. Fuji and the crustal width of IBM is more than 40 km below Mt. Fuji. The contrasts of S wave velocities between IBM crust and mantle become weak at the depth of about 50 km just below Mt. Fuji. Large low velocity region is found below Mt. Fuji at the depth of 20-40 km.

7 Conclusion

RF analyses are applied to teleseismic waveforms recorded at a number of seismic sites around Mt. Fuji. Receiver functions and S-wave velocity structure obtained from the inversion analysis have five following characteristics.

1. There are distinct large positive velocity boundaries at depths of 20–30 km and 40–50 km below Mt. Fuji, representing the lower boundary of the Fuji's magma chamber and the IBM crust.

2. A discontinuity of the velocity boundary is found at a depth of 50 km immediately beneath Mt. Fuji, representing a locally weakened velocity contrast.

3. The width of the thickened IBM crust beneath the Izu Peninsula is approximately 40 km.

4. Subducting oceanic crust from Suruga and Sagami troughs is represented by low S-wave velocities.

5. There is a distinct low velocity region below Mt. Fuji, representing the magma chamber.

Appendix A   How to deviate the Slepian tapers.

In this chapter, we outline the MTC method following *Slepian* (1983) and *Park et al.* (1987). Suppose we estimate the spectrum of the finite time series. A conventional direct method of spectral estimate is to multiply a time-series data by a taper $y(t) = (y_0, y_1, y_2 \cdots y_{N-1})$ and apply the Discrete Fourier Transform (DFT). The spectral leakage in frequency domain of this taper is represented as its DFT:

$$Y(f) = \sum_{t=0}^{N-1} y_t \exp(-2\pi i f t) \tag{A.1}$$

where f, $Y(f)$, and i represent the frequency, the Fourier transform of $y(t)$, and the imaginary unit. Suppose the sampling rate is 1 second. To minimize the bias at frequency f by a spectral leakage from outside the frequency band $|f| <= W$, where W is a chosen bandwidth, we maximize the fraction of spectral energy of Y defined in equation (A.1), β, within the chosen band:

$$\beta = \frac{\int_{-W}^{+W} |Y(f)|^2 df}{\int_{-\frac{1}{2}}^{\frac{1}{2}} |Y(f)|^2 df} \tag{A.2}$$

Then, we expand the numerator in equation (A.2) as follows:

$$
\begin{aligned}
\int_{-W}^{+W} |Y(f)|^2 df &= \int_{-W}^{+W} Y(f) Y^*(f) df \\
&= \int_{-W}^{+W} \sum_{t=0}^{N-1} y_t \exp(-2\pi i f t) \sum_{s=0}^{N-1} y_s \exp(2\pi i f s) df \\
&= \int_{-W}^{+W} \sum_{t=0}^{N-1} \sum_{s=0}^{N-1} y_t y_s \exp\left[2\pi i f (s-t)\right] df \\
&= \sum_{t=0}^{N-1} \sum_{s=0}^{N-1} y_t \frac{\sin\left[2\pi(s-t)W\right]}{\pi(s-t)} y_s
\end{aligned}
\tag{A.3}
$$

The Parseval's theorem rewrites the denominator in equation (A.2) as

$$\int_{-\frac{1}{2}}^{\frac{1}{2}} |Y(f)|^2 df = \sum_{t=0}^{N-1} |y_t|^2 \tag{A.4}$$

Then, the equation (A.2) is

$$\beta(\mathbf{y}) = \frac{\mathbf{y}^{\mathrm{T}} \cdot \mathbf{A} \cdot \mathbf{y}}{\mathbf{y}^{\mathrm{T}} \cdot \mathbf{y}} \tag{A.5}$$

where

$$\mathbf{y} = [y_0, y_1, y_2 \cdots y_{N-1}] \tag{A.6}$$

$$\mathbf{A}_{st} = \frac{\sin [2\pi(s - t)W]}{\pi(s - t)} \tag{A.7}$$

Next, we find the N-vector $\mathbf{y}$ that maximizes β. Define $\mathbf{w}$ as

$$\mathbf{w} = \frac{\mathbf{y}}{\sqrt{\mathbf{y} \cdot \mathbf{y}}} \tag{A.8}$$

Then, equation (A.2) becomes

$$\beta(\mathbf{w}) \;\; = \;\; \mathbf{w} \cdot \mathbf{A} \cdot \mathbf{w} \tag{A.9}$$

$$\mathbf{w}^{\mathrm{T}} \cdot \mathbf{w} \;\; = \;\; 1 \tag{A.10}$$

Lagrange's method of undetermined multipliers defines the N-vector $\mathbf{y}$ that maximizes β as

$$\frac{\partial}{\partial \mathbf{w}} (\beta - \lambda g) = 0 \tag{A.11}$$

where

$$g = \mathbf{w}^{\mathrm{T}} \cdot \mathbf{w} - 1 = 0 \tag{A.12}$$

Here, λ is the undetermined multipliers.

Substitution of equation (A.5) into (A.7) leads to a eigenvalue problem

$$
\begin{aligned}
\frac{\partial}{\partial w_i} (\beta - \lambda g) &= \frac{\partial}{\partial w_i} \left[(\mathbf{w}^{\mathrm{T}} \cdot \mathbf{A} \cdot \mathbf{w})_i - \lambda (\mathbf{w}^{\mathrm{T}} \cdot \mathbf{w} - 1) \right] \\
&= \mathbf{e}_i^{\mathrm{T}} \cdot \mathbf{A} \cdot \mathbf{w} + \mathbf{w}^{\mathrm{T}} \cdot \mathbf{A} \cdot \mathbf{e}_i - \lambda \mathbf{e}_i^{\mathrm{T}} \mathbf{w} - \lambda \mathbf{w}^{T} \mathbf{e}_i \\
&= (\mathbf{A} \cdot \mathbf{w})_i + (\mathbf{w}^{\mathrm{T}} \cdot \mathbf{A})_i - 2\lambda w_i \\
&= 2(\mathbf{A} \cdot \mathbf{w})_i - 2\lambda w_i \\
&= 0 \hspace{6cm} \text{(A.13)}
\end{aligned}
$$

where

$$
\frac{\partial \mathbf{w}}{\partial w_i} = \mathbf{e}_i \hspace{6cm} \text{(A.14)}
$$

So that the vector $\mathbf{y}$ that maximizes β is the solution of the eigen-equation

$$
\mathbf{A} \cdot \mathbf{y} - \lambda \mathbf{y} = 0 \hspace{6cm} \text{(A.15)}
$$

where λ represents the maximum of β.

Solutions of equation (A.15) are represented as ordered eigenvalues $1 > \lambda_0 > \lambda_1 > \cdots > \lambda_{N-1} > 0$ and associated eigenvectors. These eigenvectors are *the discrete $NW\pi$ prolate spheroidal sequences (DPSS)* in the time domain, and the Fourier transforms of the DPSS are known as *the discrete prolate spheroidal wave functions (DPSWF)* [Slepian, 1983]. The DPSS is doubly orthogonal, that is, this is orthogonal over $(-W, W)$ and over $(-\frac{1}{2}, \frac{1}{2})$ in frequency domain.

Combining these orthonormal sequences of tapers reduces the variances of overall spectrum estimates (*Park et al.*, 1987). To construct a multiple taper spectral estimate of a time series x_t, we calculate the DFT of the product of x_t and y_t and average them. However, larger side-lobes in higher orders give spurious effects for spectral estimates. In this study, we set the parameters of the MTC method as equation (2.19) according to *Park and Levin* (2000). Their study estimate RFs

using following equations:

$$H_R(\omega) \quad = \quad \frac{R(\omega)}{Z(\omega)} = \frac{E_r(\omega)}{E_z(\omega)} = \frac{E_r(\omega)E_z{}^*(\omega)}{E_z(\omega)E_z{}^*(\omega)} \tag{A.16}$$

$$H_T(\omega) \quad = \quad \frac{T(\omega)}{Z(\omega)} = \frac{E_t(\omega)E_z{}^*(\omega)}{E_z(\omega)E_z{}^*(\omega)} \tag{A.17}$$

Substituting the spectrum estimated by the MTC method to above equations, and using the doubly

orthogonal, RFs are redefined as

$$H_R(f) \quad = \quad \frac{\sum_{k=0}^{K-1} Z^k(f)^* R^k(f)}{\sum_{k=0}^{K-1}[Z^k(f)^* Z^k(f)] + S_0(f)} \tag{A.18}$$

$$H_T(f) \quad = \quad \frac{\sum_{k=0}^{K-1} Z^k(f)^* T^k(f)}{\sum_{k=0}^{K-1}[Z^k(f)^* Z^k(f)] + S_0(f)} \tag{A.19}$$

where the subscript k represents the spectrum estimated from the kth order of the *DPSS* and $S_0(f)$

represents a spectrum estimate of the pre-event noise on the vertical component. These definitions

enable a reliable estimation of the RFs.

References

Abe, Y., T. Ohkura, T. Shibutani, K. Hirahara, and M. Kato (2010), Crustal structure beneath Aso Caldera, Southwest Japan, as derived from receiver function analysis, *Journal of Volcanology and Geothermal Research*, *195*(1), 1–12, doi:10.1016/j.jvolgeores.2010.05.011.

Aizawa, K., R. Yoshimura, and N. Ohiman (2004), Splitting of the Philippine Sea Plate and a magma chamber beneath Mt. Fuji, *Geophysical Research Letters*, *31*(9), L09603, doi:10.1029/2004GL019477.

Aizawa, K., Y. Ogawa, T. Hashimoto, T. Koyama, W. Kanda, Y. Yamaya, M. Mishina, and T. Kagiyama (2008), Shallow resistivity structure of Asama Volcano and its implications for magma ascent process in the 2004 eruption, *Journal of Volcanology and Geothermal Research*, *173*(3-4), 165–177, doi:10.1016/j.jvolgeores.2008.01.016.

Aizawa, K., et al. (2014), Three-dimensional resistivity structure and magma plumbing system of the Kirishima Volcanoes as inferred from broadband magnetotelluric data, *Journal of Geophysical Research*, *119*, 198–215, doi:10.1002/2013JB010682.

Aizawa, K., et al. (2016), Gas pathways and remotely triggered earthquakes beneath Mount Fuji, Japan, *Geology*, *44*(1), G37,313.1, doi:10.1130/G37313.1.

Aki, K., and P. G. Richard (2002), *Quantitative seismology, 2nd edition*, University Science Books, Sausalito, California.

Amano, K., N. Matsubara, and M. Tagiri (2007), The Basemant of Mt. Fuji: The Tanzawa Mountain – Collided and Accreted Paleo-oceanic Island Arc – [in Japanese with English abstract], in *Fuji volcano*, pp. 59–68, Yamanashi Institute of Enviromental Sciences, Fuji-Yoshida, doi:10.1017/CBO9781107415324.004.

Ammon, C. J. (1991), The isolation of receiver effects from teleseismic P waveforms, *Bulletin of the Seismological Society of America*, *81*(6), 2504–2510.

Ammon, C. J., G. E. Randall, and G. Zandt (1990), On the nonuniqueness of receiver function inversions, *Journal of Geophysical Research*, *95*(B10), 15,303–15318, doi:10.1029/ JB095iB10p15303.

Aoike, K. (1999), Tectonic Evolution of the Izu Collision Zone, *Research Report of the Kanagawa Prefectural Museum, Natural History*, *9*, 113–151.

Aoki, Y., et al. (2009), P-wave velocity structure beneath Asama Volcano, Japan, inferred from active source seismic experiment, *Journal of Volcanology and Geothermal Research*, *187*(3-4), 272–277, doi:10.1016/j.jvolgeores.2009.09.004.

Arai, R. (2011), Multiple collision and subduction structure of the Izu-Bonin arc revealed by integrated analysis of active and passive source seismic data, *Doctoral thesis, The University of Tokyo*.

Arai, R., and T. Iwasaki (2014), Crustal structure in the northwestern part of the Izu collision zone in central Japan, *Earth, Planets and Space*, *66*(1), 21, doi:10.1186/1880-5981-66-21.

Arai, R., T. Iwasaki, H. Sato, S. Abe, and N. Hirata (2014), Contrasting subduction structures within the Philippine Sea plate: Hydrous oceanic crust and anhydrous volcanic arc crust, *Geochemistry, Geophysics, Geosystems*, *15*(5), 1977–1990, doi:10.1002/2014GC005321.

Araragi, K. R., M. K. Savage, T. Ohminato, and Y. Aoki (2015), Seismic anisotropy of the upper crust around Mount Fuji, Japan, *Journal of Geophysical Research*, *120*, 2739–2751, doi:10. 1002/2014JB011554.

Asano, S., et al. (1985), Crustal structure in the northern part of the Philippine Sea plate as derived

from seismic observations of Hatoyama-off Izu Peninsula Explosions, *Journal of Physics of the Earth*, *33*, 173–189.

Beaty, K. S., D. R. Schmitt, and M. Sacchi (2002), Simulated annealing inversion of multimode Rayleigh wave dispersion curves for geological structure, *Geophysical Journal International*, *151*(2), 622–631, doi:10.1046/j.1365-246X.2002.01809.x.

Bostock, M. G. (1999), Seismic waves converted from velocity gradient anomalies in the Earth's upper mantle, *Geophysical Journal International*, *138*(3), 747–756, doi:10.1046/j.1365-246x.1999.00902.x.

Cassidy, J. F. (1992), Numerical experiments in broadband receiver function analysis, *Bulletin of the Seismological Society of America*, *82*(3), 1453–1474.

Chung, T. W., J. M. Lees, K. Yoshimoto, E. Fujita, and M. Ukawa (2009), Intrinsic and scattering attenuation of the Mt Fuji Region, Japan, *Geophysical Journal International*, *177*(3), 1366–1382, doi:10.1111/j.1365-246X.2009.04121.x.

Darbyshire, F. A., K. F. Priestley, R. S. White, R. Stefánsson, G. B. Gudmundsson, and S. S. Jakobsdóttir (2000), Crustal structure of central and northern Iceland from analysis of teleseismic receiver functions, *Geophysical Journal International*, *143*(1), 163–184, doi:10.1046/j.1365-246x.2000.00224.x.

Efron, B., and R. Tibshirani (1991), Statistical data analysis in the computer age., *Science*, *253*(5018), 390–395, doi:10.1126/science.253.5018.390.

Fujii, T. (2007), Magmatology of Fuji Volcano [in Japanese with English abstract], in *Fuji volcano*, pp. 233–244, Yamanashi Institute of Enviromental Sciences, Fuji-Yoshida.

Fujita, E., T. Kozono, H. Ueda, Y. Kohno, S. Yoshioka, N. Toda, A. Kikuchi, and Y. Ida (2013),

Stress field change around the Mount Fuji volcano magma system caused by the Tohoku megathrust earthquake, Japan, *Bulletin of Volcanology*, *75*(1), 679, doi:10.1007/s00445-012-0679-9.

Gurrola, H., E. G. Baker, and B. J. Minster (1995), Simultaneous time-domain deconvolution with application to the computation of receiver functions, *Geophysical Journal International*, *120*, 537–543, doi:10.1111/j.1365-246X.1995.tb01837.x.

Helffrich, G. (2006), Extended-time multitaper frequency domain cross-correlation receiver-function estimation, *Bulletin of the Seismological Society of America*, *96*(1), 344–347, doi: 10.1785/0120050098.

Helmberger, D., and R. A. Wiggins (1971), Upper Mantle Structure of Midwestern United States, *Journal of Geophysical Research*, *76*(14).

Huang, H.-H., F.-C. Lin, B. Schmandt, J. Farrell, R. B. Smith, and V. C. Tsai (2015), The Yellowstone magmatic system from the mantle plume to the upper crust, *Science*, *348*(6236), 773–776, doi:10.1126/science.aaa5648.

Igarashi, T., T. Iidaka, and S. Miyabayashi (2011), Crustal structure in the Japanese Islands Inferred from Receiver Function Analysis [in Japanese with English abstract], *Journal of Seismological Society Japan*, *63*, 139–151.

Julia, J. (2007), Constraining velocity and density contrasts across the crust - mantle boundary with receiver function amplitudes, *Geophysical Journal International*, *171*, 286–301, doi:10.1111/j.1365-2966.2007.3502.x.

Julia, J., C. J. Ammon, R. B. Herrmann, and A. M. Correig (2000), Joint inversion of receiver function and surface wave dispersion observations, *Geophysical Journal International*, *143*(1), 99–112.

Kagiyama, T. (2007), Structure of Fuji Volcano [in Japanese with English abstract], in *Fuji volcano*, pp. 137–150, Yamanashi Institute of Enviromental Sciences, Fuji-Yoshida.

Kaneko, T., A. Yasuda, T. Fujii, and M. Yoshimoto (2010), Crypto-magma chambers beneath Mt. Fuji, *Journal of Volcanology and Geothermal Research*, *193*(3-4), 161–170, doi:10.1016/j.jvolgeores.2010.04.002.

Kennett, B. L. N., and N. J. Kerry (1979), Seismic waves in a stratified half space, *Geophysical Journal of the Royal Astronomical Society*, *57*, 557–583.

Kennett, B. L. N., E. R. Engdahl, and R. Buland (1995), Constraints on seismic velocities in the Earth from traveltimes, *Geophysical Journal International*, *122*(1), 108–124, doi:10.1111/j.1365-246X.1995.tb03540.x.

Kinoshita, S. M., T. Igarashi, Y. Aoki, and M. Takeo (2015), Imaging crust and upper mantle beneath Mount Fuji, Japan, by receiver functions, *Journal of Geophysical Research*, *120*, 3240–3254, doi:10.1002/2014JB011522.Received.

Kodaira, S., T. Sato, N. Takahashi, A. Ito, Y. Tamura, Y. Tatsumi, and Y. Kaneda (2007), Seismological evidence for variable growth of crust along the Izu intraoceanic arc, *Journal of Geophysical Research*, *112*, B05104, doi:10.1029/2006JB004593.

Langston, C. A. (1979), Structure under Mount Rainier, Washington, inferred from teleseismic body waves, *Journal of Geophysical Research*, *84*(B9), 4749–4762, doi:10.1029/JB084iB09p04749.

Lees, J. M., and M. Ukawa (1992), The South Fossa Magna, Japan, revealed by high-resolution P- and S-wave travel time tomography, *Tectonophysics*, *208*(4), 377–396, doi:10.1016/0040-1951(92)90436-A.

Levin, V., and J. Park (1997), P-SH conversions in a flat-layered medium with anisotropy of arbitrary orientation, *Geophysical Journal International*, *131*(2), 253–266, doi:10.1111/j. 1365-246X.1997.tb01220.x.

Lodge, A., and G. Helffrich (2009), Grid search inversion of teleseismic receiver functions, *Geophysical Journal International*, *178*(1), 513–523, doi:10.1111/j.1365-246X.2009.04176.x.

Ludwig, W. J., J. E. Nafe, and C. L. Drake (1970), *Seismic refraction in The Sea*, 53–84 pp., Maxwell, A.E.

Matsubara, M., and K. Obara (2011), The 2011 off the Pacific coast of Tohoku Earthquake related to a strong velocity gradient with the Pacific plate, *Earth, Planets and Space*, *63*(7), 663–667, doi:10.5047/eps.2011.05.018.

Matsubara, M., H. Hayashi, K. Obara, and K. Kasahara (2005), Low-velocity oceanic crust at the top of the Philippine Sea and Pacific plates beneath the Kanto region, central Japan, imaged by seismic tomography, *Journal of Geophysical Research*, *110*(12), 1–15, doi:10.1029/ 2005JB003673.

Metropolis, N., A. W. Rosenbluth, M. N. Rosenbluth, A. H. Teller, and E. Teller (1953), Equation of state calculations by fast computing machines, *Journal of Chemical Physics*, *21*(6), doi:doi: 10.1063/1.1699114.

Nagaoka, Y., K. Nishida, Y. Aoki, M. Takeo, and T. Ohminato (2012), Seismic imaging of magma chamber beneath an active volcano, *Earth and Planetary Science Letters*, *333-334*(JUNE), 1–8, doi:10.1016/j.epsl.2012.03.034.

Nakajima, J., F. Hirose, and A. Hasegawa (2009), Seismotectonics beneath the Tokyo metropolitan area , Japan : Effect of slab-slab contact and overlap on seismicity, *Journal of Geophysical Research*, *114*, 1–23, doi:10.1029/2008JB006101.

Nakamichi, H., M. Ukawa, and S. Sakai (2004), Precise hypocenter locations of midcrustal low-frequency earthquakes beneath Mt. Fuji, Japan, *Earth Planets Space*, *56*(56), 40–43.

Nakamichi, H., H. Watanabe, and T. Ohminato (2007), Three‐dimensional velocity structures of Mount Fuji and the South Fossa Magna, central Japan, *Journal of Geophysical Research*, *112*, B03310, doi:10.1029/2005JB004161.

Nakamura, H., H. Iwamori, and J. Kimura (2008), Geochemical evidence for enhanced fluid flux due to overlapping subducting plates, *Nature Geoscience*, *1*(6), 380–384, doi:10.1038/ngeo200.

Nishida, K., H. Kawakatsu, and K. Obara (2008), Three-dimensional crustal S wave velocity structure in Japan using microseismic data recorded by Hi-net tiltmeters, *Journal of Geophysical Research*, *113*, B10302, doi:10.1029/2007JB005395.

Okino, K., Y. Shimakawa, and N. Shinji (1994), Evolution of the Shikoku Basin, *Journal of Geomagnetism and Geoelectricity*, *46*, 463–479.

Okino, K., S. Kasuga, and Y. Ohara (1998), A new scenario of the Parece Vela Basin genesis, *Marine Geophysical Researches*, *20*(1), 21–40, doi:10.1023/a:1004377422118.

Park, J., and V. Levin (2000), Receiver functions from multiple-taper spectral correlation estimates, *Bulletin of the Seismological Society of America*, *90*(6), 1507–1520.

Park, J., C. R. Lindvergl, and F. L. I. Vernon (1987), Multipaper Spectral Analysis of High-Frequency Seismograms, *Journal of Geophysical Research*, *92*, 12,675–12,684, doi:10.1029/JB092iB12p12675.

Richards, M. A., and C. Lithgow-Bertelloni (1996), Plate motion changes, the Hawaiian-Emperor bend, and the apparent success and failure of geodynamic models, *Earth and Planetary Science Letters*, *137*(1-4), 19–27, doi:10.1016/0012-821X(95)00209-U.

Rychert, C. A., S. Rondenay, and K. M. Fischer (2007), P-to-S and S-to-P imaging of a sharp lithosphere-asthenosphere boundary beneath eastern North America, *Journal of Geophysical Research*, *112*(8), 1–21, doi:10.1029/2006JB004619.

Saito, M. (1988), DISPER80: A subroutine package for the calculation of seismic normal-mode solutions, in *Seismological Algorithms: Computational Methods and Computer Programs*, edited by D. J. Doornbos, pp. 293–319, Academic Press, San Diego.

Sakai, S., et al. (2001), Magma Migration from the Point of View of Seismic Activity in the Volcanism of Miyake-jima Island in 2000 [in Japanese with English abstract], *Journal of Geography (Chigaku Zasshi)*, *110*(2), 145–155.

Salmon, M. L., T. A. Stern, and M. K. Savage (2011), A major step in the continental Moho and its geodynamic consequences: the Taranaki-Ruapehu line, New Zealand, *Geophysical Journal International*, *186*(1), 32–44, doi:10.1111/j.1365-246X.2011.05035.x.

Sambridge, M. (1999a), Geophysical inversion with a neighbourhood algorithm – II . Appraising the ensemble, *Geophysical Journal International*, *138*, 727–746.

Sambridge, M. (1999b), Geophysical inversion with a neighbourhood algorithm—I.Searching a parameter space, *Geophysical Journal International*, *138*, 479–494.

Sambridge, M., and K. Mosegaard (2002), Monte Carlo Methods in Geophysical Inverse Problems, *Reviews of Geophysics*, *40 (3)*(3), 29, doi:10.1029/2000rg000089.

Sato, H., T. Iwasaki, K. Kasahara, E. Kurashimo, T. Ishiyama, R. Arai, and T. Nakayama (2012), Lithospheric structure of the Kanto area deduced by low-fold seismic reflection profiling and earthquake interferometry analysis [in Japanese], *FY 2011 Report of the Special Project for Earthquake Disaster Mitigation in Tokyo Metropolitan Area*, pp. 75–136.

Savage, M. K., J. Park, and H. Todd (2007), Velocity and anisotropy structure at the Hikurangi subduction margin, New Zealand from receiver functions, *Geophysical Journal International*, *168*(3), 1034–1050, doi:10.1111/j.1365-246X.2006.03086.x.

Sen, M. K., and P. L. Stoffa (2013), *Global Optmization Methods in Geophysical Inversion*, Cambridge university press, New York.

Seno, T., S. Stein, and A. E. Gripp (1993), A model for the motion of the Philippine Sea plate consistent with NUVEL-1 and geological data, *Journal of Geophysical Research*, *98*, 17,941–17,948, doi:10.1029/93JB00782.

Seno, T., T. Sakurai, and S. Stein (1996), Can the Okhotsk Plate be discriminated from the North American plate?, *Journal of Geophysical Research*, *101*(B5), 11,305–11315, doi:10.1029/96JB00532.

Shibutani, T., M. Sambridge, and B. Kennett (1996), Genetic algorithm inversion for receiver functions with application to crust and uppermost mantle structure, *Geophysical Research Letters*, *23*(14), 1829–1832.

Shibutani, T., K. Hirahara, and T. Ueno (2009), Receiver Function Analyses for Estimating Seismic Velocity Discontinuity Structure [in Japanese with English abstract], *Journal of the Seismological Society of Japan. 2nd ser.*, *61*, 199–207, doi:10.4294/zisin.61.199.

Shiomi, K. (2012), New Measurements of Sensor Orientation at NIED Hi-net Stations [in Japanese with English abstract], *Report of NIED*, *80*, 1–20.

Shiomi, K., H. Sato, K. Obara, and M. Ohtake (2004), Configuration of subducting Philippine Sea plate beneath southwest Japan revealed from receiver function analysis based on the multivariate autoregressive model, *Journal of Geophysical Research*, *109*, B04308, doi:10.1029/2003JB002774.

Slepian, D. (1983), Some comments on Fourier analysis, uncertainty and modeling, *SIAM review*, *25*(3), 379–393, doi:10.1137/1025078.

Stern, R. J., M. J. Fouch, and S. L. Klemperer (2003), *An overview of the Izu-Bonin-Mariana subduction factory*, vol. 183, 175–222 pp., Geophys. Monogr. Ser, doi:10.1029/138GM10.

Takahashi, M. (2000), The magma supply system and tectonics of Fuji Volcano [in Japanese with English abstract], *Chikyu monthly*, *22*, 516–523.

Takahashi, N., et al. (2009), Structural variations of arc crusts and rifted margins in the southern Izu-Ogasawara arc-back arc system, *Geochemistry, Geophysics, Geosystems*, *10*(June), doi:10.1029/2008GC002146.

Tamura, Y. (2011), Formation of Continental Crust at the Izu-Honshu Collision Zone [in Japanese with English abstract], *Journal of Geography (Chigaku Zasshi)*, *120*(4), 567–584.

Tamura, Y., et al. (2010), Missing Oligocene Crust of the Izu-Bonin Arc: Consumed or Rejuvenated During Collision?, *Journal of Petrology*, *51*(4), 823–846, doi:10.1093/petrology/egq002.

Tsukui, M., M. Sakuyama, T. Koyaguchi, and K. Ozawa (1986), Long-term eruption rates and dimensions of magma reservoirs beneath Quaternary polygenetic volcanoes in Japan, *Journal of Volcanology and Geothermal Research*, *29*, 189–202.

Ueno, H., S. Hatakeyama, T. Aketagawa, J. Funasaki, and N. Hamada (2002), Improvement of hypocenter determination procedures in the japan meteorological agency [in Japanese with English abstract], *Q. J. Seism*, *65*, 123–134.

Ukawa, M. (2005), Deep low-frequency earthquake swarm in the mid crust beneath Mount Fuji (Japan) in 2000 and 2001, *Bulletin of volcanology*, *68*(1), 47–56, doi:10.1007/s00445-005-0419-5.

Vinnik, L. P., C. Reigber, I. M. Aleshin, G. L. Kosarev, M. K. Kaban, S. I. Oreshin, and S. W. Roecker (2004), Receiver function tomography of the central Tien Shan, *Earth and Planetary Science Letters*, *225*(1-2), 131–146, doi:10.1016/j.epsl.2004.05.039.

Wirth, E. A., and M. D. Long (2012), Multiple layers of seismic anisotropy and a low-velocity region in the mantle wedge beneath Japan: Evidence from teleseismic receiver functions, *Geochemistry, Geophysics, Geosystems*, *13*(8), n/a–n/a, doi:10.1029/2012GC004180.

Yamauchi, M., K. Hirahara, and T. Shibutani (2003), High resolution receiver function imaging of the seismic velocity discontinuities in the crust and the uppermost mantle beneath southwest Japan, *Earth, Planets and Space*, *55*(1), 59–64, doi:10.1186/BF03352463.

Yoshimoto, M., T. Fujii, T. Kaneko, A. Yasuda, S. Nakada, and A. Matsumoto (2010), Evolution of Mount Fuji, Japan: Inference from drilling into the subaerial oldest volcano, pre-Komitake, *Island Arc*, *19*(3), 470–488, doi:10.1111/j.1440-1738.2010.00722.x.

Yukutake, Y., R. Honda, M. Harada, R. Arai, and M. Matsubara (2015), A magma-hydrothermal system beneath Hakone volcano, central Japan, revealed by highly resolved velocity structures, *Journal of Geophysical Research*, *120*(5), 3293–3308, doi:10.1002/2014JB011856.

Zhu, L., and H. Kanamori (2000), Moho depth variation in southern California, *Journal of Geophysical Research*, *105*, 2969–2980, doi:10.1029/1999JB900322.

Acknowledgment